



---

MACROSCOPIC CROSSLINKED NEAT CARBON NANOTUBE MATERIALS

Zhiyong Liang  
FLORIDA STATE UNIV TALLAHASSEE

---

10/01/2015  
Final Report

DISTRIBUTION A: Distribution approved for public release.

**REPORT DOCUMENTATION PAGE**

*Form Approved  
OMB No. 0704-0188*

The public reporting burden for this collection of information is estimated to average 1 hour per response, including the time for reviewing instructions, searching existing data sources, gathering and maintaining the data needed, and completing and reviewing the collection of information. Send comments regarding this burden estimate or any other aspect of this collection of information, including suggestions for reducing the burden, to the Department of Defense, Executive Service Directorate (0704-0188). Respondents should be aware that notwithstanding any other provision of law, no person shall be subject to any penalty for failing to comply with a collection of information if it does not display a currently valid OMB control number.

**PLEASE DO NOT RETURN YOUR FORM TO THE ABOVE ORGANIZATION.**

<b>1. REPORT DATE (DD-MM-YYYY)</b> 28-09-2015	<b>2. REPORT TYPE</b> Final	<b>3. DATES COVERED (From - To)</b> 07-07-2011 - 30-06-2015
--	--------------------------------	--

<b>4. TITLE AND SUBTITLE</b> Macroscopic Crosslinked Neat Carbon Nanotube Materials and CNT/Carbon Fiber Hybrid Composites: Supermolecular Structure and New Failure Mode Study	<b>5a. CONTRACT NUMBER</b>
	<b>5b. GRANT NUMBER</b> FA9550-1101-0131
	<b>5c. PROGRAM ELEMENT NUMBER</b>

<b>6. AUTHOR(S)</b> Liang, Zhiyong (Richard) and Wang, Ben	<b>5d. PROJECT NUMBER</b> 031492
	<b>5e. TASK NUMBER</b>
	<b>5f. WORK UNIT NUMBER</b>

<b>7. PERFORMING ORGANIZATION NAME(S) AND ADDRESS(ES)</b> Florida State University, 2005 Levy Ave., Tallahassee, FSL 32310 Georgia Tech Manufacturing Institute, Georgia Institute of Technology, Atlanta, GA 30332	<b>8. PERFORMING ORGANIZATION REPORT NUMBER</b>
---	---

<b>9. SPONSORING/MONITORING AGENCY NAME(S) AND ADDRESS(ES)</b> Air Force Office of Scientific Research 875 N. Randolph Street Suite 325, Room 3112 Arlington, VA 22203	<b>10. SPONSOR/MONITOR'S ACRONYM(S)</b> AFOSR
	<b>11. SPONSOR/MONITOR'S REPORT NUMBER(S)</b>

**12. DISTRIBUTION/AVAILABILITY STATEMENT**  
Approved for public release

**13. SUPPLEMENTARY NOTES**

**14. ABSTRACT**  
Two novel low-density material systems were explored to attempt to realize the ultimate intrinsic properties of CNTs for scale-up applications: 1) continuous highly aligned CNT tapes or sheets and 2) CNT sheet/ carbon fiber hybrid composites (CNT/CF) with aerospace-grade quality and carbon fiber concentration. We studied different approaches for engineering CNT networks in CNT thin films to achieve a high degree of alignment and graphitic crystal packing. We discovered that the unique geometrically constrained self-assembly and graphitic crystal packing of flattened and aligned CNTs can lead to close surface contact between CNTs to substantially improve the load transfer and mechanical properties. We also revealed that extremely low permeability ( $\times 10^{-17}$ ~ $10^{-19}$  m<sup>2</sup>) of CNT thin film or buckypaper materials could largely eliminate through-thickness flow of resin matrix during composite autoclave fabrication process. Modifications in the processing parameters and consideration of strong capillary resin absorption of CNT networks during CNT buckypaper/CF prepreg materials for hybrid composites are needed to fabricate aerospace-grade hybrid composites with 5~8 wt.% CNT and 50~60 vol.% carbon fiber concentrations. The composites with CNT/CF alternative interply hybridization demonstrated promising mechanical/electrical multifunctional feature. Strong CNT layers acted as effective microcrack arresting layers to potentially improve damage tolerance properties.

**15. SUBJECT TERMS**  
Nanocomposites, Low-density materials, CNT sheets, Buckypaper, Nanotube alignment, Hybrid composites

<b>16. SECURITY CLASSIFICATION OF:</b>			<b>17. LIMITATION OF ABSTRACT</b> UU	<b>18. NUMBER OF PAGES</b>	<b>19a. NAME OF RESPONSIBLE PERSON</b> Richard Liang
<b>a. REPORT</b> U	<b>b. ABSTRACT</b> U	<b>c. THIS PAGE</b> U			<b>19b. TELEPHONE NUMBER (Include area code)</b> (850) 645-8998

## INSTRUCTIONS FOR COMPLETING SF 298

**1. REPORT DATE.** Full publication date, including day, month, if available. Must cite at least the year and be Year 2000 compliant, e.g. 30-06-1998; xx-06-1998; xx-xx-1998.

**2. REPORT TYPE.** State the type of report, such as final, technical, interim, memorandum, master's thesis, progress, quarterly, research, special, group study, etc.

**3. DATES COVERED.** Indicate the time during which the work was performed and the report was written, e.g., Jun 1997 - Jun 1998; 1-10 Jun 1996; May - Nov 1998; Nov 1998.

**4. TITLE.** Enter title and subtitle with volume number and part number, if applicable. On classified documents, enter the title classification in parentheses.

**5a. CONTRACT NUMBER.** Enter all contract numbers as they appear in the report, e.g. F33615-86-C-5169.

**5b. GRANT NUMBER.** Enter all grant numbers as they appear in the report, e.g. AFOSR-82-1234.

**5c. PROGRAM ELEMENT NUMBER.** Enter all program element numbers as they appear in the report, e.g. 61101A.

**5d. PROJECT NUMBER.** Enter all project numbers as they appear in the report, e.g. 1F665702D1257; ILIR.

**5e. TASK NUMBER.** Enter all task numbers as they appear in the report, e.g. 05; RF0330201; T4112.

**5f. WORK UNIT NUMBER.** Enter all work unit numbers as they appear in the report, e.g. 001; AFAPL30480105.

**6. AUTHOR(S).** Enter name(s) of person(s) responsible for writing the report, performing the research, or credited with the content of the report. The form of entry is the last name, first name, middle initial, and additional qualifiers separated by commas, e.g. Smith, Richard, J, Jr.

**7. PERFORMING ORGANIZATION NAME(S) AND ADDRESS(ES).** Self-explanatory.

**8. PERFORMING ORGANIZATION REPORT NUMBER.**

Enter all unique alphanumeric report numbers assigned by the performing organization, e.g. BRL-1234; AFWL-TR-85-4017-Vol-21-PT-2.

**9. SPONSORING/MONITORING AGENCY NAME(S) AND ADDRESS(ES).** Enter the name and address of the organization(s) financially responsible for and monitoring the work.

**10. SPONSOR/MONITOR'S ACRONYM(S).** Enter, if available, e.g. BRL, ARDEC, NADC.

**11. SPONSOR/MONITOR'S REPORT NUMBER(S).** Enter report number as assigned by the sponsoring/monitoring agency, if available, e.g. BRL-TR-829; -215.

**12. DISTRIBUTION/AVAILABILITY STATEMENT.** Use agency-mandated availability statements to indicate the public availability or distribution limitations of the report. If additional limitations/ restrictions or special markings are indicated, follow agency authorization procedures, e.g. RD/FRD, PROPIN, ITAR, etc. Include copyright information.

**13. SUPPLEMENTARY NOTES.** Enter information not included elsewhere such as: prepared in cooperation with; translation of; report supersedes; old edition number, etc.

**14. ABSTRACT.** A brief (approximately 200 words) factual summary of the most significant information.

**15. SUBJECT TERMS.** Key words or phrases identifying major concepts in the report.

**16. SECURITY CLASSIFICATION.** Enter security classification in accordance with security classification regulations, e.g. U, C, S, etc. If this form contains classified information, stamp classification level on the top and bottom of this page.

**17. LIMITATION OF ABSTRACT.** This block must be completed to assign a distribution limitation to the abstract. Enter UU (Unclassified Unlimited) or SAR (Same as Report). An entry in this block is necessary if the abstract is to be limited.

# **Macroscopic Crosslinked Neat Carbon Nanotube Materials and CNT/Carbon Fiber Hybrid Composites: Supermolecular Structure and New Failure Mode Study**

(AFOSR # FA9550-11-1-0131, Program Manager: Dr. Joycelyn Harrison)

## **Project Final Report**

**(Period of Performance: 01 July 2011 to 30 June 2015)**

**September 2015**

Dr. Richard Liang\*

High-Performance Materials Institute

Florida State University

Tallahassee, FL 32310

\* [zliang@fsu.edu](mailto:zliang@fsu.edu)

Dr. Ben Wang\*\*

Georgia Tech Manufacturing Institute

Georgia Institute of Technology

Atlanta, GA 30332

\*\* [ben.wang@gatech.edu](mailto:ben.wang@gatech.edu)



## CONTENT LIST

<b>Abstract</b> .....	<b>4</b>
<b>1. Mechanisms and Scale-up Process Development of Mechanical Stretching to Fabricate Highly Aligned CNT Materials</b> .....	<b>5</b>
1.1 CNT Alignment.....	5
1.2 Mechanical Stretching.....	6
1.3 Stretching Behavior of CNT Thin Films .....	8
1.4 Strain Hardening Estimation .....	10
1.5 Multiple Deformation Modes of CNT Networks .....	15
1.6 Large Stretching Strain for High Degree of CNT Alignment .....	20
1.7 Development of Scalable Stretching Process.....	21
1.8 Characterization of Degree of CNT Alignment .....	22
<b>2. Failure Modes and Geometrically Constrained Self-assembly and Graphitic Crystal Packing of Flattened and Aligned Carbon Nanotubes</b> .....	<b>26</b>
2.1 TEM and SEM Experiments .....	26
2.2 CNT Network Transformation .....	26
2.3 CNT Network Failure Mode.....	27
2.4 CNT Collapse and CNT/Resin Interface .....	29
2.5 Geometrically Constrained Self-assembly and Graphitic Crystal Microstructure.....	31
2.6 Molecular Model and MD Simulation of Packing Models of Geometrically Constrained Self-assembly and Graphitic Flattened CNTs.....	33
2.7 Twisting and Folding of Flattened CNTs.....	37
2.8 CNT Pullout Failure and CNT/resin Interface Bonding .....	38
<b>3. High Energy Beam and High Temperature Treatments of CNT Networks</b> .....	<b>40</b>
3.1 High Energy E-beam Irradiation .....	41
3.2 Low Energy E-beam with High Temperature and High Vacuum .....	43
3.3 Mid-Range E-beam Energy with Vacuum.....	43
<b>4. CNT Buckypaper/Carbon Fiber Hybrid Composites</b> .....	<b>45</b>
4.1 Permeability of CNT Buckypaper.....	47
4.2 Materials and Permeability Measurement Setup .....	48
4.3 Permeability Estimation Model.....	50
4.4 Permeability Results.....	52
4.5 Nanoscale Pore Characteristics-Permeability Relationships.....	56
4.6 Manufacturing Challenges of CNT Buckypaper/CF Hybrid Composites.....	60
4.7 Experimental .....	60
4.8 New Resin Flow Behavior and Manufacturing Challenges in Autoclave Process for BP/CF Hybrid Composites.....	63
4.9 Aerospace-grade Quality of CNT BP/CF Hybrid Composites.....	67
4.10 Tensile Properties and Failure Modes of CNT BP/CF Hybrid Composites.....	70
4.11 High Electrical Conductivity of CNT BP/CF Hybrid Composites.....	75
<b>5. Multiscale Model and Simulation of Buckypaper and Nanocomposites</b> .....	<b>75</b>

5.1 Coarse-grained MD Model of CNT Network Structures in Buckypaper ..... 76  
5.2 FEA for Modeling CNT Network Structure Change and Alignment Properties ..... 79  
**Conclusions ..... 82**  
**Acknowledgement ..... 83**  
**References..... 84**

## ABSTRACT

Carbon nanotubes (CNTs) demonstrate great potential for developing high-performance multifunctional materials due to their unique combination of exceptional mechanical, thermal and electrical and lightweight properties. In this project, we explored two novel low-density material systems to potentially realize the ultimate intrinsic properties of CNTs for scale-up applications: 1) continuous highly aligned CNT tapes or sheets and 2) CNT sheet/ carbon fiber hybrid composites (CNT/CF) with aerospace-grade quality and carbon fiber concentration.

We studied different approaches for engineering CNT networks in CNT thin films or buckypaper to achieve a high degree of alignment and graphitic crystal packing. By selecting extra-large aspect ratio ( $>100,000$ ) and small diameter (5-8 nanometers) double-walled CNTs and using load transfer media in CNT networks, we developed a unique mechanical stretching process to realize a high degree of alignment and graphitic crystal assembling CNTs to reduce packing defects in macroscopic assemblages of CNTs. The aligned CNT fraction in the resultant materials can be as high as 0.93, which is close to that of carbon fiber materials. We discovered that the unique geometrically constrained self-assembly and graphitic crystal packing of flattened and aligned CNTs can lead to close surface contact between CNTs to substantially improve the load transfer and mechanical properties. We also revealed that extremely low permeability ( $\times 10^{-17\sim-19} \text{ m}^2$ ) of CNT thin film or buckypaper materials could largely eliminate through-thickness flow of resin matrix during composite autoclave fabrication process. Modifications in the processing parameters and consideration of strong capillary resin absorption of CNT networks during CNT buckypaper/CF prepreg materials for hybrid composites are needed to fabricate aerospace-grade hybrid composites with 58 wt.% CNT and 5060 vol.% carbon fiber concentrations. The composites with CNT/CF alternative interply hybridization demonstrated promising mechanical/electrical multifunctional feature. Furthermore, strong CNT layers acted as effective microcrack arresting layers to potentially improve damage tolerance properties. The project results provide a new fundamental understanding of scale-up CNT applications in lightweight and multifunctional composites and structures.

# 1. Mechanisms and Scale-up Process Development of Mechanical Stretching to Fabricate Highly Aligned CNT Materials

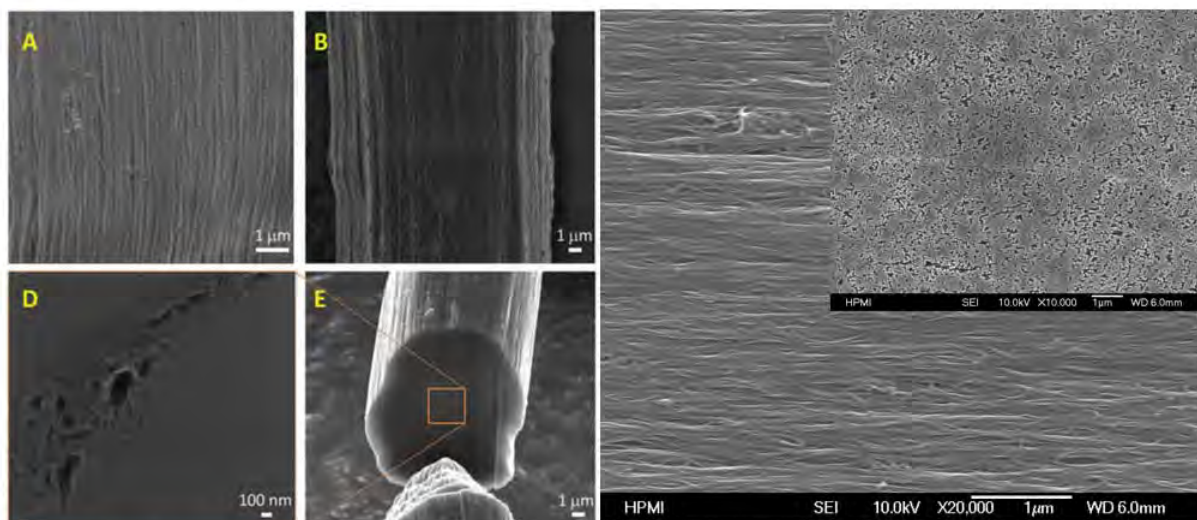
## 1.1 CNT Alignment

Carbon nanotubes (CNTs) have great potential as a new high performance material due to their high mechanical,<sup>1-14</sup> thermal<sup>10-14</sup> and electrical<sup>7,11-18</sup> properties. The tensile strength for an individual multi-walled carbon nanotube (MWCNT) has been measured between 11 and 63 GPa.<sup>1</sup> More importantly, CNTs are highly anisotropic in nature and similar to carbon fibers and Kevlar fibers. Those exceptional properties only exist along the CNT axial direction. For an example, when CNT networks of randomly oriented nanotubes are fabricated for scale-up applications, the theoretical high strength for individual nanotubes is far from being attainable due to many factors, with the lack of alignment in the network a major factor.

Many research groups have attempted different techniques to align CNTs in their networks. Some attempted methods involve using filtration to orient the CNTs while in suspension,<sup>13</sup> using argon gas flow to create flow induced alignment,<sup>19</sup> growing the carbon nanotube forest using chemical vapor deposition and plasma enhanced chemical vapor deposition to obtain natural growth orientation,<sup>3,20-28</sup> template/spinning techniques to aid in growth orientation,<sup>4,29-31</sup> melting processing methods<sup>32,33</sup> to achieve alignment via shear flow, polymerization encapsulation techniques to take advantage of electrical and thermal properties of aligned CNT sheets and CNT/polymer composites,<sup>5</sup> magnetic fields to induce alignment on a random film,<sup>34-40</sup> pushing a vertically-aligned nanotube “forest” down into an aligned sheet using shear pressing,<sup>6,41</sup> and mechanically stretching a CNT/polymer film using the polymer as a load transfer media before curing of a thermoset polymer or under heating for a thermoplastic polymer.<sup>7,16-18,42-45</sup>

Of the many methods attempted of CNT alignment, the most popular are magnetic alignment, CNT fiber by spinning, and mechanical stretching. Windle and co-workers implemented a twisting method that resulted in a tensile strength of 8.8 GPa and Young’s modulus of 357 GPa for a CNT fiber with 1 mm test gauge length<sup>9</sup> due to high alignment and dense packing of CNTs. The continuous spinning method was also used by Liu and coworkers by which they combined the twisting and condensing methods.<sup>46</sup> Pasquali’s group used a wet spinning method to produce very dense CNT fibers with highly aligned DWCNTs and less defects, achieving high tensile strength of 1 GPa and modulus of 120 GPa and electrical conductivity of 2.9 MS/m.<sup>47</sup> A similar stretch winding process was used by Zhu and his coworkers that resulted in a high CNT volume fraction nanocomposite with a tensile strength of 3.8 GPa and modulus of 293 GPa because of the dramatic improvement of alignment and dense CNT packing.<sup>48</sup> Our group used a mechanical stretching method of fabricating aligned CNT sheets that produced tensile strength of approximately 2.1 GPa and modulus of 169 GPa due to the improvement of CNT alignment and crystal-like packing.<sup>7,17</sup> Figure 1 shows two examples of dense packing and high degree of alignment of CNTs in both continuous CNT fibers<sup>47</sup> and mechanical stretched large CNT sheets.<sup>7,16-18</sup> These advances and results from discovering and studying dedicated CNT

assemblage microstructures toward developing high-strength materials are very promising. To fully utilize these methods to transfer the nanotube properties, exploring and understanding how the network is nanoscopically and macroscopically modified during the processes of alignment and the critical conditions to achieve high degree of alignment are necessary.



(a) Dense CNT packing in wet-spinning fiber

(a) Highly aligned CNTs in mechanically stretched CNT sheets

Figure 1. Highly aligned and dense packing microstructures of CNTs in high-performance CNT fiber (Pasquali<sup>47</sup>) and sheets (Liang<sup>7, 16-18</sup>)

The mechanical stretching process can be a cost effective solution for scale-up manufacturing of aligned CNT materials. A crucial intrinsic property that the random network of CNTs needs to possess in order to be stretched to achieve high degree of alignment is an extremely high aspect ratio ( $>100,000$ ) of each constituent nanotube.<sup>16</sup> Large aspect ratios allow the network with heavy molecular entanglement to withstand plastic deformation and the nanotube network to reach a high degree of alignment in its nanostructure, similar to carbon fiber and polymer molecules.<sup>8,9</sup>

## 1.2 Mechanical Stretching

A random network of CNTs forces uniaxial alignment can be stretched along the plane of applied force. The method of applying uniaxial force to a CNT/polymer matrix was first applied by Jin et al. in 1998 by casting CNTs with a thermoplastic polymer then stretching the product to vary the degree of alignment within the polymer/CNT composite. The resulting alignment was studied using X-ray analysis to find the produced morphology.<sup>42</sup> This method was further studied by Badaire et al. who found a correlation between elongation percentage and thermal/electrical property improvements (thermal: 3-4 factors larger, electrical: several orders larger).<sup>48</sup> Kim et al. studied the dispersion and alignment of CNTs in a gelatin film and the resulting

photoluminescence and highly polarized absorption properties that show promise in light-emitting materials.<sup>49</sup> Miaudet et al. showed that the principle of stretching/drawing a fiber was effective for inducing PVA crystallinity that increases toughness of the composite.<sup>43</sup> Wang et al. combined the spinning and stretching techniques by taking an aligned film and further stretching 2%, 4% and 7%, which showed additional straightening of the nanotube network resulted in ultimate strength increases of 50%, 150% and 199%, respectively.<sup>44</sup> Our group has shown that using randomly oriented millimeter long MWCNT networks with adding Bismaleimide (BMI) and applying uniaxial force before resin cure orient the nanotubes in sheets through strain-induced nanotube interactions,<sup>7,16-18</sup> as shown in Figure 2. They have shown a correlation between the elongation and aligned percentages and achieved improved mechanical properties when stretch percentage is larger. When chemical functionalization is added to this process, a ultra-high tensile strength of 3081 MPa and Young's modulus of 350 GPa can be achieved because of higher cross-linking induced by functionalization.<sup>7,16,17</sup>

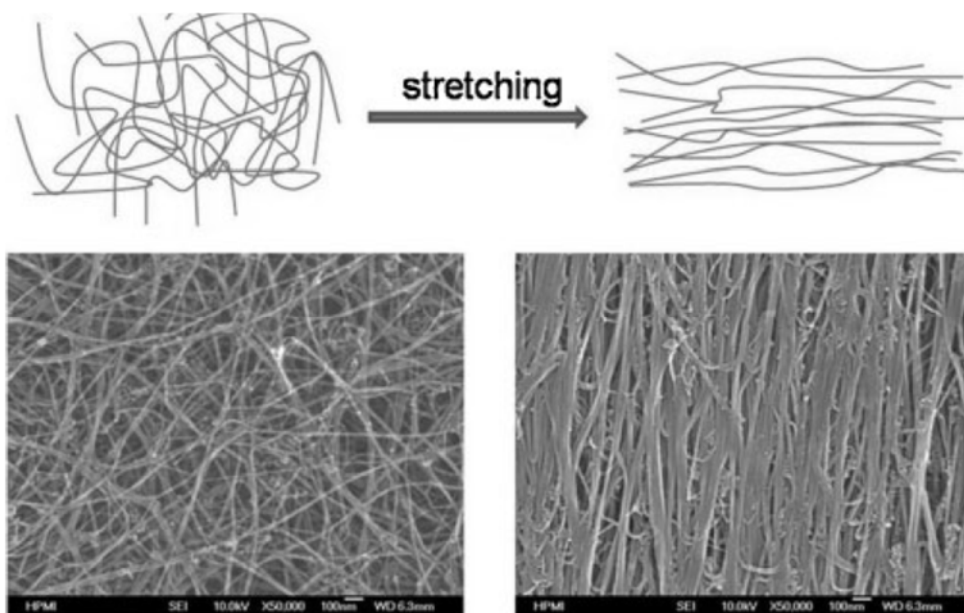


Figure 2. Schematic and corresponding SEM images of mechanical stretching to align nanotubes in a random MWCNT sheet<sup>7</sup>

Recently, Wang et al. went on to further improve the method using a matrix spray and stretching apparatus, which resulted in record-high strength of (3.8 GPa, Young's modulus of 293 GPa, electrical conductivity of 1230 S/cm and thermal conductivity of 41 W/mK. These advances are attributed to high aspect ratio, high volume fraction, high alignment and lowered waviness.<sup>45</sup> Also, Li et al. (Liang's group) produced modeling results of the stretch method on the degree of alignment using X-ray diffraction, Raman spectroscopy and electrical measurements, which show the structural evolution of the long CNT ropes during and after stretching.<sup>18</sup>

### ***1.3 Stretching Behavior of CNT Thin Films***

While many methods have been studied, the anisotropy on the nanoscale has not been adequately modeled or understood fully.<sup>14</sup> In this study, we will focus on the fundamental understanding of deformation mechanisms of CNT networks and the structure-property relationships of the aligned nanotube network at different deformation stages toward achieving high degree of alignment and developing scalable process.

Our research showed that the MWCNT networks can be modified via an applied uniaxial strain of up to 40% with uncured resin impregnation treatment (the resin as the load transfer media) to improve alignment and packing of the nanotubes.<sup>50</sup> The ductility of the network largely relies on the high aspect ratio of millimeter long nanotubes, high waviness and locking points from residual catalyst nanoparticles and use of load transfer media. The original random network (supplied by Nanocomp Technologies, NH) shows low density, strength and modulus and only able to stretch to about 20-30% strain due to lack of ductility.<sup>16</sup> The stretching process is highly scalable and the resultant materials have great potential for high-performance composite applications.

Figure 3 shows the microscale evolution of the CNT networks from random orientation to a densely packed microstructure with heavily bundled “ropes” and an improved alignment degree in the horizontal direction – the direction of strain. Figure 4 shows the stress-strain responses during the stretching process of both the neat CNT network and resin impregnated network. Once the uncured polymer materials are impregnated to the neat CNT sheets, an identical procedure for applying uniaxial tensile strain of the neat sheets was used. Figure 4 shows the treated CNT sheets experienced a unique stress response with increasing strain. The two samples with the resin treatment not only were able to withstand strains of up to 40%, but also showed a more dramatic necking phenomena which suggests increased orientation and crystallization within the necking region. Figure 3 (f) of the 40% stretched resin treated CNT sheet shows a dramatic improvement in the alignment and CNT self-assembly into large bundles.

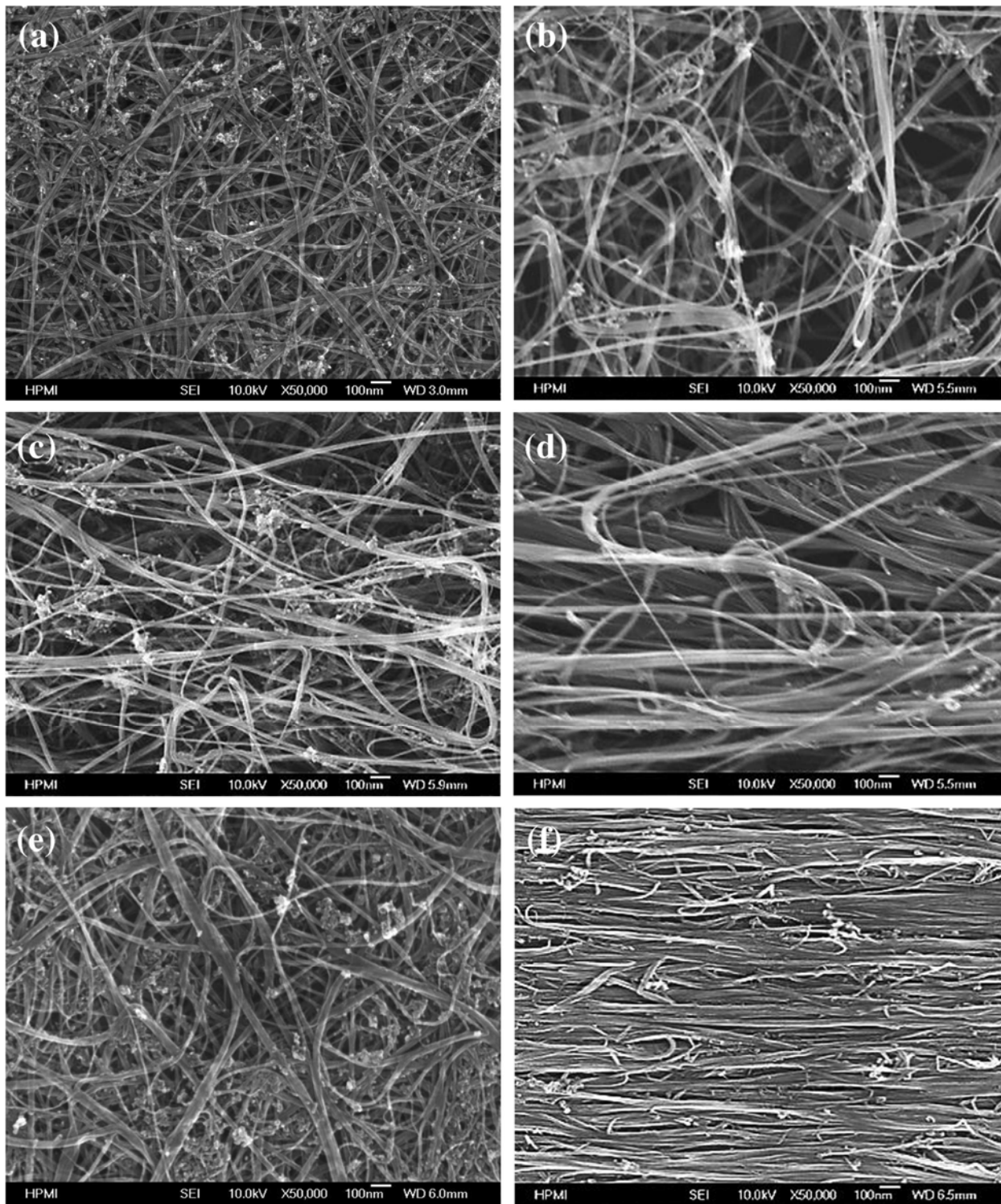


Figure 3. SEM images of neat (a-d) MWCNT networks at strains of 0% (a), 10% (b), 20% (c) and 30% (d), and resin treated (e-f) MWCNT networks at strains of (e) 0% and (f) 40%. The strain direction in all images is lateral

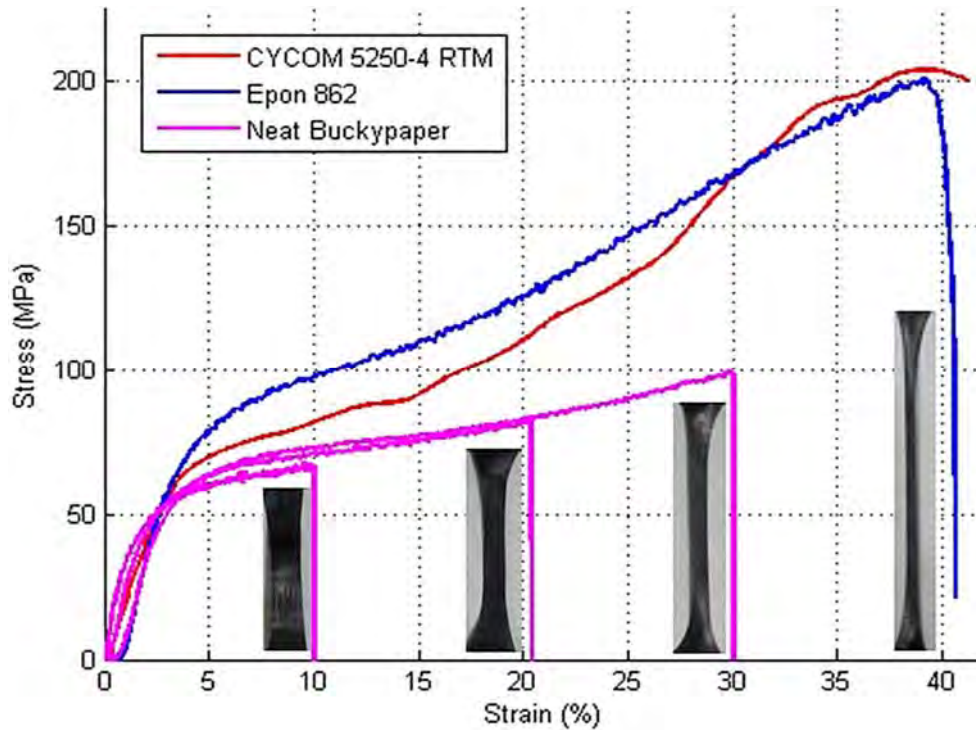


Figure 4. Typical mechanical stress/strain curves, and sample morphology produced by the MWCNT sheets being strained to 10%, 20%, and 30% and the resin treated samples strained to 40%

The staged-strain deformation for the MWCNT networks was further studied by consecutively applying stage strains, as shown in Figure 5. The results show how the sample of neat CNT network was initially deformed to >20% as denoted by Neat Stretch #1. When the same pre-deformed sample was strained two additional times – denoted by Neat Stretch #2 and #3 – the force dynamic of each consecutive strain showed a two-stage deformation feature, and the onset change force corresponded well to the previous maximum stretching force. It was interesting that the maximum force applied aligned with the next deformation transition from elastic to plastic deformation. The high modulus of the elastic portion enhanced the interactions and load transfer among CNTs and created densely packed and large bundles along the stretching direction. This microstructure change due to additional alignment and self-assembly of CNTs through supplementary plastic deformation resulted in further increases in the tensile strength and modulus with each additional amount of strain applied.

#### 1.4 Strain Hardening Estimation

To account for the cross-sectional area decreasing and necking of CNT networks, true stress/strain curves were created based on the experimental results. True stress ( $\sigma_T$ ) assumes material volume remains constant and is determined by the instantaneous load acting on the actual cross-sectional area.<sup>51</sup> True strain ( $\epsilon_T$ ) is the rate of instantaneous increase in gauge

length. The following equations are for the constant volume assumption, true stress and true strain:

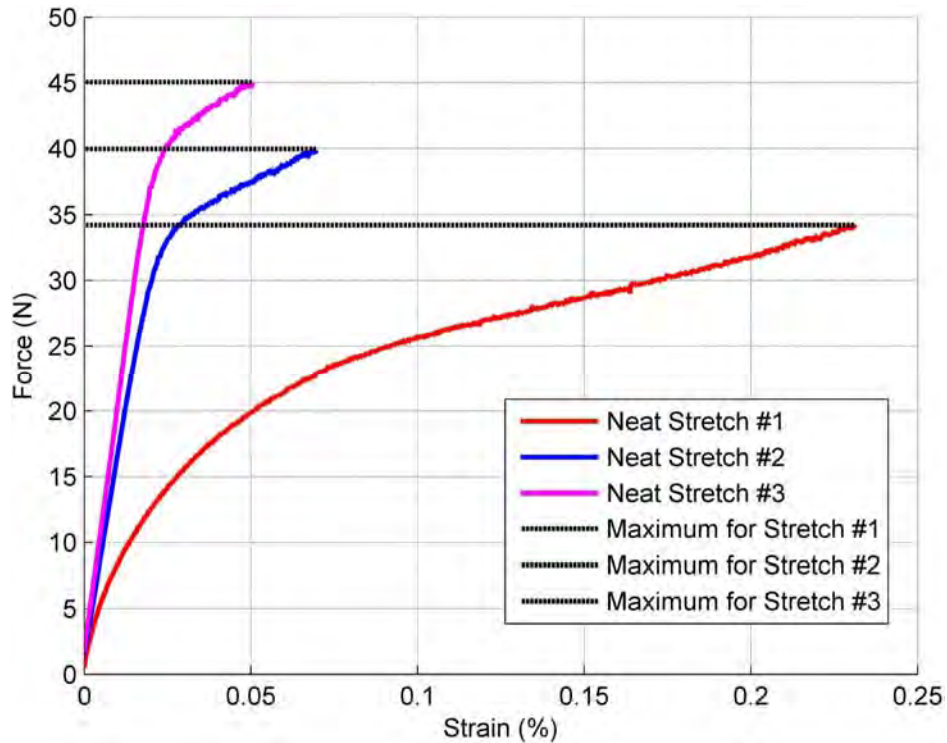


Figure 5. Force-strain curves when a neat CNT network sample is strained over 20% the first time, allowed to relax, then placed back on the tensile machine and stretched two additional sequential times of at least 5% strain. Dashed lines represent the maximum of the previous strain application and how it corresponds to the next stage of stretch

$$A_o \ell_o = A \ell \quad (1)$$

$$\sigma_T = \sigma_E (1 + \varepsilon_E) \quad (2)$$

$$\varepsilon_T = \ln(1 + \varepsilon_E) \quad (3)$$

where  $A$  is cross-sectional area,  $\ell$  is sample gauge length,  $P$  is applied load,  $\sigma_E$  and  $\varepsilon_E$  are engineering stress and strain, respectively.<sup>51</sup> Figure 6 shows the true stress-strain curves for stretching the neat and polymer treated samples. A high percentage in deformation resulted in a notable characteristic strain hardening increase in slope,<sup>52</sup> like cold worked metals.<sup>49</sup> This result indicates the stretching process also straightens the bundles and ropes of CNTs, resulting in closer packing, which reduces voids and porosity, thereby improving the mechanical properties and minimizing defects.

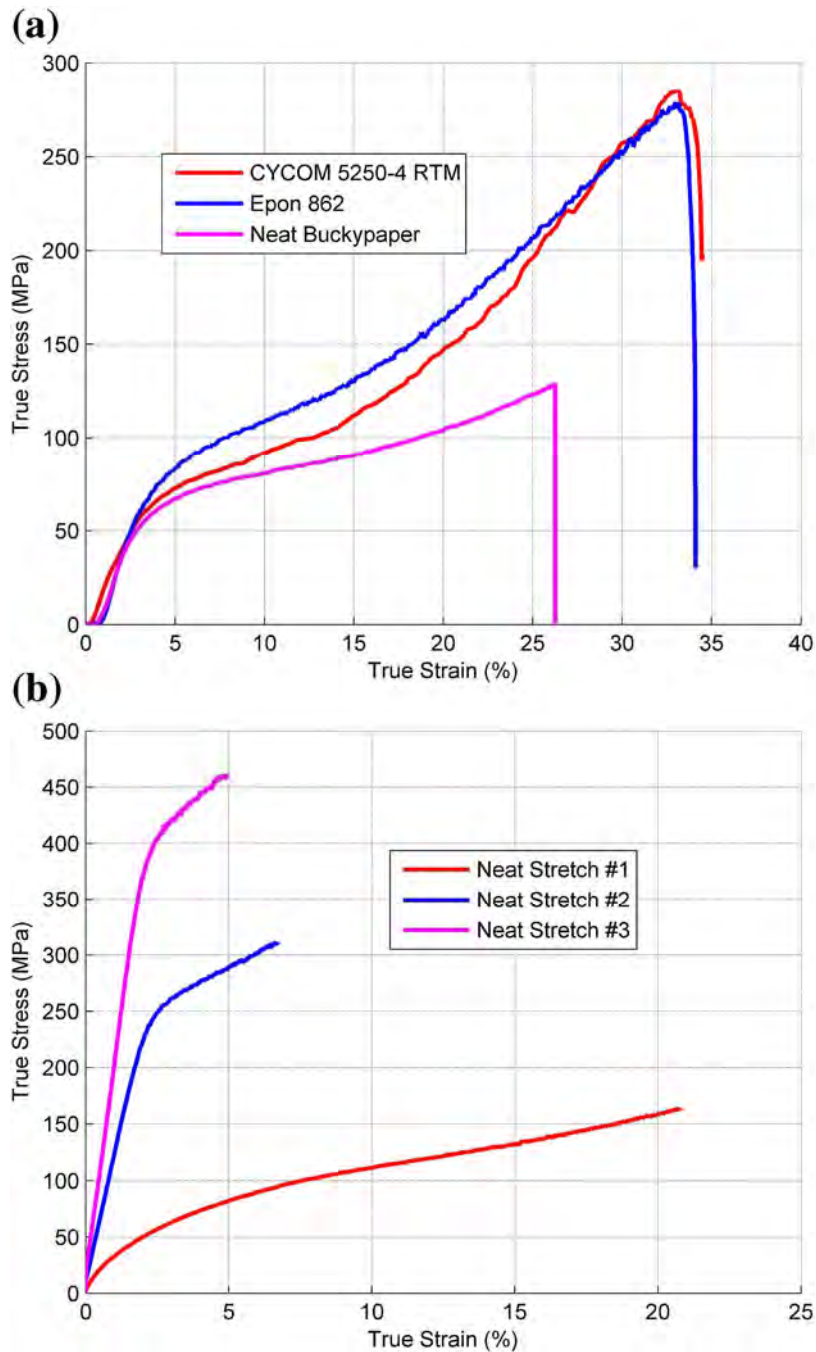


Figure 6. True stress/strain curves of drawing procedures for the initial strain of neat CNT and resin treated materials from Figure. 4 and true stress/strain curves for re-straining neat CNT material from Figure. 5

The nanotube networks' structural evolution and stress-strain behaviors are similar to those of polymer materials.<sup>2,52,53</sup> The stress-strain behaviors of the bilinear elastic/plastic deformation of

the networks, as shown in Figures 6, were similar to thermoplastic polymers during the drawing procedure. The difference is that the CNT sheets did not undergo a stress reduction after onset of necking, compared to typical polymer stretching deformation. This is mainly due to dramatic increases of CNT alignment and assembled into large bundles, and the nanostructure of the nanotube network was slightly more brittle than that of the plastic polymers. The response of the CNT networks can be described as a combination of the cross-linked brittle polymer and the fibrillar plastic polymer stretching behaviors.<sup>52,53</sup> The mechanism of thermoplastic deformation strengthening is that the alignment and crystallization of the long molecular chains increases toughness and strength along the alignment direction, whereas metal drawing has the strain hardening mechanism.<sup>54</sup> In traditional metal strengthening, cold working was used to deform the metal below the recrystallization temperature.<sup>54</sup> Cold working involves applying a stress greater than the yield stress to create plastic deformation and rearrange microstructures. In our study, repeating the procedure resulted in higher strength, lower ductility and brittle behavior of the material due to the creation of CNT crystalline and orientation order along the axial direction, as shown by Figure 5. When tensile strain was applied to the material and necking commenced, a complex stress distribution and concentration were induced on the material, and the true stress-strain curve from the start of plastic deformation was approximated by the following relationship.<sup>54</sup>

$$\sigma_T = K\varepsilon_T^n \quad (4)$$

$$\frac{\sigma_T}{\varepsilon_T} n = \frac{d \sigma_T}{d \varepsilon_T} \quad (5)$$

$$0 \leq n \leq 1 \quad (6)$$

where K is the strength coefficient and n is the strain hardening parameter. A low n value corresponds to a poor response to cold working. A greater strength in metals corresponds to a larger number of dislocations while a greater strength in thermoplastic polymers denotes a long-range order and crystallization of long molecules due to the van der Waals bonds being broken and the polymer chains being dislocated.

The n and K coefficients of the CNT network deformation were computed based on Figure 6 and are shown in Table 1. The n and K values for the staged strain experiment in Figures 5 and 6 show that most of the CNT morphology reconstruction occurred in the first ~20% of strain. The resin treated sample's greater alignment, which is shown in Figure 3, was due to the increase of over 160% for n values and over 200% for K values when compared with neat CNT network. A

similar treatment process was applied to the Epon and Cytec treated CNT networks that allowed for greater elongation and held the treatment variations as negligible. A possible reason for the different resin treated samples expressing similar n values would be that both resin treatments allow for a similar degree of alignment, locking angles and sliding friction between the CNTs that caused the hardening of the network. For FCC metals, the n value is roughly 0.5, where the n value for BCC metals is roughly 0.15. Table 2 shows the typical n and K values for some materials.<sup>51,52</sup> The n values when the neat CNT material was re-stretched is comparable to BCC metals outperforms that of the baseline polycarbonate. The polymer treated strain hardening values were above that of FCC metals, which showed an intense response to stretching deformation due to the unusual strong self-assembly nature of CNTs.<sup>52</sup>

Table 1. Strain hardening parameters for CNT networks straining tested in this work

CNT Network Type and Strain %	n	K (MPa)
Neat CNT - Initial strain to 23%	0.49	162.03
Neat CNT - Re-strain 1 to 30%	0.22	310.84
Neat CNT - Re-strain 2 to 35%	0.19	460.58
Epon Treated CNT - Strain to 40%	0.63	272.83
Cytec Treated CNT - Strain to 40%	0.65	304.78

Table 2. Strain hardening parameters for common materials<sup>51,52</sup>

Material Type	n	K (MPa)
4340 Steel Alloy (tempered at 315 °C)	0.12	2650
AZ-31B Magnesium Alloy (annealed)	0.16	450
2024 Aluminum Alloy (heat treated - T3)	0.17	780
Low-carbon Steel (annealed)	0.21	600
Naval Brass (annealed)	0.21	585
304 Stainless Steel (annealed)	0.44	1400
Copper (annealed)	0.44	530
Polycarbonate	0.15	10

## 1.5 Multiple Deformation Modes of CNT Networks

### 1.5.1 Deformation due to elongation and lowered waviness

For this mode of the network's deformation, during the application of uniaxial strain, the individual nanotubes and their bundles undergo uniaxial stress at each end and become straighter and aligned to the stress vector.<sup>18</sup> Raman shift measurements of the G-band peak are known to reveal the orientation of the nanotubes.<sup>18,54,55</sup> The measurements show that the scattering signal was polarized along the oriented nanotube axis. Although the Raman measurements were limited to the surface of the material to ~50 nm surface depth (approximately 1015 nanotube layers), the measurements can be considered representative of strain-induced orientation of the nanotubes throughout the material.<sup>15,37,54–56</sup> The polarized Raman spectra was measured first with the polarization parallel to the strain-oriented direction ( $\theta = 0^\circ$ ) then perpendicular to the strain-oriented direction ( $\theta = 90^\circ$ ). The G-band intensity ratios between the two directions were calculated, as shown in Figure 7. The increase in the degree of alignment as the strain percentage increased shows that as the network was plastically deformed, the surface nanotubes were more aligned and showed a polarized response in direction of alignment. Both the neat CNT and polymer treated CNT networks showed good alignment response in the Raman intensity ratio/alignment degree calculations. However, the polymer treated sample was able to achieve a higher alignment response at the same deformation levels, as shown in Figure 4.

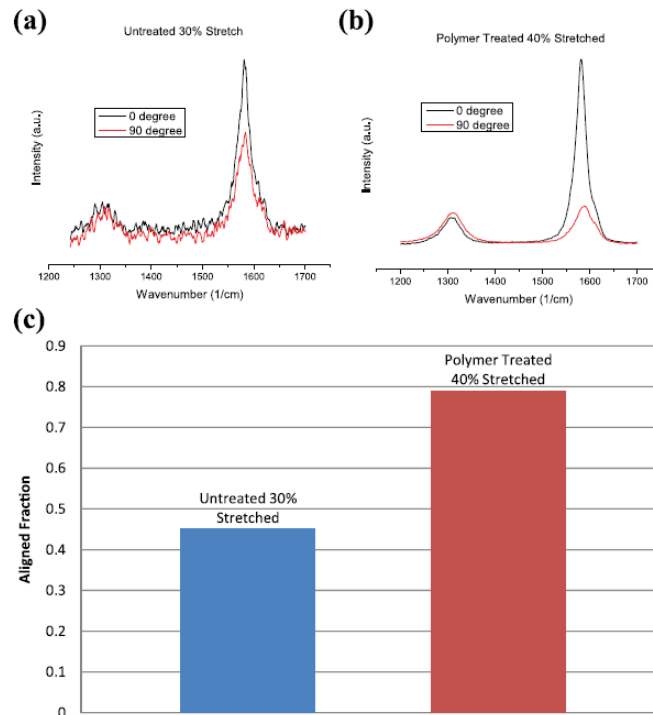


Figure 7. Raman spectroscopy measurements for (a) untreated CNT network at 30% strain, (b) polymer treated CNT network at 40% strain, and (c) alignment degree (denoted as a fraction) calculated from G-band intensity ratios along parallel and perpendicular polarizations to the stretching direction

### 1.5.2 Sliding friction along parallel nanotubes leading to straight CNTs and re-assembly into big bundles

The sliding friction mode under tension for the CNTs under tensile strain is the axial translation of individual nanotubes and nanotube bundles in proximity close enough to activate friction forces. This mode of tension is most prominent at about 20% strain in the neat CNT network, as shown in Figure 8. The nanotubes that were once perpendicular to the axis of orientation are now closer to being oriented parallel to the tensile direction. This change in orientation causes friction between unoriented perpendicular nanotubes and also between co-oriented parallel nanotubes. Alignment of adjacent small bundles self-assembled into large bundles or crystalline bundles, as shown in Figure 8.

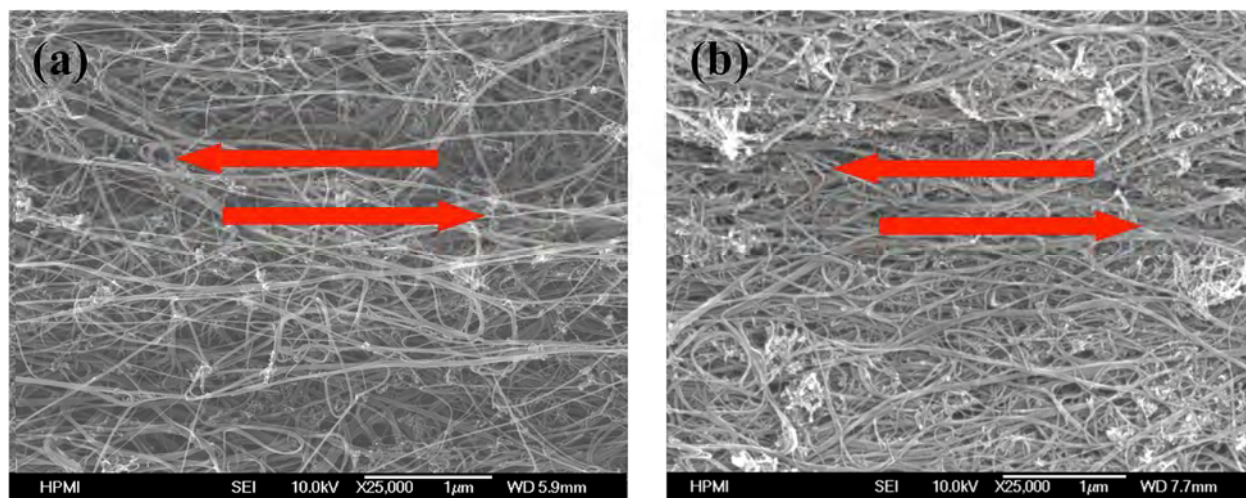


Figure 8. SEM images of neat MWCNT (a) and polymer treated MWCNT (b) networks at a 20% strain. Arrows indicate strain direction

### 1.5.3 De-bundling and hook stretching to align CNTs

Additional tension occurred due to bundles of CNTs either releasing from a bundle or reassembling into another bundle. This was most evident through examining SEM images and estimating bundle size. From Figure 9 shown in red squares, the loose bundle in (a) was a diameter of  $\sim 2 \mu\text{m}$ , while the bundle in (b) had a diameter of  $\sim 1 \mu\text{m}$ . This reduction in bundle size is contributed to the nanotubes being peeled from the bundle and the nanotubes becoming more intertwined to form large aligned bundles. The polymer treated sample showed the de-bundling mechanism, as seen in the change from (c) to (d). However, the bundles experienced a more predominant bundle sliding and relaxation rather than tightening. The stress leads to the de-bundled alignment along the stretching direction.

While hooked CNTs/CNT bundles accounted for a small portion of the stress, the ultra-long nature of the individual CNTs resulted in a hook behavior. This characteristic is the planar form of the self-folded morphology shown in CNT fibers, as shown by Lu and Chou.<sup>57</sup> The hook tail diameter was shown to be inversely proportional to the amount of stress needed to modify the

network, as shown in Figure 9. Due to high flexibility of CNTs, under the tension stress, the hooked or catalyast locked CNTs can well be aligned along the stretching direction.

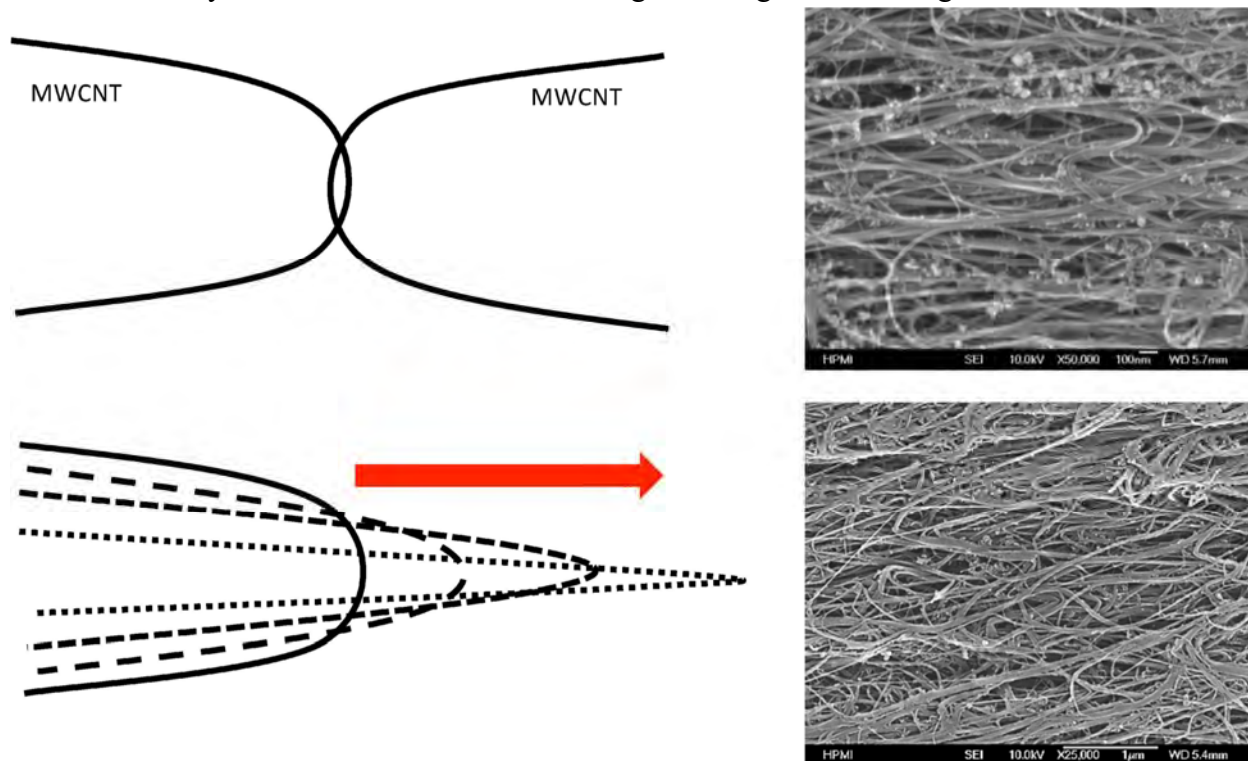


Figure 9. Entanglement modeling of open folded CNT stress as stress is applied to tail ends of CNTs

#### 1.5.4 Self-assembly and packing

The individual nanotubes and bundles came closer together due to the van der Waals attraction and reassembled into larger bundles to form a denser network. The densification of the CNT networks resulted in a better load transfer from a decrease in void content and activation of strong van der Waals interaction between individual nanotubes. Figure 9 also shows the extreme densification of the bundles that occurred between 20% and 30% strains. Figure 9 shows that the ropes formed in the 30% strain sample were larger than the looser ropes in the 10% sample. This formation of the large rope structure is the key to strengthening the nanostructure by improving load transfer between nanotubes. More than 30% reduction in width at the 30% strain also reflects the dense packing as shown in Figure 10. The shiny surface morphology seen in Figure 11(a) illustrates a similar optical phenomenon to the Raman measurements with increasing reflectivity correlated to increasing nanostructure alignment. The resin-treated 40% strained sample showed less optical reflection than the 30% untreated sample. While the density of the resin-treated 40% sample was higher than that of the 30% untreated sample, the treatment and purifying stages needed for the resin-treated sample caused the surface to show less reflection. Figure 11 shows how the strain process increases the nanotube density of the network by observing cross sectional nanotube packing from 10% to 40% strain elongation of a polymer treated and purified sample.

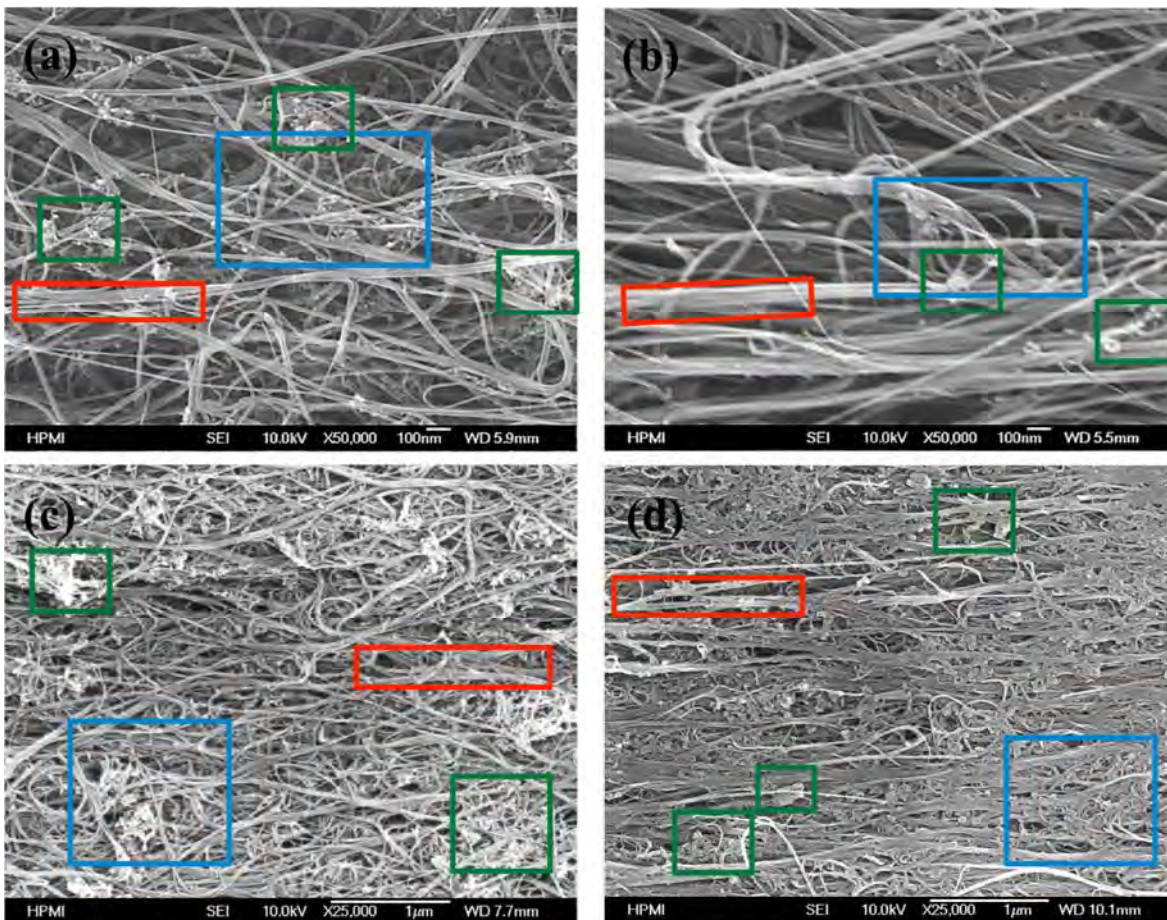


Figure 10. SEM images of Neat MWCNT networks at strains of 20% (a), 30% (b). Polymer treated 20% (c) and 40% (d). Red rectangles indicate CNT ropes that show a different amount of individual nanotubes in large bundles for different strains. Blue squares indicate bundle size and assembly changes. Green squares indicate defects and residual catalyst nanoparticles

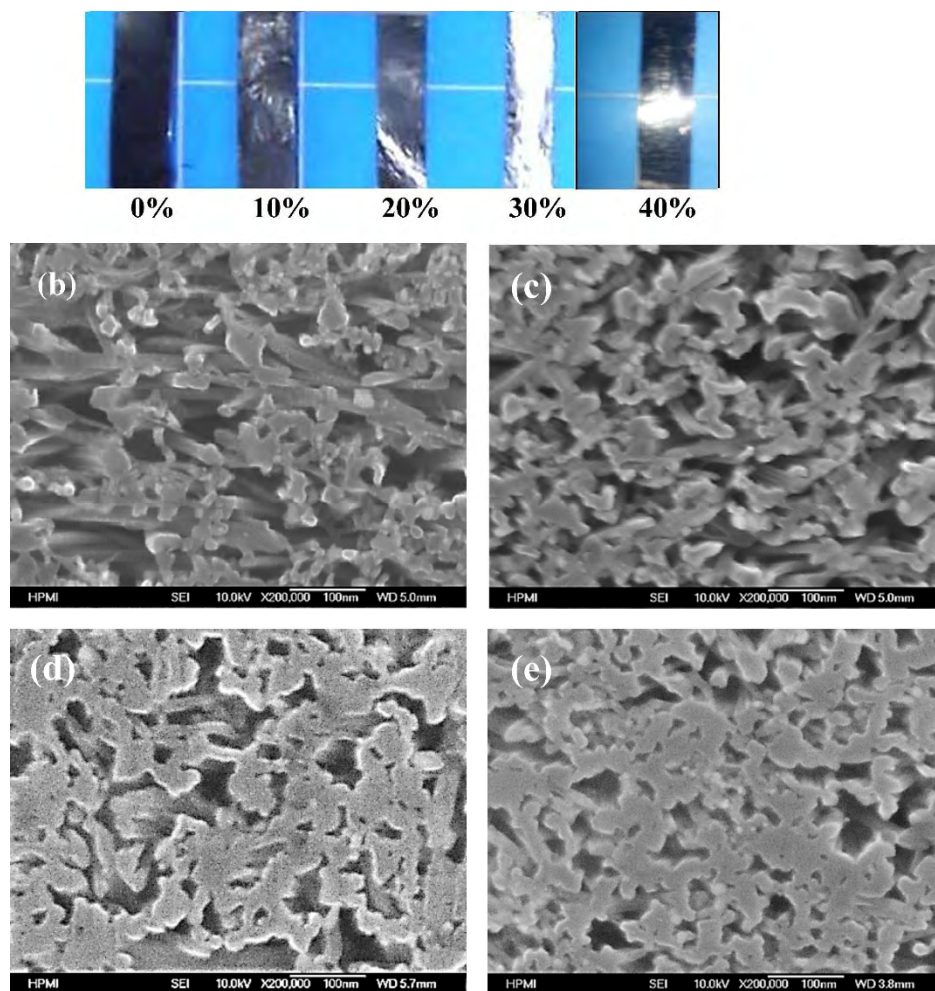


Figure 11. Surface morphology of stretched neat MWCNT networks with 0%, 10%, 20%, 30% and 40% strains (a). SEM cross-section images showing material density of MWCNT networks at strains of 10% (b), 20% (c), 30% (d) and 40% (e)

### 1.5.5 Catalyst locking of CNTs to enhance load transfer during stretching

In the MWCNT sheet materials as they were manufactured, significant amounts of residual catalyst nanoparticles were found. This mode of tension deformation accounts for the individual nanotubes and nanotube ropes dragging and pulling over the imperfections during stretching. As seen in Figure 10, the nanotube bundles in the neat sample in (a) and the nanotube ropes in (b) were pulling and entangling with the catalyst nanoparticle as indicated by the green squares. Another important phenomena occurring was the creation of a locking angle between CNTs. The locking angle was formed by the catalyst intersection point between CNTs causing a simultaneous imperfection and assistance for strain relaxation. The dragging friction was also a cause of failure in the networks due to possible stress concentration at the locking points. The dramatic increase in catalyst and various particles in the polymer treated samples in (c) and (d) indicates how the adhesion of the polymer particles on the nanotube locking points causes a better alignment during stretching deformation.

### 1.6 Large Stretching Strain for High Degree of CNT Alignment

With the further improvements of the stretching process, the CNT networks impregnated with BMI and epoxy resin systems can be stretched up to 80% strain without breaking. As seen in the SEM images in Figure 12, the degree of alignment of the CNT sheet can be dramatically improved with the resin-assisted stretching. High degrees of alignment were apparent in both the 60% and 80% stretching strain cases in Figure 11; however, there was an apparent lowered waviness with the 80% case due to self-assembly and CNT sliding.

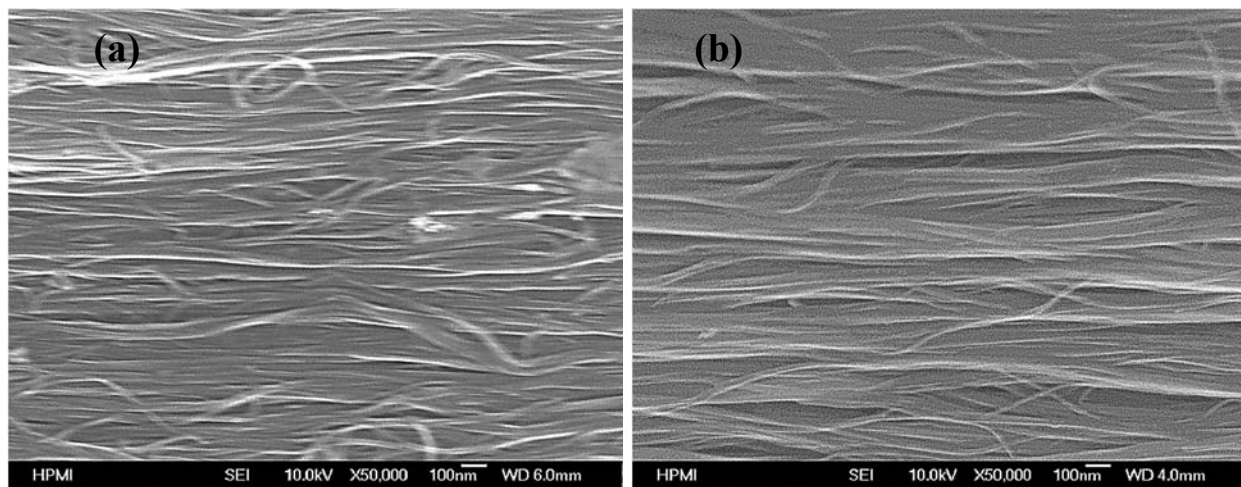


Figure 12. SEM images of 60% strain stretched buckypaper with BMI resin treatment (a) and 80% strain stretched buckypaper with BMI resin treatment (b)

The mechanism of strain strengthening in CNT networks was previously discussed. By controlling the viscoelastic properties of the applied resins to enhance load transfer, we successfully achieved such high stretching strain to realize a high degree of CNT alignment. Similarly, the metrics for strain hardening  $n$  were calculated using the true stress/true strain curves from the stretching procedure, as shown in Figure 13(a). The alignment degree was calculated based on Raman spectrum results from the resultant films as previously discussed. The strain hardening parameter,  $n$ , was shown to have a positive correlation with the alignment degree, as shown in Figure 13(b). The new strain hardening  $n$  values for the 60% and 80% strain stretched thin films were comparable to those of traditional materials in Figure 13(c), and the BMI treated 80% stretched CNT film showed a strain hardening parameter of more than 80% higher than that of traditional metals.

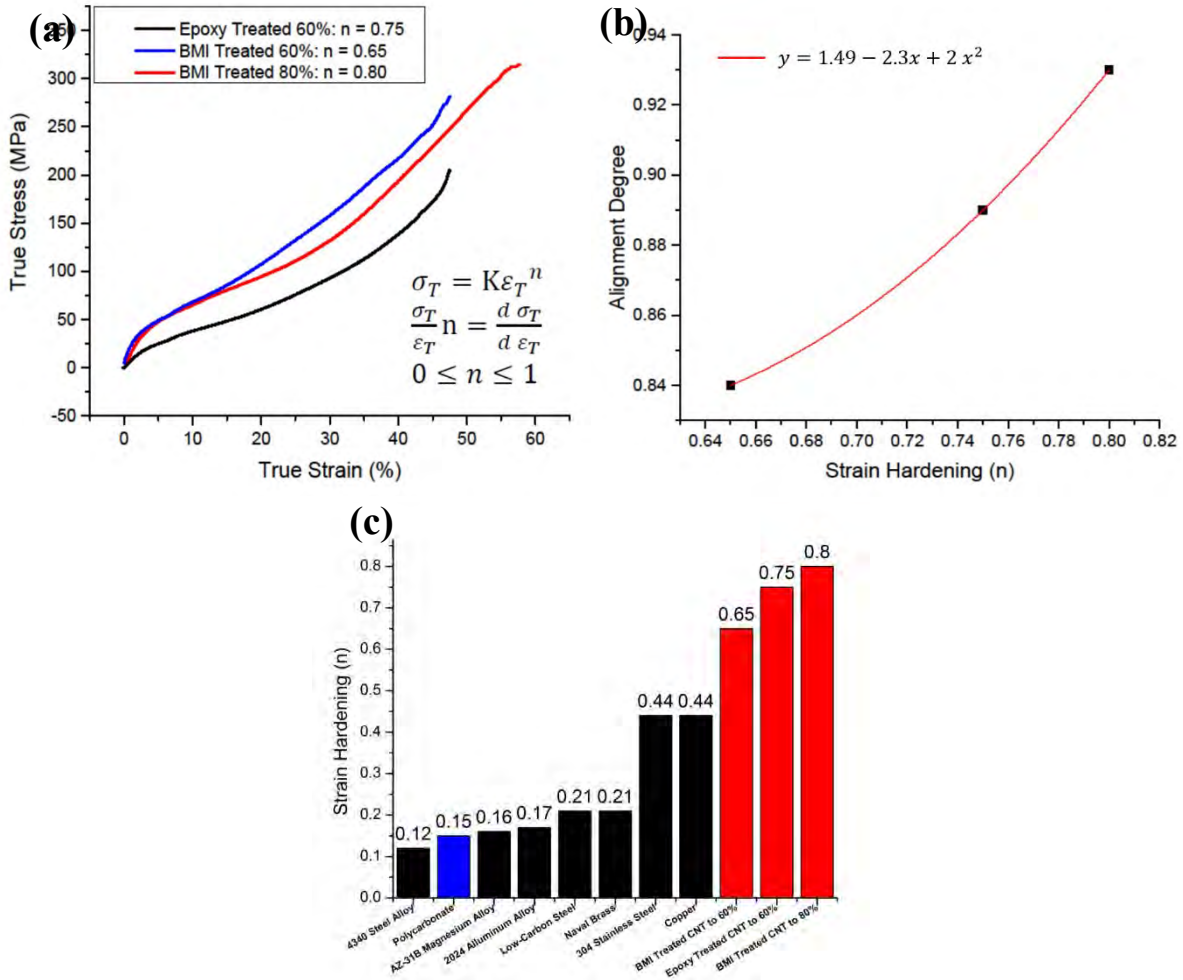


Figure 13. True Stress/True Strain curves for stretching the BMI (to 60% and 80% strain) and Epoxy treated CNT materials to 60% (a), the resultant strain hardening parameter  $n$  vs. the alignment degree and the fitted model (b), and the resultant strain hardening parameter  $n$  for various metals (black bars), polymer (blue bar) and the BMI and epoxy treated CNT materials (red bars) (c)

### 1.7 Development of Scalable Stretching Process

Our unique and patented stretching method<sup>50,58</sup> was scaled to a continuous process to potentially accelerate technical transfer into real-world engineering applications. Figure 14 demonstrates large and stable plastic deformation after uncured resin (load transfer media) treated CNT networks, and transforming random CNT networks into 10-foot long tapes of aligned CNTs achieved by our proprietary continuous stretching process. We also successfully produced and provided these continuous tape materials of highly aligned CNTs to industrial and government programs.

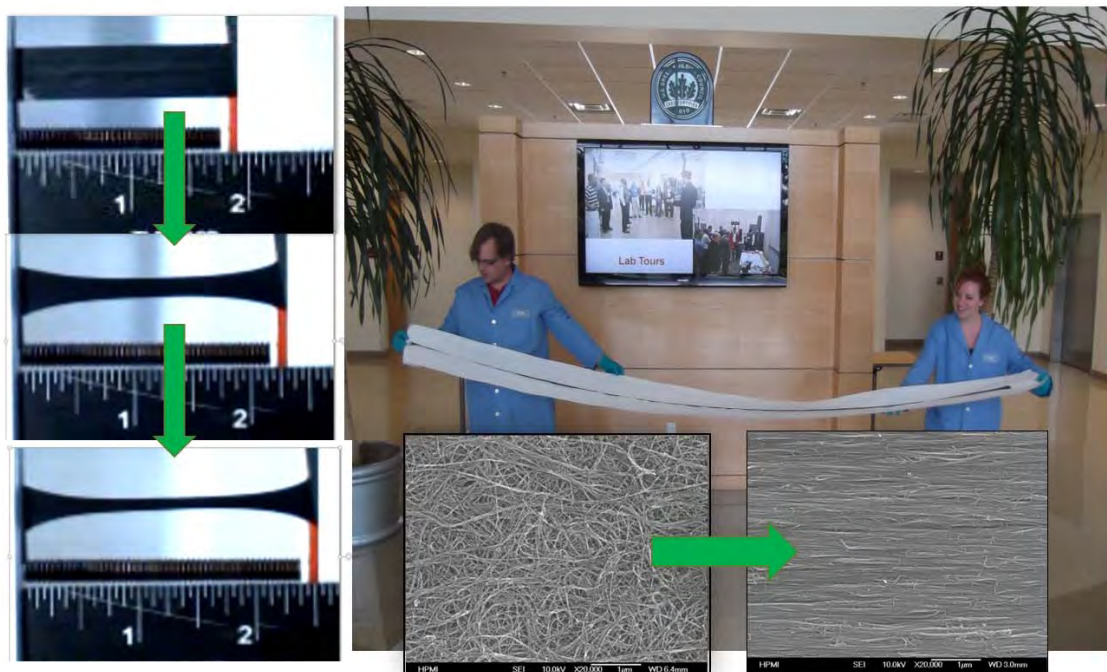


Figure 14. Scalable mechanical stretching process to produce a 10-foot long highly aligned CNT tape sample

### *1.8 Characterization of Degree of CNT Alignment*

To better understand CNT alignment and packing changes under stretching, we studied CNT network microstructure changes under tensile strains using in-situ X-ray and Raman scattering techniques.<sup>18</sup> Specifically, in-situ X-ray experiments were able to monitor relatively large sample areas (up to  $10 \times 10 \text{ mm}^2$ ), which is valuable for discovering the uniformity of microstructures of CNT networks, as shown in Figure 15. The results show that the process of stretch-induced alignment of CNT networks resulted in straightening the waviness of the long nanotube bundles, self-assembling and denser packing of the nanotubes into graphitic crystal structures or large bundle assemblages. In Figure 15, the evolution of the anisotropy of the stretch-aligned network can be clearly observed from the arc-shaped (002) peak as the strain increased. This dramatic intensity increases the close-packing (CP) peak at the lower angle of  $5^\circ < 2\theta < 8^\circ$  indicating the formation and growth of long-range order of graphitic crystals.<sup>30</sup> Both Raman and X-ray analysis were used to detect and quantify degrees of alignment of CNTs in materials.<sup>4,39,55,59–65</sup>

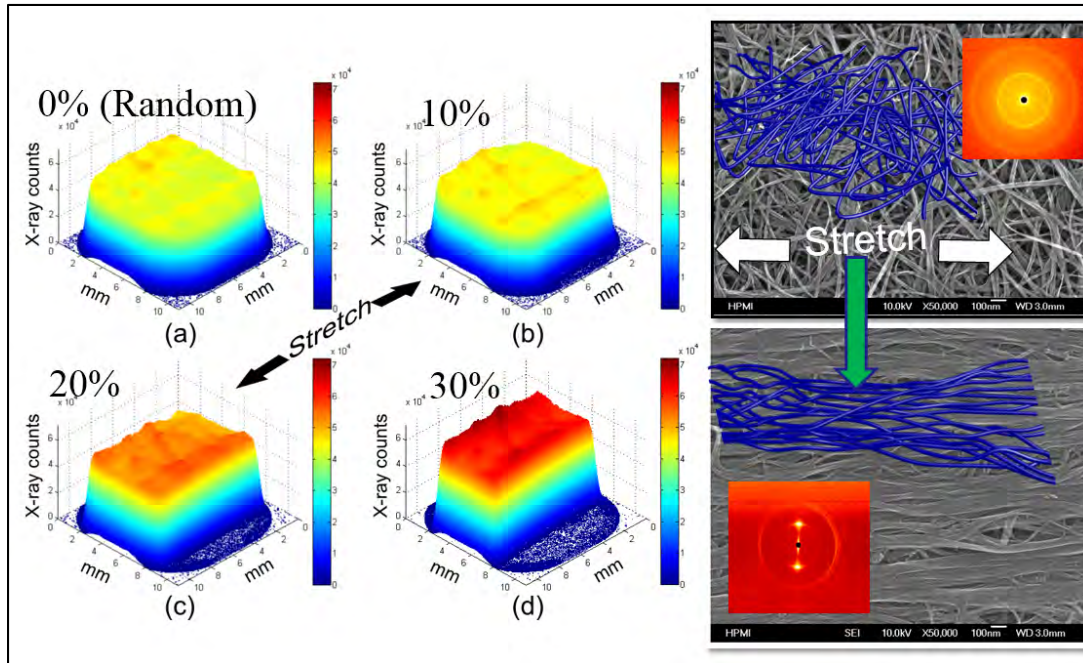


Figure 15. Microstructure evolution of CNT network under tensile strain: 1) (a)-(d) showing X-ray intensity due to both alignment and close-packing increase of CNT networks under different tensile strains; 2) the cartoon drawings showing change of both waviness and formation of closed-packing big bundles of CNTs during stretching, and the SAXS results indicting the formation of highly anisotropic graphitic crystal during stretching

For this study,<sup>18</sup> we used the randomly oriented CNT sheets supplied by Nanocomp Technologies Inc. (Concord, NH). The CNT sheets or networks (NTN) were cut into rectangular shapes of  $1 \times 4 \text{ cm}^2$ . The samples (2 cm in gauge length) were mounted onto an Anton Paar TS-600 tensile stage, which allowed the in-situ investigations of the straining process using both X-ray (Figure 16a) and polarized Raman scattering techniques (Figure 16b). The TS-600 stage has a window of  $15 \times 15 \text{ mm}^2$ , which allows the X-ray beam to impinge on the sample. However, when used inside the micro-Raman system, the laser beam was not limited to this scope as the stage was mounted with the sample facing the objective lens.

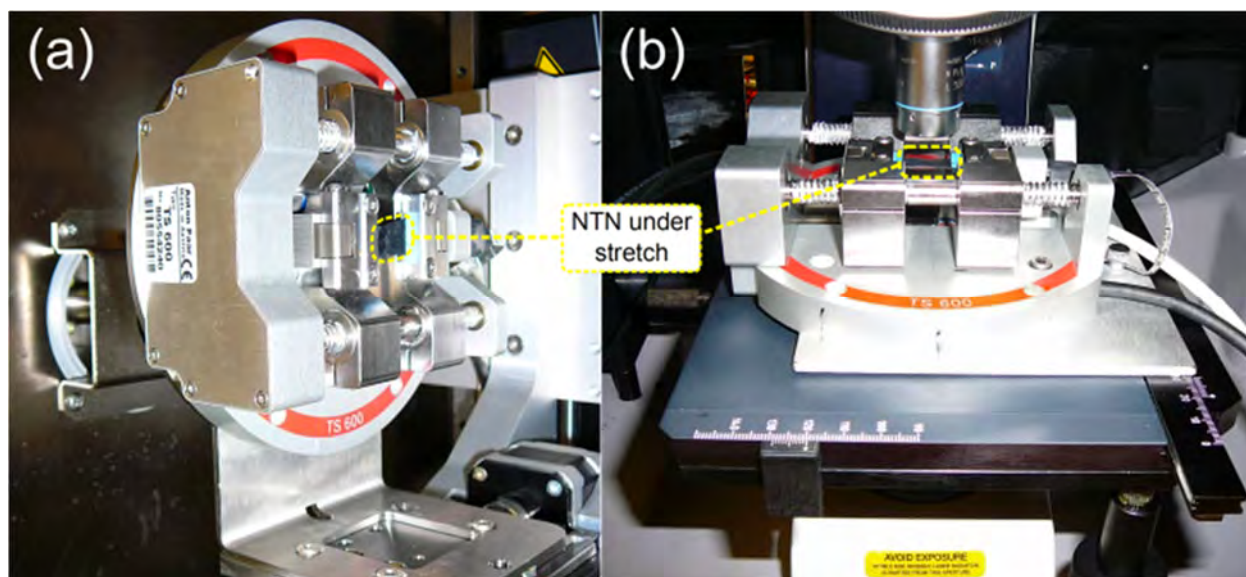


Figure 16. Experimental setup for the in-situ characterization of the CNT network (NTN) structural evolution during stretching: (a) The TS-600 tensile stage installed inside the sample chamber of the Bruker Nanostar system; (b) The TS-600 stage mounted on a Leica manual two-dimensional XY stage inside the sample chamber of the Renishaw inVia micro-Raman system

The small angle X-ray scattering (SAXS) and wide angle X-ray diffraction (WAXD) measurements were performed on a Bruker NanoSTAR system with an Incoatec  $\mu$ S microfocuss X-ray source operating at 45 kV and 650  $\mu$ A. The primary beam was collimated with cross-coupled Göbel mirrors and a pinhole of 0.1 mm in diameter, providing a Cu  $K\alpha$  radiation beam ( $\lambda = 0.154$  nm) with a beam size about 0.15 mm in full width half maximum (FWHM) at the sample position. The small-angle scattering intensity was measured on a two-dimensional multiwire Hi-STAR detector. The wide-angle diffraction intensity was captured by a Fuji Photo Film image plate and read with a Fuji FLA-7000 scanner. The in-situ Raman spectroscopic characterization was carried out on a Renishaw inVia micro-Raman system using a 785 nm excitation wavelength (1.58 eV) diode laser. Typical laser power was 0.5 mW with a 50 $\times$  magnification objective lens, and the laser beam size was around 10  $\mu$ m. Polarized Raman spectra were obtained in the VV configuration. In order to characterize the inhomogeneity of the NTNs, an adaptor was custom made to carry the TS-600 tensile stage on a manual Leica two-axis stage in the Renishaw system. The mapping was then obtained from repeated Raman measurements on the sample at 3 mm intervals along the stretch direction and 2 mm intervals in the normal direction.

As shown in Figure 15, as the strains increased, most of the stretched network would align along the preferred axis, with the exception of the ropes on the edges that started to crack and deviated from the preferred orientation. Compared to the alignment of shorter CNTs in strong magnetic fields where the tubes are rotated to change their orientations toward the preferred axis,<sup>63</sup> stretching-induced alignment of long CNT ropes is a fundamentally different process in which the tubes are aligned through straightening the waviness and growth nanotube bundle size of the

spaghetti-like long ropes showing with the SEM images and carton drawings. This mechanism was in agreement with our observations in Figures 3, 11 and 12, as well as the discussions in previous stretching sections. However, considering the factors of inhomogeneity in alignment, limited laser beam size and penetration depth of Raman scattering, and layered structure of the NTN, an approach that is able to characterize the aligned fraction of the long nanotube networks in macroscopic dimensions must be further explored.<sup>18</sup>

Due to large variation and inhomogeneity of CNT networks during deformation, as shown in Figures 15 and 17, we used a data fitting process to more accurately calculate the aligned fraction (AR) of CNT oriented along the stretching direction.<sup>43,50</sup>

$$I(\phi, A_R, \sigma) = A \int_0^{2\pi} \left[ \frac{1 - A_R}{\pi} + \frac{A_R}{\sigma\sqrt{\pi/2}} e^{-2(\theta-\phi)^2/\sigma^2} \right] \cdot \frac{\cos^4\theta}{\cos\theta + K\sin\theta} d\phi \quad (7)$$

where  $A_R$  is aligned fraction and  $\sigma$  is the Gaussian standard deviation (equivalent  $\text{FWHM} = \sigma\sqrt{2\ln 2}$ ). Two Raman orthogonal measurements at  $\theta = 0$  and  $\pi/2$  provide a ratio that depends on both  $\sigma$  and  $A_R$ . If  $\sigma$  is small,  $I(0)/I(\pi/2)$  gives a zero-order estimate of  $A_R$ . Since the Raman intensity was less sensitive to out-of-plane than in-plane misalignment when the polarized measurement was done in-plane, the FWHM value was fixed at  $11.5^\circ$ , as found in the WAXS data. The best estimate of  $A_R$  was 0.93 for the 80% strain-stretched samples,<sup>50</sup> as shown in Figure 17. This is a higher degree of alignment of CNTs than any previously reported in the literature and comparable to high strength carbon fiber materials.<sup>32,66</sup> Such a high degree of alignment and transformation of CNT network, as shown in Figure 18, are essential to achieve high mechanical properties in CNT assemblages and their composites. Through those efforts, we gained a significant fundamental understanding of CNT network evolutions, detailed alignment and packing properties of the networks.

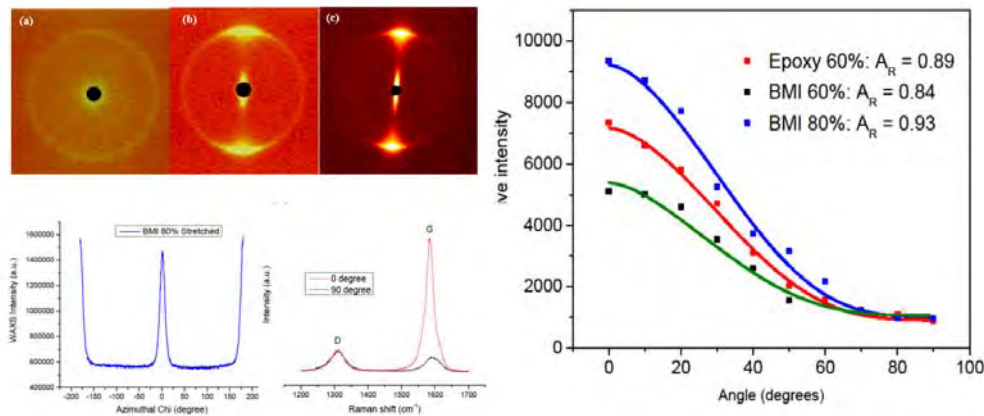


Figure 17. WAXS patterns of a randomly oriented sample (a), 40% stretched aligned sample (b), and 80% stretched sample (c), and 80%-stretched samples with BMI treatment at the (002) crystal plane  $20^\circ < 2\theta < 30^\circ$  and the close-packing peak (CP)  $5^\circ < 2\theta < 8^\circ$  as well as  $0^\circ/90^\circ$  Raman G-band ratio, and estimated aligned fraction ( $A_R$ ) values for 60% and 80% strain stretched samples

## **2. Failure Modes and Geometrically Constrained Self-assembly and Graphitic Crystal Packing of Flattened and Aligned Carbon Nanotubes**

While the mechanical properties of highly aligned carbon nanotube (CNT) thin films and their nanocomposites have been widely studied, the load transfer mechanisms and failure modes of aligned CNT materials and their composites have not been sufficiently explored and understood. In this research, super-aligned CNT thin films of 80% stretching strain with a measured alignment fraction of up to 0.93, as discussed in Section 1.8, were used. Atomic resolution transmission electron microscopy (TEM) analysis revealed unusual CNT crystal packing and permitted the observation of interesting structural features of the CNTs and their assemblages, including collapsing, flattened packing, preferred stacking, folding and twisting phenomena, as well as CNT pullouts from bundles and the resin matrix.<sup>67,68</sup> The large surface-to-surface contact areas between aligned and flattened nanotubes, driven by van der Waals interactions, gave rise to a high density packing of the flattened CNTs in the nanocomposite, resembling a graphitic material. Molecular dynamics (MD) simulations through collaboration with a NASA research team<sup>67</sup> were performed to model the packing structure and understand the dependence of density on the relative content of flattened nanotube and void space. The modeling results support the conclusions drawn from the experimental observations as well as the alignment mechanisms discussed in *Sections 1.5, 1.6 and 1.8*.

### ***2.1 TEM and SEM Experiments***

In this research, TEM images were taken using the JEM-ARM200cF (A Sub-Angström Cs Corrected Transmission/Scanning Transmission Electron Microscope from JEOL) at 80 kV to study in detail the nanostructures and CNT/CNT and CNT/resin interfaces. The TEM samples were prepared by peeling and cutting the failure areas from failed tensile specimens and placing them on TEM mesh grids. The SEM analysis was conducted using a JEOL 7401F SEM.

### ***2.2 CNT Network Transformation***

Randomly oriented CNT sheets, shown in Figures 18 (a, b), were mechanically stretched to an 80% strain to achieve a high degree of alignment. Figures 1(c, d) show the highly aligned CNTs and the substantially enlarged bundles that resulted from CNT self-assembly after the stretch processing, as discussed in *Section 1.8*. The resulting highly aligned sheets were impregnated with a BMI resin solution to make CNT/BMI nanocomposites with 5060 wt% of CNT<sup>7,15-17,67</sup> for mechanical and TEM analysis.

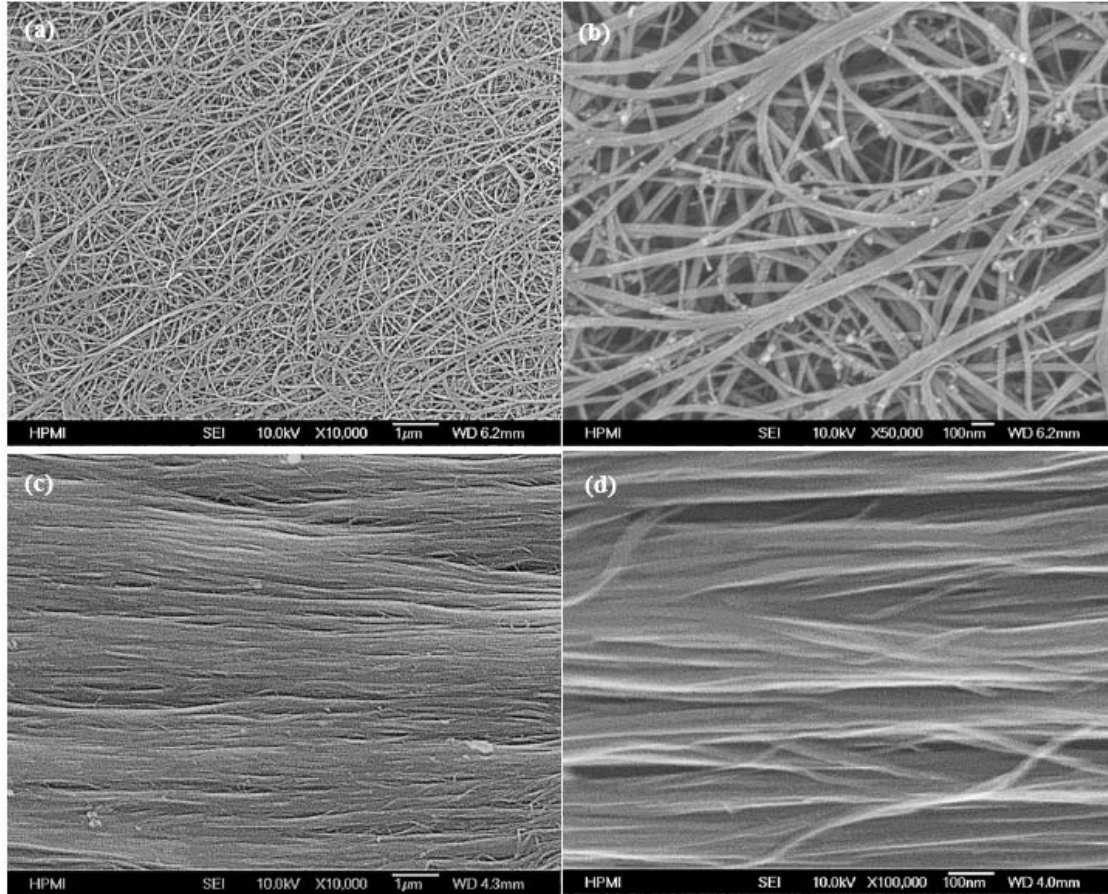


Figure 18. Surfaces of the as-received, randomly oriented CNTs with residual catalyst at  $\times 10,000$  magnification (a) and  $\times 50,000$  magnification (b), and highly-aligned 80% strain-stretched films at  $\times 10,000$  magnification (c) and  $\times 100,000$  magnification (d)

The tensile strength of the 80%-stretched aligned CNT/BMI nanocomposite specimens was  $699.47 \pm 11.68$  MPa with a Young's modulus of  $91.90 \pm 9.05$  GPa along the aligned direction. The corresponding values for a nanocomposite made with the as-received, unaligned CNT sheet were  $392.68 \pm 57.78$  MPa and  $24.02 \pm 6.16$  GPa for the tensile strength and Young's modulus, respectively. The significant improvements observed in the tensile properties of the CNT/BMI nanocomposites made with oriented CNT sheets indicate improved load transfer between the CNT assemblies in the axial direction.

### 2.3 CNT Network Failure Mode

The failure modes observed in conventional carbon fiber reinforced composites provided a useful starting point from which to understand the aligned CNT nanocomposites studied in this work. Failure of unidirectional carbon fiber ( $67 \mu\text{m}$  in diameter) reinforced composites under longitudinal tensile load occurs by three typical modes: (1) brittle fracture of fibers, (2) brittle fracture of fibers with pullout, and (3) fiber pullout with fiber-matrix debonding.<sup>69</sup> Usually no carbon fiber deformation observed after composite failure. In contrast, aligned CNT

nanocomposites frequently have telescoping failure modes and their tensile properties and failure modes are governed by complex nanotube/nanotube and nanotube/resin interactions.<sup>70</sup>

Figure 19 shows the failure surface of an aligned CNT/BMI composite. In this image, a progressive telescoping CNT pullout – beginning with a large width of the film and tapering to several small bundles of CNTs – can be seen. The morphology reveals extensive CNT pullout from the matrix, indicating a non-brittle fracture. In conventional carbon fiber reinforced composites, the load transfer between the fiber and matrix arises primarily from covalent bonding between the fiber and matrix and from friction caused by fiber surface roughness due to surface treatment and sizing.<sup>71</sup> Fiber-matrix interactions are critical in these composites since there is no noticeable direct load transfer between the carbon fibers. In contrast, the CNT pullout failure mode seen in CNT composites suggests that much weaker interfacial interactions exist between CNT bundles and the resin matrix and that direct load transfer between CNTs is playing a critical role for the failure modes. Figure 19(a) shows the layered structure that resulting from separation between layers during tensile loading and the gradual failure of large bundles. This layered failure mode indicates weak bonding and load transfer between different aligned CNT layers and is reminiscent of the delamination failure mode that occurs between plies in a conventional carbon fiber composite. Figure 19(b) shows the typical telescoping failure at the fracture surface that leads to the CNT pullout at the tips. This type of CNT pullout structure was frequently observed in this work, indicating a CNT-matrix debonding failure mode and suggesting the CNT bundles aggregate and self-assemble during the failure process.

Figure 19(c) shows the folding of CNTs and CNT bundles that results from an elastic spring-back of the nanotubes after mechanical failure of the composite. This indicates that some load transfer was occurring between the CNTs and the matrix, though clearly not enough to break the nanotubes. Figure 19(d) shows a failure mode in the aligned CNT composite, also frequently observed in unidirectional carbon fiber reinforced composites,<sup>72,73</sup> in which a crack propagates along the alignment direction and results in a separation between bundles. Again, this failure indicates inadequate load transfer between the reinforcement and resin matrix.

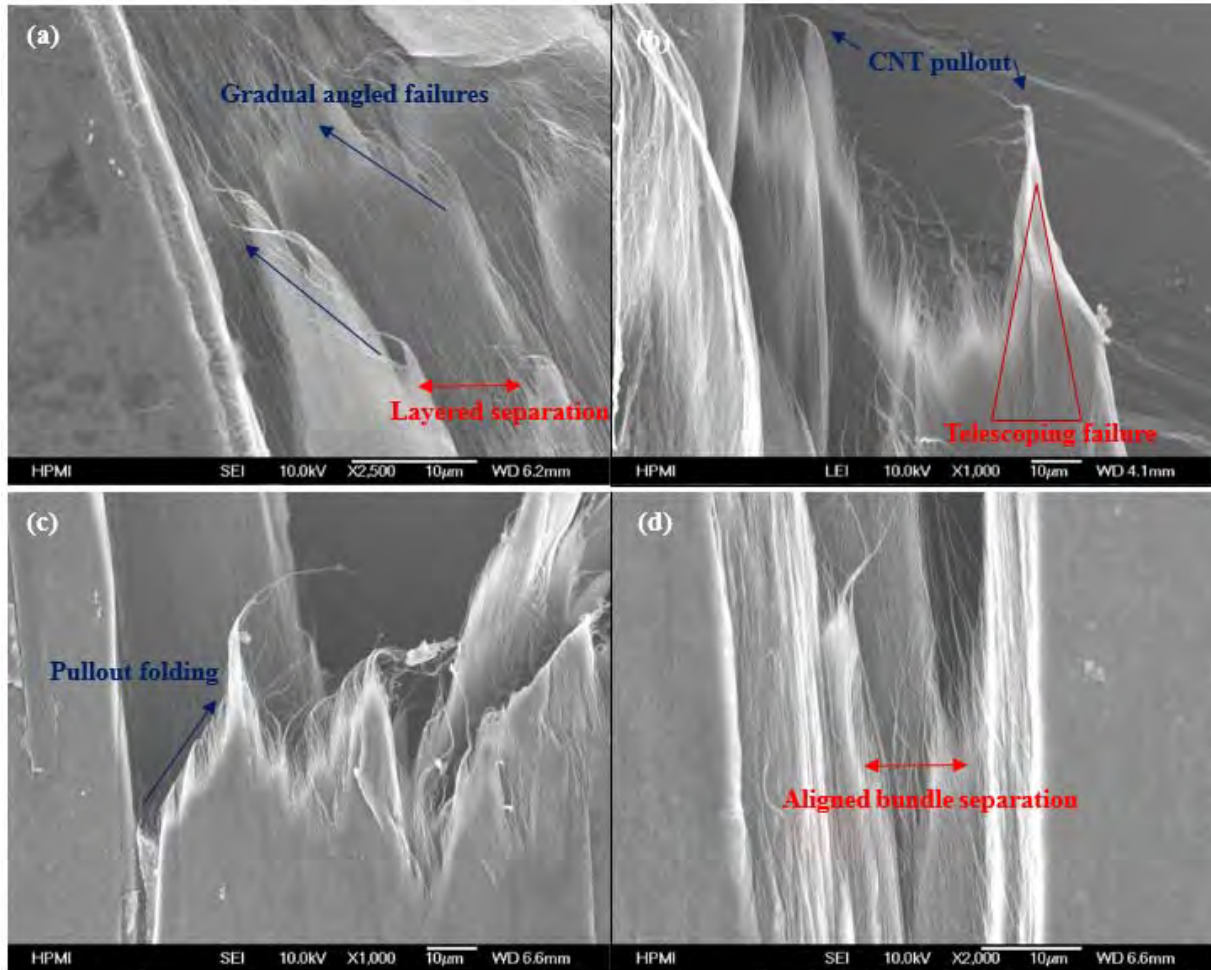


Figure 19. Major failure modes of the aligned CNT/BMI composite: (a) gradual angled failure and layered separation, (b) triangular telescoping failure and CNT pullouts, (c) CNT pullout and folding, and (d) aligned bundle separation in the perpendicular direction

#### 2.4 CNT Collapse and CNT/Resin Interface

TEM analysis was used to study the structures of individual CNTs and their bundles at the atomic scale. The TEM images in Figure 20 were taken by focusing the tips of the CNT bundles to further explore the interface and nanotube-to-nanotube interactions. Figure 20(a) shows well-aligned and broken CNT bundles that have separated into multiple small bundles. Figures 20(a, b) show that some resin remained on the surface of the collapsed CNTs after fracture, which indicates that relatively good resin/matrix impregnation and adhesion were achieved during composite fabrication. This is an encouraging result since resin impregnation of highly aligned nanotube samples is typically difficult to achieve. As the CNT density and bundle size increased with alignment, the availability and accessibility of porosity decreased, making production of well-wetted composites progressively more difficult.<sup>74,75</sup>

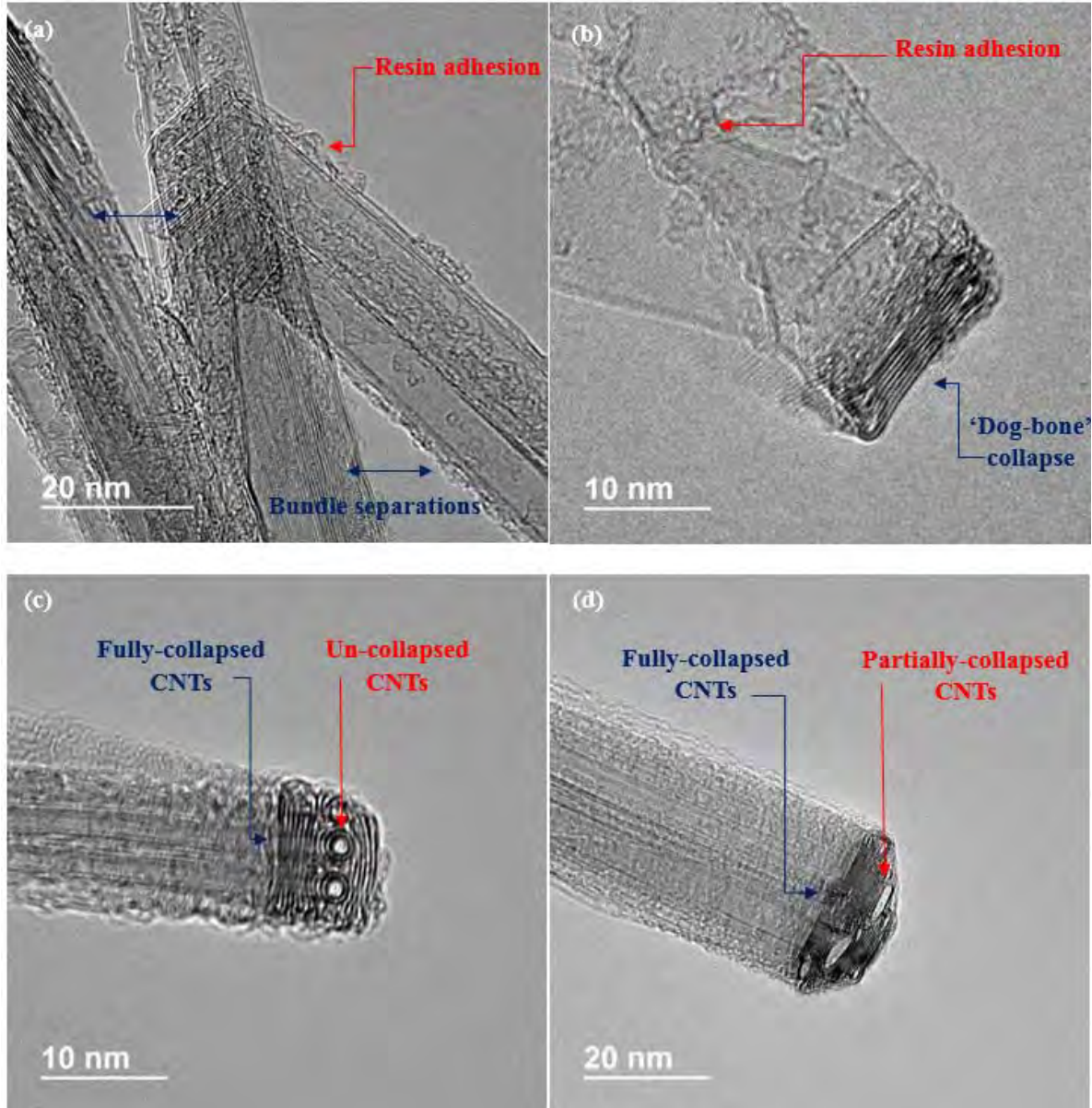


Figure 20. TEM images of (a) CNT bundle separation and resin adhesion, (b) collapsed CNT stack sliding with resin at the CNT surface, (c) diameter dependent CNT collapse, (d) varied degrees of CNT collapse in an aligned stacking

Figure 20(b) clearly shows the flattened shape taken by the CNTs that have been pulled out of the composite. This has also been referred to as a ‘dog-bone’-type collapse in the literature and linked to improved mechanical performance because of its similarity to graphitic carbon.<sup>76</sup> CNT bundle sliding is evident where multiple CNTs are seen at varied angles to the preferred axis, where they are joining as one bundle via a sliding phenomenon. Elliott and coworkers showed that single-walled CNTs with a diameter greater than 4.2 nm were unstable with respect to a flattening collapse,<sup>77</sup> though nanotubes with multiple walls would be expected to have larger critical diameters. Figure 20(c) shows that within the same stack of aligned and bundled

MWCNTs, the larger diameter nanotubes – about 10 nm in this case – fully collapsed while smaller diameter tubes remained cylindrical. Figure 20(d) shows that nanotubes of intermediate diameters partially collapsed and conformed to the fully collapsed larger diameter nanotubes. These new observations are in agreement with previous modeling results.<sup>77</sup> Since the synthesis method used to produce the nanotubes for this project tended to result in 6–10 nm diameter nanotubes, a significant majority of the nanotubes observed in the TEM images were flattened. Production methods yielding nanotubes of smaller average diameter would exhibit a larger population of cylindrical tubes.

### ***2.5 Geometrically Constrained Self-assembly and Graphitic Crystal Microstructure***

Dramatic increases in CNT alignment and volume fraction are two of the key requirements that must be met before the goal of taking optimal advantage of CNT mechanical properties in a nanocomposite material can be achieved. Considering this, it is difficult to overstate the significance of the graphitic crystal packing microstructures shown in Figure 20, and in previous work by others.<sup>78</sup> Developing an understanding of and an ability to control the size and morphology of these bundles of flattened and aligned CNTs would represent an important step towards the goal of tailorable nanocomposite materials. Some important work in this direction has already been done with analytical modeling and molecular simulation;<sup>79</sup> however, experimental imaging is also of critical importance. Thus, additional TEM image analysis, as shown in Figure 21, was conducted to further investigate this phenomena.

Figures 21(a, b) show several relatively large domains of approximately 20 flattened ‘dog-bone’ CNTs stacked into a graphite-like structure. The bundles were aligned in the stretching direction of the CNT paper used to make the composite. A visible coating of BMI polymer on the external surfaces of, and in some cases between, the stacked bundles was observed. Also notable in these images is the consistency in nanotube diameters within each stack, which is shown in Figure 21(c), where a transition from a stack of large diameter nanotubes (blue outline) to a stack of medium diameter nanotubes (red outline), rather than an intermixing of the two sizes, can be seen. Segregating the nanotubes by size in this manner had the effect of maximizing the interfacial adhesion between the nanotubes while minimizing defects in the packing arrangement. In a continuous range of nanotube diameters, rather than the bimodal distribution shown in Figure 21(c), the CNTs tended to be found in order of decreasing size, as shown in Figure 21(d). Again, this arrangement, referred to as pyramidal stacking, maximizes the attractive overlap between adjacent nanotubes while minimizing internal voids within the stack.

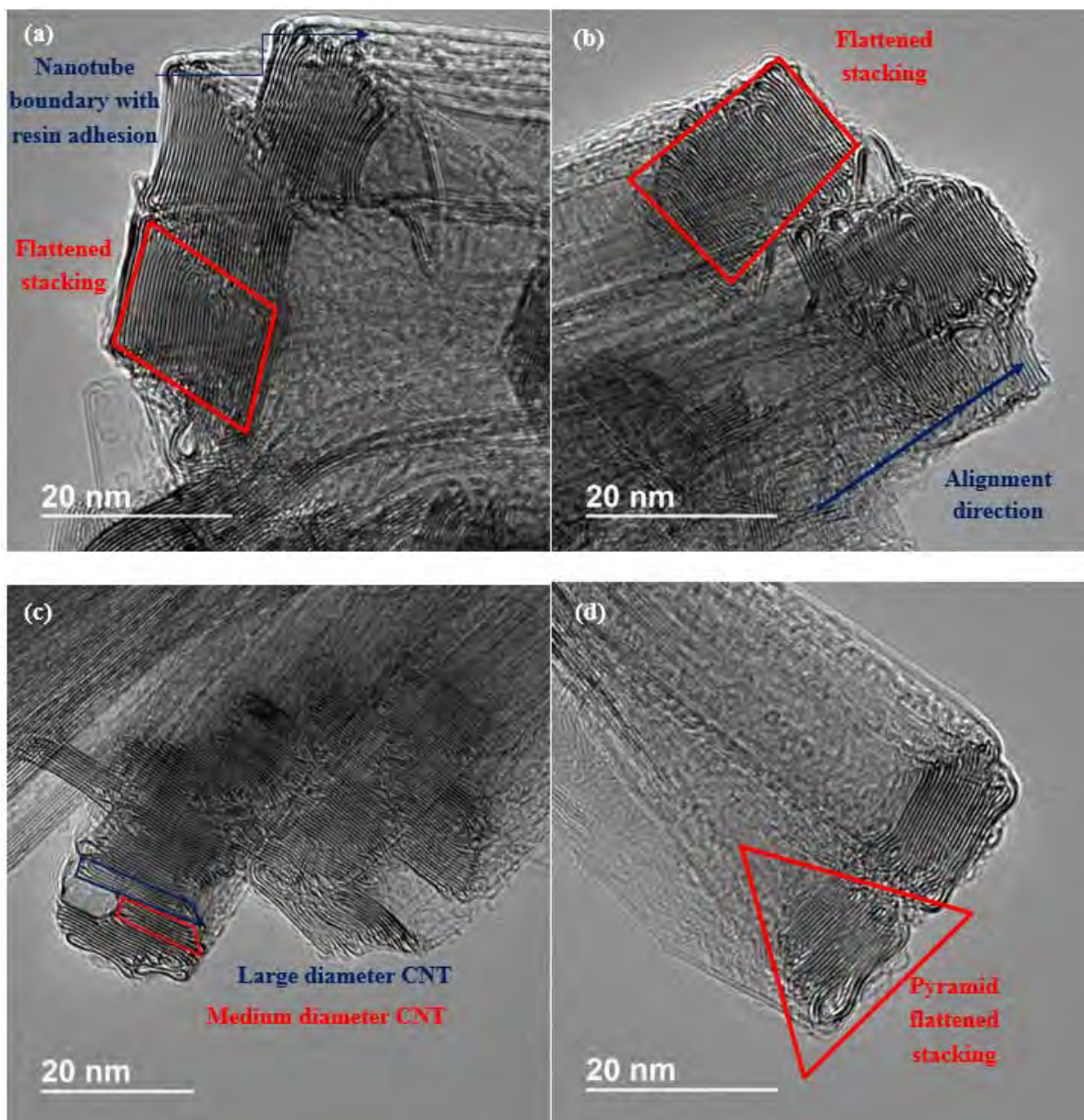


Figure 21. TEM images of (a) CNT flattened stacking and visible nanotube boundary with resin interface, (b) large bundled flattened ‘dog-bone’ stacking due to geometric constrains and corresponding alignment direction, (c) varied diameter stacking, (d) pyramid type flattened stacking for gradually varied diameter CNTs

This preferential association of similarly sized CNTs constitutes the geometrically constrained self-assembly and packing features has not been explored or understood. This phenomenon initiates that during the gas phase synthesis process when the nanotubes have the greatest mobility, they contact and pair with other nanotubes of similar size. The alignment, bundle size growth and final stacking configuration must then come during the sheet stretching process, which is the only other time when large scale geometric changes occur within the as-prepared CNT material. In any case, the overall thermodynamic driving force appears to be the energetic

favorability of maximizing of the attractive van der Waals interaction by maximizing the area of overlap between adjacent nanotubes. This is a different behavior than is found in other materials containing ordered flakes or sheets.<sup>80</sup> In nacre, for example, the arrangement of the much larger filler particles is significantly influenced by the polymer layers separating the platelets. Nanoclays, while of similar thickness to the CNTs studied here, tend to be charged and, therefore, more heavily influenced by electrostatic interactions. As shown in Figure 22, this new discovery of geometrically constrained self-assembly and graphitic crystal microstructure of aligned and flattened CNTs provides the essential alignment and molecular improvements to potentially realize theoretical performance of nanotube materials. We also demonstrated a simple mechanical stretching process capable of cost effective scale-up to potentially accelerate the rapid insertion of the materials into real world applications.

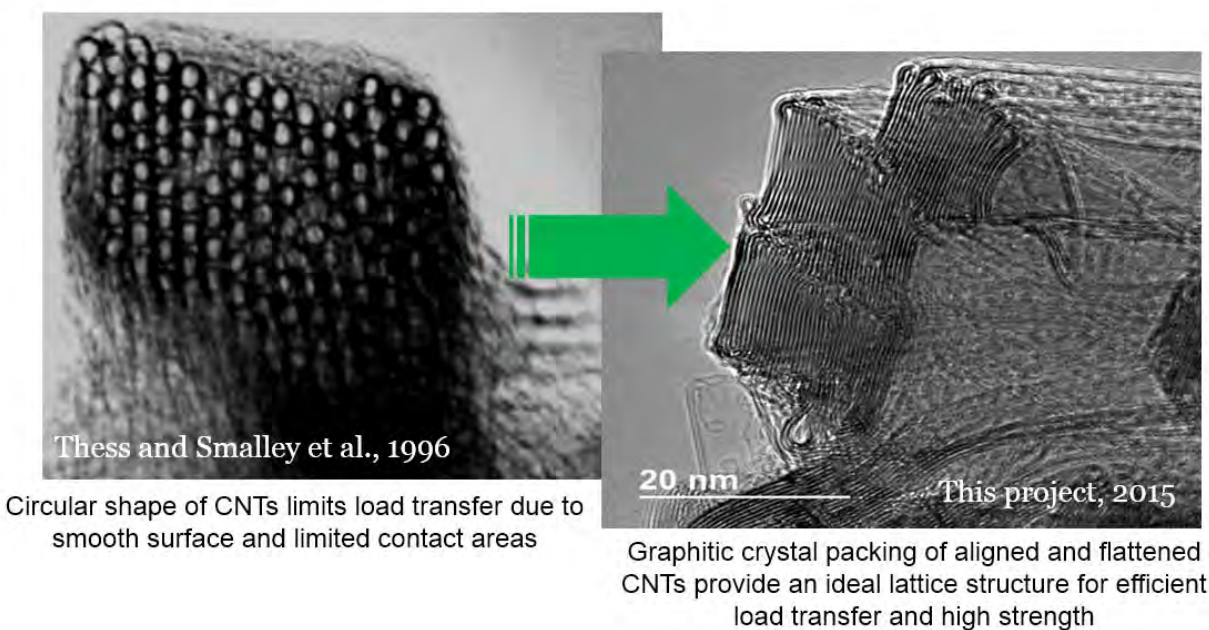


Figure 22. New super-molecular structures of CNT assemblages: geometrically constrained self-assembly and graphitic crystal for load transfer breakthrough

### ***2.6 Molecular Model and MD Simulation of Packing Models of Geometrically Constrained Self-assembly and Graphitic Flattened CNTs***

Thorough collaboration, the NASA research team<sup>67</sup> successfully developed and conducted MD simulations to validate the stability and theoretical density of this new microstructures of CNT assemblages. The open source program LAMMPS was used to perform the MD simulations, and the open source program Ovito was used to provide images.<sup>81,82</sup> The quantum mechanics based force field for carbon (QMFF-Cx) of Pascal et al. was used to determine interatomic forces.<sup>83</sup> Both the round and flat model simulations used DWCNTs composed of a (93,0) CNT nested inside of a (102,0) CNT. In isolation, these DWCNTs were found to have an outer diameter of 8 nm and an inter-wall spacing of approximately 0.34 nm, which was within the range of nanotube

diameters observed in the experimental TEM images shown in Figures 20 and 21. The round CNT simulation used a 4x4 array of DWCNTs in a periodic cell with dimensions of 31.7×27.5×5.1 nm<sup>3</sup>. The flattened CNT simulation cell contained a 2×6 array with dimensions of 23.1×10.2×5.1 nm<sup>3</sup>. In both cases, the CNTs were 5.1 nm long in the axial direction, resulting in simulation cells containing 149,760 and 112,320 atoms for the round and flattened cases, respectively. The large number of atoms in these systems and the slow inter-tube relaxation processes required extensive equilibration runs of approximately 1.5 ns each.

The equilibrium structures of the round and flattened systems found at a simulation temperature of 300 K are shown in Figure 23, and their densities are provided in Table 3. Note that both images are shown at the same scale and accurately reflect the dramatic decrease in volume and corresponding increase in density that occurs upon flattening. Figure 23 shows that the flat CNTs stacked vertically to form a structure similar to graphite. The round CNT system are flattened on the edges to form a hexagonal shape with four-layer graphite-like walls. This is a well-known structural deformation known as polygonization, which balances the attractive van der Waals interactions with the increased strain energy that results from nanotube deformation.<sup>84,85</sup> The two systems simulated were composed of 0% collapsed CNTs and 100% collapsed CNTs, establishing minimum and maximum packing densities for 8 nm diameter nanotubes. For larger diameter CNTs, the density will decrease for round CNTs and increase for flattened CNTs. In the limit of very large diameter CNTs, the density of flattened nanotubes will approach that of graphite because the contribution of the end-loops is independent of the CNT diameter. For smaller diameter CNTs, the density will increase for round CNTs and decrease for flattened nanotubes as the contribution of the end-loops become more significant. Below a critical diameter, predicted to be around 5 nm for DWCNTs,<sup>86,87</sup> the flattened CNT geometry will no longer be energetically stable and only round CNTs will be present. As seen in Figure 23(d), partially collapsed CNTs are also found in these materials and will have densities intermediate between those of the 0% collapsed and 100% collapsed systems.

Table 3. Densities of round and flat CNT models

System	Density (g/cm <sup>3</sup> )
Round CNTs	0.665
Flattened CNTs	1.820

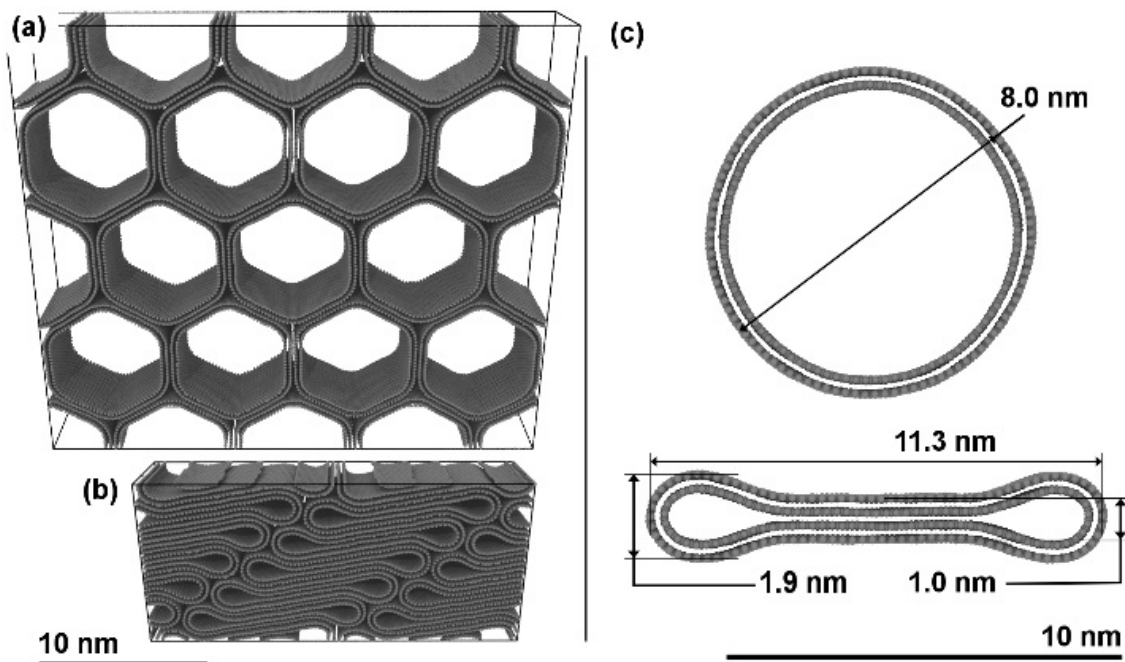


Figure 23. Bulk CNT systems consisting of (a) 0% collapsed round CNTs and (b) 100% collapsed CNTs, (c) dimensions of flat and round CNTs in isolation

Using the measured densities of neat CNT film in Table 4 and the calculated CNT densities and from Table 1, the void volume fraction may be computed for varying ratios of round to flattened CNT materials. Figures 22 and 23 show that stretching the samples decreased the void volume fraction and increased the fraction of flattened nanotubes. In fact, to achieve the total density observed in the 80% stretched sample ( $1.61 \text{ g/cm}^3$ ), the volume fraction of flattened CNTs must be above 0.8 if the sample is assumed to be fully dense packing, i.e. with a void volume fraction of zero. Making the more reasonable assumption that some void volume remains in the samples, the fraction of flattened nanotubes must be even higher. If a void-free sample could somehow be prepared at the unstretched density ( $0.76 \text{ g/cm}^3$ ), this model predicts that it would have to contain approximately 10% flattened nanotubes. The unstretched or initial random samples clearly contained a significant void content, as shown in Figure 18, indicating the as-received material must contain a content of flattened nanotubes much higher than 10%. This is an interesting result relevant to the question of whether the nanotubes were flattened during synthesis or during the stretching process. These results indicate that a significant portion of the flattening occurred during synthesis. The high density of flattened and crystal packed CNT structures was close to that of reinforcement carbon fiber ( $1.78 \text{ g/cm}^3$ ), as shown in Figure 24, indicating improved microstructures to provide large molecular level voids in the materials.

Table 4. Measured densities of treated and purified CNT film and CNT/BMI composites

Stretching Strain (%)	Measured Density (g/cm <sup>3</sup> )		Areal Density (g/m <sup>2</sup> )		Average Thickness (μm)	
	CNT Tape	CNT/BMI composite	CNT Tape	CNT/BMI composite	CNT Tape	CNT/BMI composite
	0	0.76	1.49	12.24	19.92	16.10
20	1.22	-	26.64	-	21.84	-
40	1.42	1.64	31.81	29.54	22.40	18.00
60	1.54	1.74	40.85	37.53	26.50	21.57
80	1.61	1.81	50.57	46.13	31.34	25.50

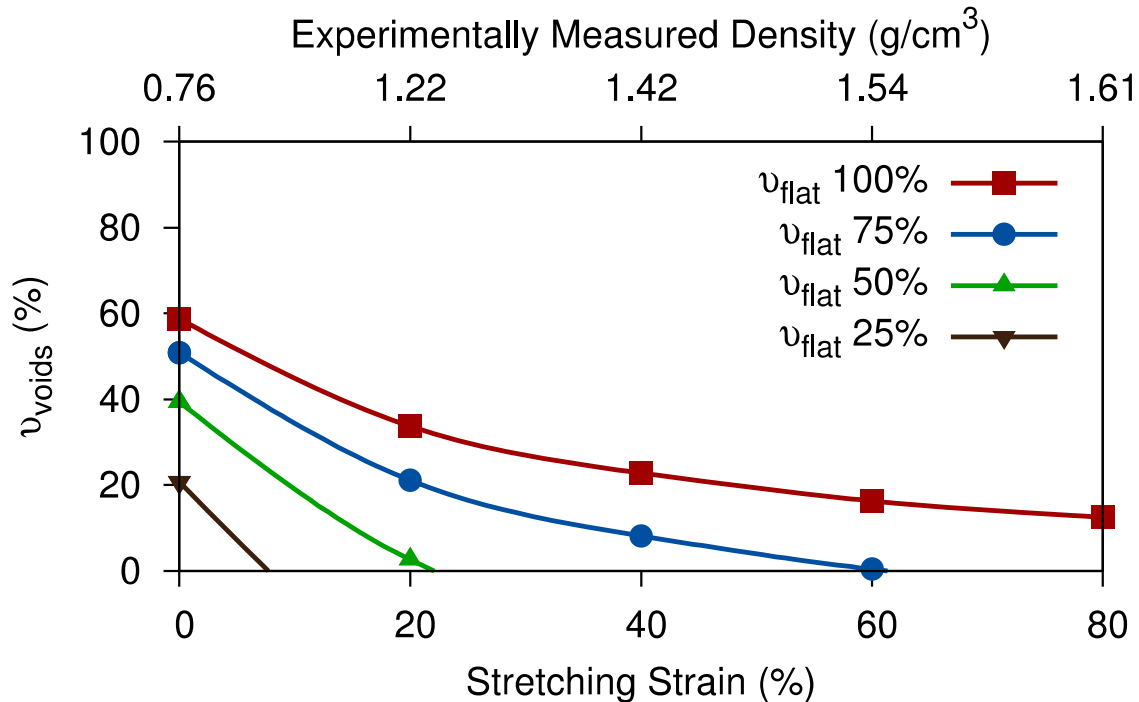


Figure 24. Volume fraction of voids at various stretching strains. Corresponding experimental densities of neat CNT film samples are shown on the top axis, data from Table 4. Lines correspond to assumed volume fractions of flattened CNTs in the samples

In the case of CNT/BMI nanocomposite samples, very high measured densities were observed, as shown in Table 4. If the system is assumed to be composed of 100% flat CNTs and to be fully

dense (0% void volume), a maximum density of 1.56 g/cm<sup>3</sup> is predicted. Increasing the assumed density to that of graphite (2.26 g/cm<sup>3</sup>), a maximum composite density of 1.71 g/cm<sup>3</sup> was found. The CNT/BMI composites were found to have experimental densities of 1.74 and 1.81 g/cm<sup>3</sup> in the 60% and 80% stretched case, respectively. This is possibly due to the high temperature and pressure processing conditions inducing further assembly and packing of the CNTs during composite fabrication.

### ***2.7 Twisting and Folding of Flattened CNTs***

In addition to the nanotube collapse and packing phenomena discussed and analyzed above, a number of other interesting structural deformations were observed during the course of this work. For example, Figures 25(a, b) show a collapsed CNT in a twisted ribbon configuration. Isolated flattened CNTs are easily deformed in this manner because of the significant reduction in cross-sectional area relative to a cylindrical CNT and the absence of lateral support that would be found in a bundle. In fact, previous atomistic simulations of the stability of single- and multi-walled CNTs showed that lattice registry effects can cause the warping and twisting that occurs as the nanotubes collapse due to attractive van der Waals interactions.<sup>87</sup> This mode of deformation has attracted interest since the early days of CNT research.<sup>88</sup>

There is also a longstanding interest in the mechanical behavior of CNTs under compression. For example, a combination of experimental data and modeling was used to study the buckling CNTs under compression. MWCNTs were found to have a compressive strength more than double that of any known fiber, and applying high compressive stresses resulted in kinks with large degrees of bending.<sup>89</sup> Other studies of the kinking phenomena in MWCNTs showed that the applied stress was distributed among the multiple walls of the CNT. This load distribution mechanism should translate to bundles of flattened CNTs and could be enhanced due to their larger contact areas and improved load transfer.<sup>90</sup> While compressive loading was not directly studied during this project, the spring back process, which occurs when the tension is released from a bundle of nanotubes when pulled from the matrix during fracture, applies a large transient compressive load to the nanotubes. Figures 25(c, d) show the stress-deformation couplings where the CNTs bundled together as fibrils were deformed and folded at the tips of many of the telescoping triangular failures<sup>91</sup>. In Figures 25(d), the reference alignment direction is shown to illustrate that the bundled CNTs folded away from the composite when the fibrils separated and the off-axis stresses occurred. The fact that the CNTs remain bundled even after the high stress bending event is an indication of the robustness of the adhesion between flattened CNTs in the bundles.

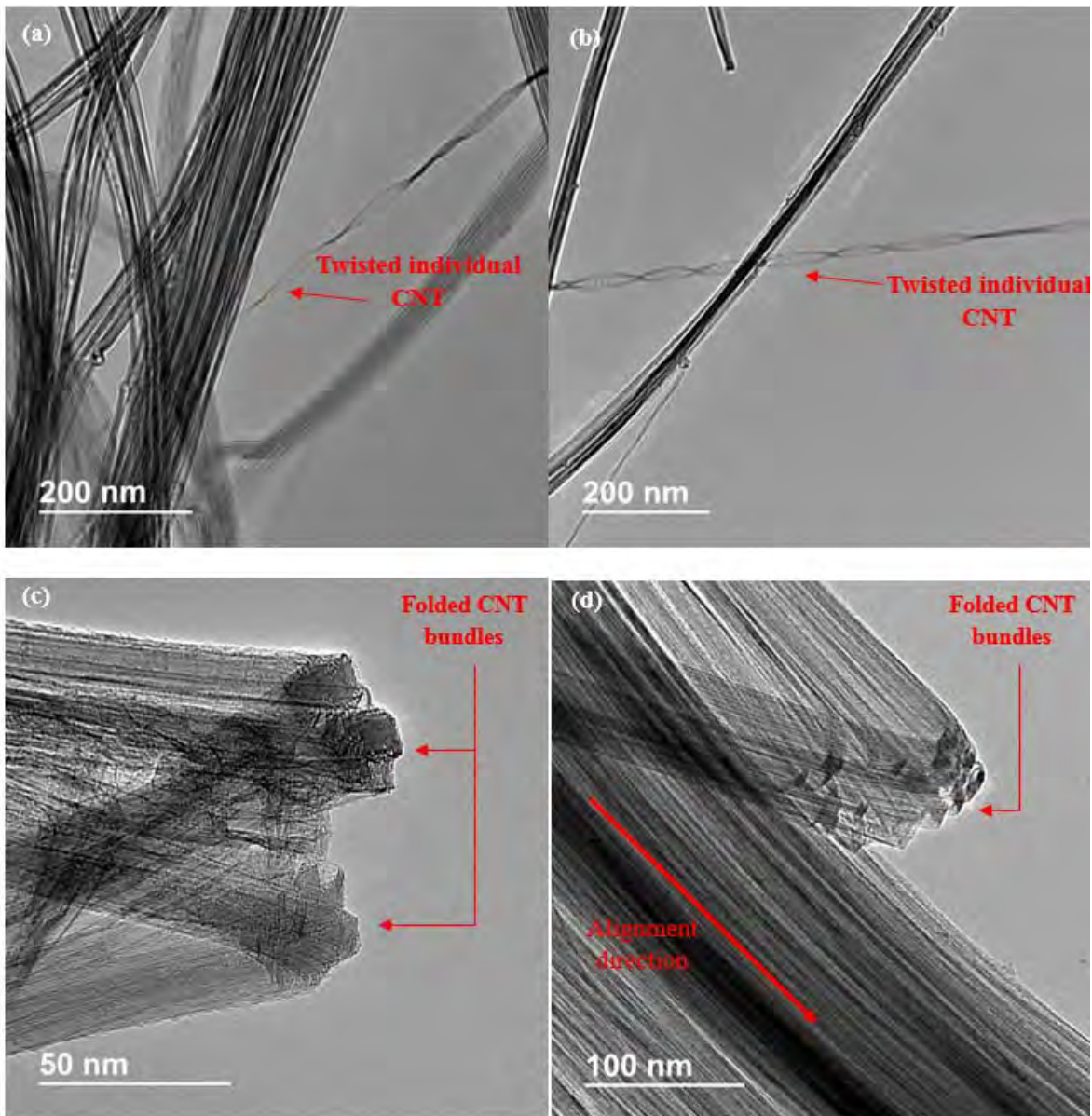


Figure 25. TEM images of (a, b) twisted individual CNTs (c) folded CNTs from the pulled-out bundles, and (d) bundles of folded nanotubes fractured away from the alignment direction

### 2.8 CNT Pullout Failure and CNT/resin Interface Bonding

While the CNT/BMI composite tested in this work failed, in a macroscopic sense in a brittle or delamination dominated manner, the TEM and SEM images revealed a very different fracture surface than typically found for conventional carbon fiber composites. The major failure mode was the pull out of individual bundles when the interfacial bonds were broken by shear stresses between the nanotubes and the resin matrix. Also note that this did not appear to occur as a single catastrophic event, but rather in a progressive, bundle-by-bundle manner until ultimate failure of the nanocomposite occurred.<sup>41,72-74</sup> Figure 26 shows the various types of pullout failure observed. Figure 26(a) shows several flattened stacks of varying lengths after pullout. Figure

26(b) provides a closer view of a single bundle pullout and highlights the resin remaining on the bundle surface.<sup>72-74</sup> Figure 26(c) shows that a long bundle can dramatically telescope from a large diameter bundle composed of many CNTs to a single CNT. Figure 26(d) shows an intra-bundle sliding between CNTs, where a bundle between a graphitic and amorphous region slides along the alignment direction while staying in the flattened bundle's plane. The region labeled as the graphitic region was a bundle of aligned and collapsed nanotubes with its basal plane vertical to the sliding CNT bundles. However, the amorphous region demonstrated a mixture of amorphous resin and much smaller CNT bundles. Taken together, these results indicate that both CNT/CNT and CNT/resin bonding are critical to the mechanical performance of the nanocomposite, and they must be enhanced to further improve the mechanical properties.

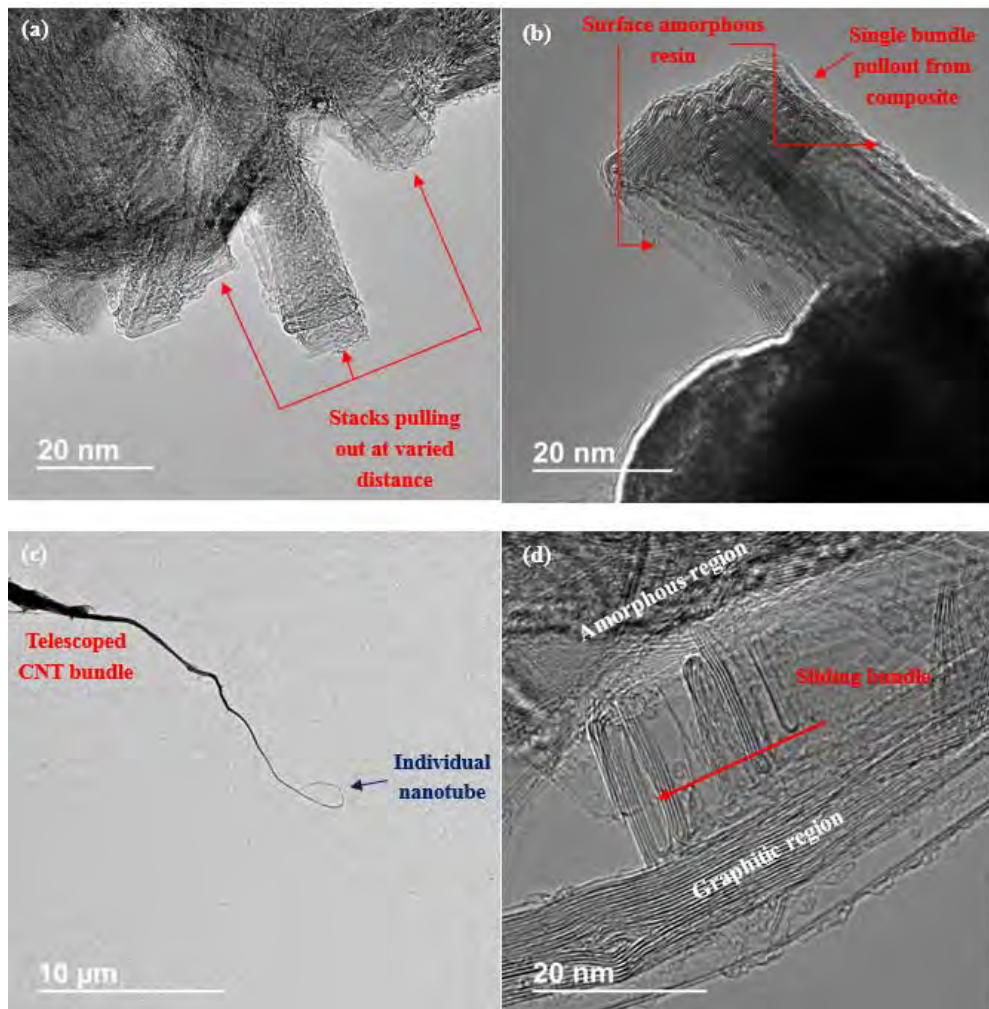


Figure 26. TEM images of (a) flattened CNT stacking with pullout of each stack, (b) uniform stacking layered pullout, (c) telescoping bundle pullout, (d) one flattened CNT stack sliding and pulling out

### 3. High Energy Beam and High Temperature Treatments of CNT Networks

We investigated the crosslinks of CNT assemblies to enhance inter-nanotube interactions to improve load transfer for high mechanical performance. In this research, we utilized electron beams (E-beam) set at different energy levels to treat CNT sheets or buckypapers, and explored structure and property changes of the resultant materials. The high-temperature treatment (>carbonization temperature) of CNT networks were conducted to observe thermal effects.

Observations of irradiation-induced phenomena have generated great interest in the effects of irradiation on CNTs, such as the coalescence and welding of CNTs, tunneling barrier formation among CNTs and creating inter-tube bridging or crosslinks within nanotube ropes<sup>92-99</sup> and buckypaper.<sup>99-103</sup> Beams of energetic particles are believed to be effective for providing scale-up potential for nanotube crosslinks and functionalization. For CNTs, the collision of an energetic particle with a carbon atom will result in several types of point defects. For instance, the formation of a single-vacancy or multi-vacancies will occur and a number of primary knock-on atoms, which, if their energy is sufficient, will leave or displace other atoms in the nanotubes or will be adsorbed onto the nanotube walls if their energy is low or create crosslinks of CNTs. Some experimental studies using a tunneling electronic microscopy and SEM on the in-situ irradiation of single-walled carbon nanotubes (SWCNTs) ropes validated the substantial enhancement of mechanical properties of an individual nanotube rope, due to inter-tube covalent bonding formation.<sup>97-99</sup> We also demonstrated crosslinking of SWCNTs in loosely and randomly packed macroscopic buckypaper, which was achieved by in-situ cross-linking SWCNTs under electron beam irradiation.<sup>103</sup> In this research, we focused on studying of E-beam treatment on macroscopic CNT sheet samples and investing the mechanical and electrical property changes of the resultant materials.

We used three different approaches to irradiate e-beams to the CNT networks: 1) high-energy beams (2MeV) in the NeoBeam alliance with a water cooled stage in an open air condition, 2) low energy beams (9 keV) with a high vacuum, and 3) mid-range powered energy E-beams (60 keV) with slight vacuum. Coalition of SWCNT can occur at over 1300 °C based on MD simulations.<sup>104</sup> The energy must break the CC bonding and connect with other adjacent C atoms. The E-beam accelerated the CC bonding break due to its energy level, so we used different e-beams for this purpose.

### 3.1 High Energy E-beam Irradiation

We previously reported that e-beam treatment increases the mechanical properties of CNT networks.<sup>103</sup> The treatment also created defects on the surface of the CNTs and increased the electrical resistivity. As shown in Figure 27, the CNT walls were damaged by the high energy E-beam treatments.

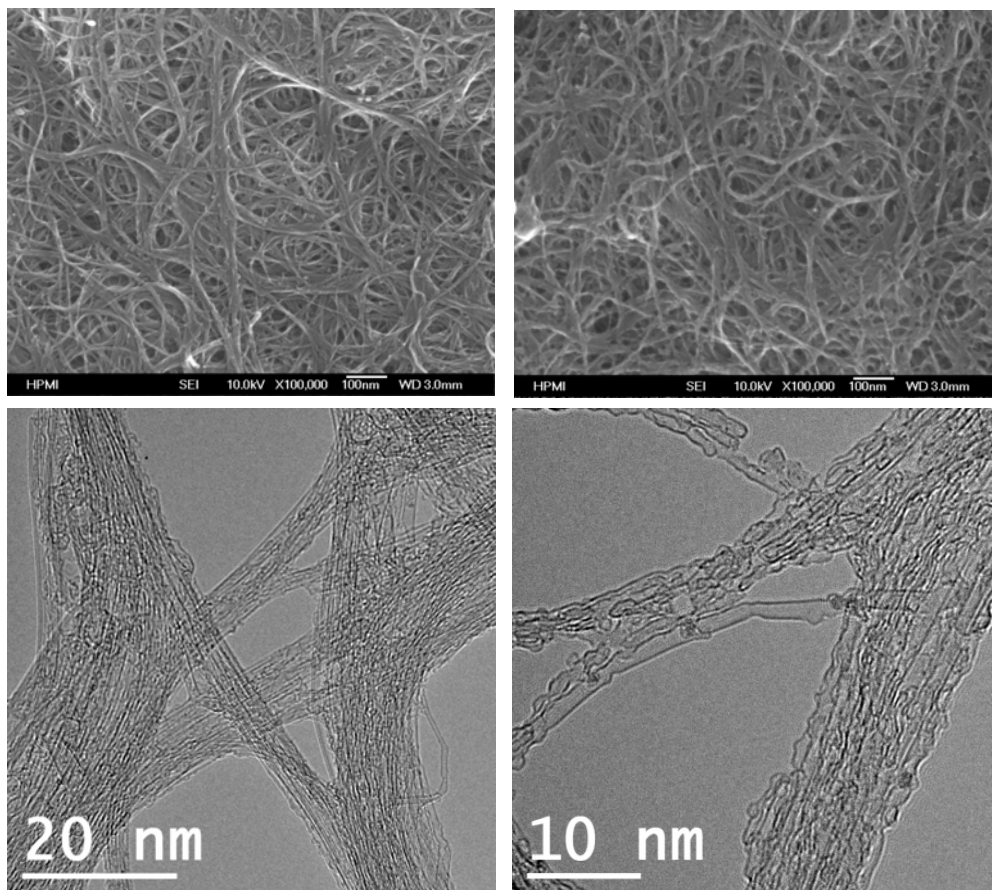


Figure 27. SEM and TEM images of (left) pristine SWCNT and (right) e-beam irradiated CNT with dose of  $300 \times 10^{15} \text{ e/cm}^2$

Figure 28 shows the Raman spectra and temperature dependence of resistivity of the SWCNT films. E-beam irradiated CNTs showed a larger disorder induced D-band as the electron dose increased. The treated samples also illustrated significant temperature dependence of resistance compared to pristine CNTs, which are typical signs of a disorder increase.

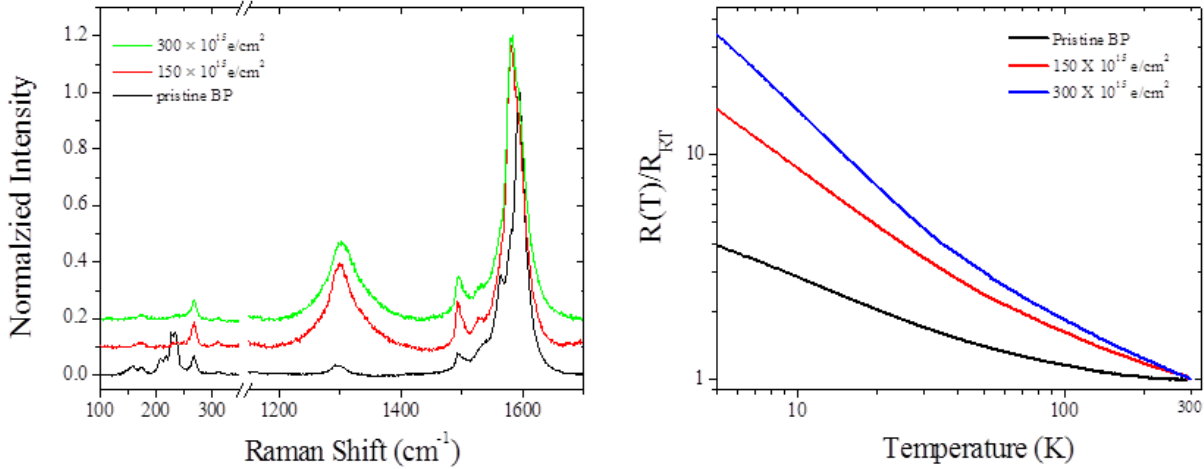


Figure 28. Raman spectra (785 nm laser excitation) at different electron doses and their corresponding temperature dependence of resistance

Figure 29 shows the electron energy loss spectroscopy (EELS) of a pristine CNT network and an irradiated one. EELS of graphene are also shown for reference. The EELS results of the pristine CNT and graphene appear almost identical; however, E-beam irradiated CNTs show broader peaks compared to the pristine sample. E-beam irradiated CNTs have broad  $\sigma^*$  peak of  $\sim 300$  eV and the similar spectrum can be found in the bended SWCNTs.<sup>105</sup> This indicates a change in the electronic state of the sample. Therefore, E-beam irradiated disorder and defects lead to changes in electronic state and the change of temperature dependent electrical transport property.

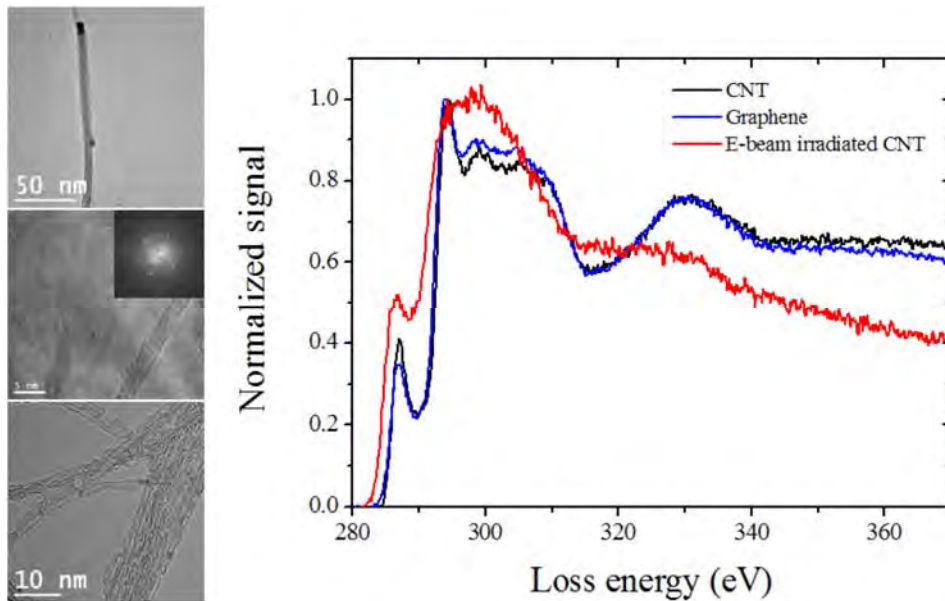


Figure 29. Carbon K-edge EELS of different Carbon structures normalized to maximum  $\sigma^*$  peak. E-beam irradiation makes  $\sigma^*$  peak and  $\tau^*$  peak broadened

### ***3.2 Low Energy E-beam with High Temperature and High Vacuum***

We used a regular E-beam evaporator (9 keV) for the E-beam treatment of CNTs. The SWCNT sheet was kept under a high vacuum ( $10^{-7}$  Torr). As the E-beam current hit the sample surface, the temperature increased. Figure 30 shows TEM images from different locations of the treated samples. The MWCNTs were observed in the intense beam areas, and welding of CNT walls was observed. The SWCNTs with slightly damaged walls were observed outside of intense beam area. However, this method cannot be applied for scalable production and treatment due to the facility limitations.

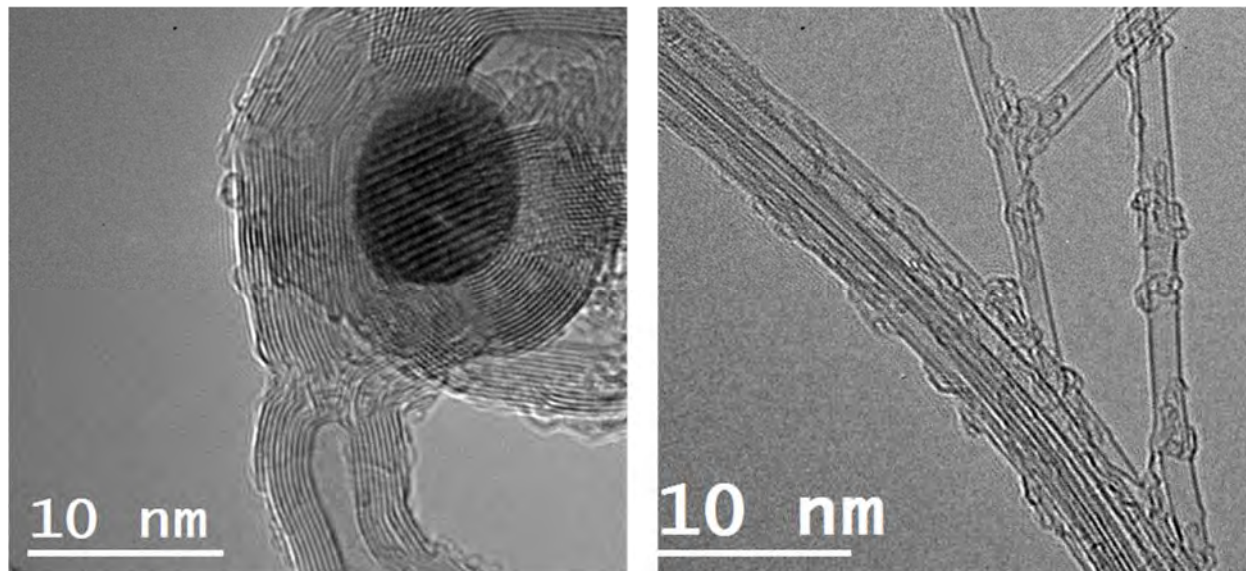


Figure 30. TEM images of E-beam irradiated SWCNT with the low energy E-beam under high vacuum

### ***3.3 Mid-Range E-beam Energy with Vacuum***

We used the E-beam manufacturing facility at the North Carolina State University, which operates at 60 keV with a vacuum level of  $10^{-3}$  Torr for CNT treatment. The CNT sheet sample size was about 6×6 inches. Figure 31 shows a photo of the sample after e-beam irradiation of 2 mA current and SEM images of the front and back surfaces of the MWCNT sheet, which shows the CNTs were exposed to high temperatures and strong beam energy. The backside color was quite different due to the deposition of materials from the graphite substrates.

Figure 31 shows some residual amorphous carbon remained on the surface and repeated exposure decreased these amorphous carbon deposition. The tensile modulus increased from less than 1 GPa in the pristine sheet to 35 GPa after irradiation, as shown in Figure 32. However, the mechanical strength was noticeably reduced due to possible CNT damages. After the E-beam treatment, the strain reduced from 25% to 12% range, indicating the combination effect of nanotube damage and amorphous deposition to limit CNT movements in the network. The effects of E-beam treatment on CNTs and their networks are complicated, so more fundamental studies are needed to gain better understanding.

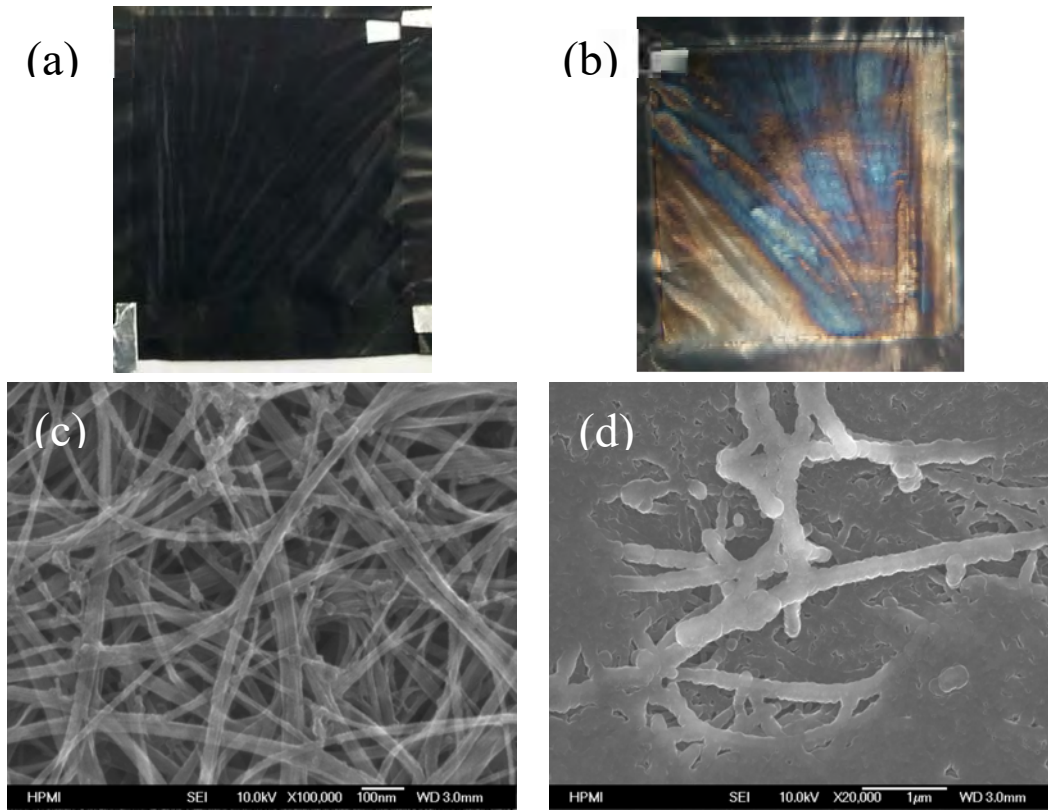


Figure 31. E-beam treatment of MWCNTs: (a) Front and (b) backside pictures of MWCNT sheet after the E-beam irradiation; (c) and (d) are their corresponding SEM images

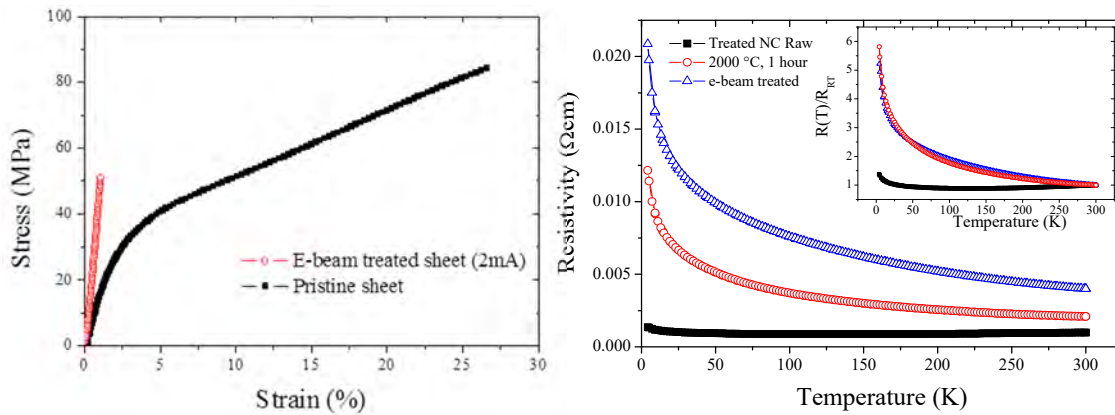


Figure 32. Typical tensile properties of pristine MWCNT sheet and e-beam irradiated sheet; the sheet modulus increased but strength was decreased after E-beam treatment; temperature dependence of resistivity of the pristine MWCNT sheet and CNT Sheet from (random sheet from Nanocomp), thermally treated sheet at 2000°C and 60 keV e-beam treated sheet. Inset shows normalized resistivity at room temperature

#### 4. CNT Buckypaper/Carbon Fiber Hybrid Composites

We studied the manufacturing process, microstructures and CNT sheets (buckypaper or BP) /CF interply hybrid composites to develop an effective approach to directly incorporate high-performance CNT materials into carbon fiber structural composites for improving mechanical and electrical conductivity.<sup>73</sup> Through collaborating with Boeing and the Cyttec research teams, we used random CNT sheets with unidirectional IM7/BMI prepreg from Cyttec and an autoclave process to make aerospace quality composite samples.

Incorporating CNTs into CF structural composites is considered a promising approach.<sup>12,13,106-113</sup> CNTs have been applied in composite materials as filler materials in resin matrices or by direct growth on fiber surfaces to improve structural, electrical and thermal properties. However, homogeneous dispersion of CNTs and fabrication of quality composites with high CNT and carbon fiber (CF) contents in large-scale structures remain major technological challenges.<sup>113,114</sup> Some innovative approaches have been attempted to fabricate CNT/fiber hybrid multiscale composite materials. For example, Wardle and co-researchers<sup>111,112</sup> succeeded in developing a transfer-printing scheme to place vertically-aligned CNT forests between two plies of fiber prepregs. The resulting hybrid composite contained an interlaminar architecture of aligned CNTs, leading to enhanced toughness of the composite.

As shown in Figure 33, we directly incorporated buckypaper with CF prepreg to make aerospace-quality composites (about 5560 vol% CF and 38 wt.% CNT contents). Large (200×250 mm<sup>2</sup>) BP/CF interply hybrid composite samples were developed to transfer the multifunctional attributes of CNTs into the materials while maintaining the structural performance of aerospace composites. During autoclave processing, the through-thickness resin flow and impregnation from fiber prepreg under vacuum and autoclave pressure dried or impregnated the buckypaper (buckypaper prepreg), followed by the in-plane resin bleeding mainly along the laminate sides after resin saturation of the buckypaper.<sup>73</sup> The extremely low permeability ( $10^{-16-17} \text{ m}^2$ )<sup>107</sup> of buckypaper layers eliminated the resin bleeding along the through-thickness of the hybrids. The higher CNT content caused voids and resin starvation defects in the BP/CF hybrid composites were due to the low permeability and high absorbency of dry buckypaper. Buckypaper prepreg lay-up processing is especially suitable to hybrid composite fabrication with a high global CNT concentration and produces less voids and defects.<sup>73</sup> Buckypaper layers showed consistent thicknesses in all prepared hybrid composites, which were about double the thickness of the dry pristine buckypaper due to absorbency and swelling effects. The buckypaper/unidirectional carbon fiber hybrid composites with 4.95 wt% CNTs showed promising tensile strength and modulus of 2519±101 MPa and 149±18 GPa, close to the corresponding values of the control sample. The tensile properties decreased with the increase of CNTs or buckypaper contents, but the electrical conductivity exhibited significant improvements. With additional functionalization of CNT to enhance interfacial bonding, the resultant hybrid composites showed an increase in tensile properties, and the sample failure modes changed from explosive failure modes of the control samples to more step-wise

delamination failure. SEM analysis showed the buckypaper layer acted as micro-crack arresting barriers to avoid through-thickness crack propagation and increased the failure strain and properties, as shown in Figure 34. By studying and modeling resin flow with low permeability CNT layers, using much stronger sheets of aligned CNTs, and applying functionalization to improve interfacial bonding, we can potentially develop a scalable manufacturing approach to make high quality CNT BP/CF hybrid composites for multifunctional and high damage tolerance structure applications. More importantly, this method is able to scale-up and realize fast insertion into current composite applications.

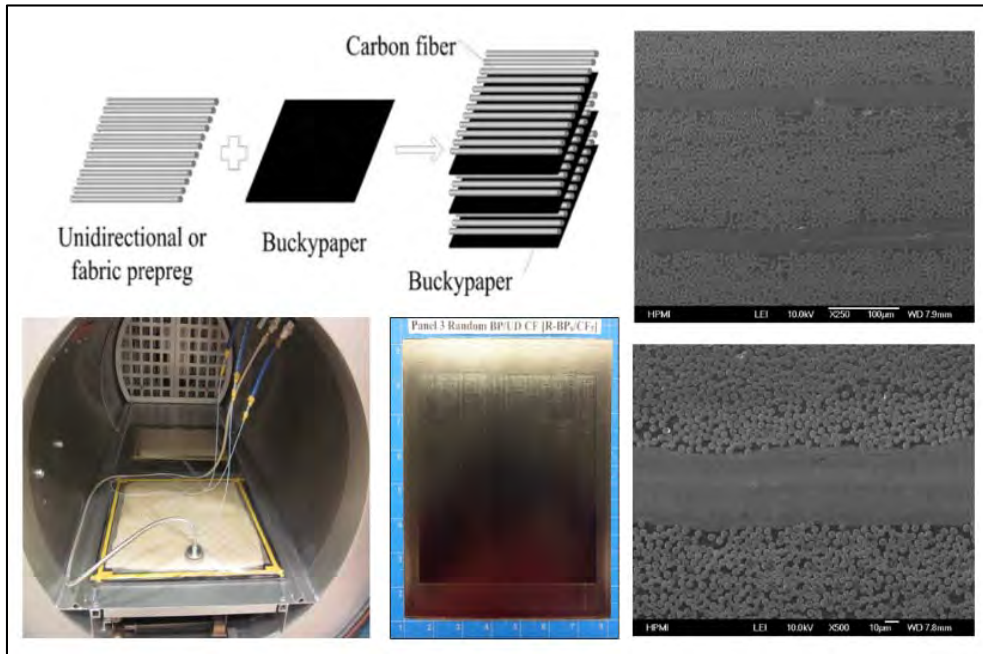


Figure 33. CNT BP/CF hybrid composites: interplay hybrid layup; autoclave process and high quality samples with well resin-impregnated CNT strips and no noticeable resin rich areas and voids

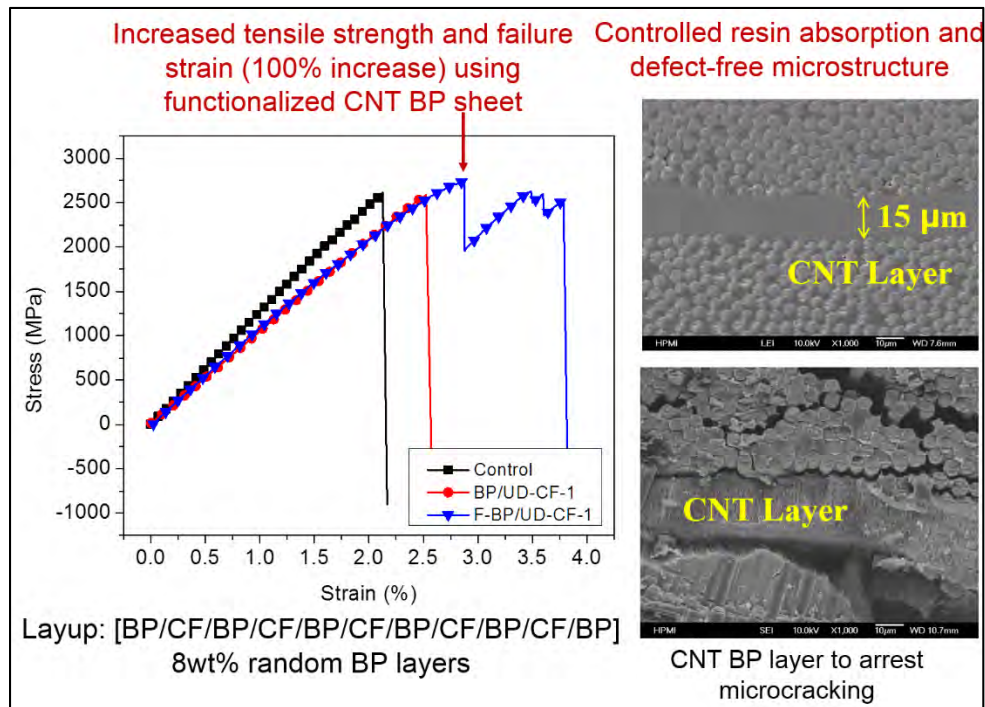


Figure 34. 100% increase of failure strain of the CNT BP/CF hybrid composites with functionalization treatment and improved failure modes

#### 4.1 Permeability of CNT Buckypaper

In contrast to traditional fiber reinforcements, buckypapers are composed of randomly dispersed CNTs of 120 nm diameters, which are much smaller than micron-size reinforcement fibers. The differences of the pore shapes and sizes in CNTs and fiber networks play an important role in composite manufacturing and quality control, especially for resin infiltration and void formation. We<sup>125</sup> measured the through-thickness permeability of SWCNT buckypaper using deionized water under a vacuum. The results revealed a much lower permeability of buckypaper compared to fiber reinforcements. A direct consequence in composite manufacturing involving buckypaper is its inhibition of resin flow and infiltration due to such a low permeability. Inhibited resin flow can trap air within porous structures leading to void formation,<sup>115</sup> Investigating the permeability of buckypapers and the resin infiltration behavior are vital to understanding and optimizing nanocomposite manufacturing.

In this study, the through-thickness permeabilities of buckypaper under different applied pressures were measured and the influential factors on permeability were investigated. The interactions between different working fluids with four types of buckypapers were investigated to reveal the flow behavior deviations from Darcy's law and Kozeny-Carman model.

## 4.2 Materials and Permeability Measurement Setup

### 4.2.1 Buckypaper Materials

The permeability measurements were carried out by using four different types of buckypaper materials: SWCNT buckypaper, two types of MWCNT buckypapers fabricated using a suspension filtration process,<sup>116,117</sup> and one commercial MWCNT nanotube was supplied by Nanocomp. The Nanocomp CNT sheets were produced using a continuous CVD process in which the MWCNTs are directed on a substrate to form thin films. These materials exhibited different nanofibrous structures, which resulted in a unique nano-pore shape and size for each material. Table 5 shows the structural parameters of these buckypapers. Two different types of MWCNTs, SMW100 and SMW200 from SouthWest NanoTechnologies, were used to fabricate MWCNT BP-1 and MWCNT BP-2 samples, respectively. We also used SouthWest SWCNT (CG200) to make SWCNT BP buckypaper. MWCNT BP-3 sample was supplied by Nanocomp using a direct deposition process.

### 4.2.2 Working Fluids

Three types of working fluids were chosen for infiltration: water, acetone and an acetone solution of epoxy resin. These liquids provided different viscosities, polarity and molecular sizes and allowed us to study their interactions with nanoscale fibrous geometries. Bisphenol-A based epoxy-635 resin without a curing hardener was used by mixing with acetone. The mixing ratio of epoxy-635 to acetone was 4:1 by weight. Table 6 lists the densities and viscosities of different liquids used at room temperature.

Table 5. Structural parameters of different buckypapers

	CNT characteristics			Thickness ( $\mu\text{m}$ )	Areal density ( $\text{g}/\text{m}^2$ )
	Type	Diameter (nm)	Length( $\mu\text{m}$ )		
MWCNT BP-1	MWCNT	$\sim 6.6$	$\sim 6.0$	40.0	22.98
MWCNT BP-2	MWCNT	$\sim 10.0$	$\sim 5.0$	43.0	23.15
MWCNT BP-3	MWCNT	6-8 nm	$>1000$	10.0	10.30
SWCNT BP	SWCNT	$\sim 1.0$	$\sim 1.0$	22.4	19.99

Table 6. Properties of infiltration working liquids

Type of liquid	Density (g/cm <sup>3</sup> )	Viscosity (Pa·s)	Suppliers
Water	0.997	$1.05 \times 10^{-3}$	---
Acetone	0.791	$3.06 \times 10^{-4}$	Sigma-Aldrich Co.
Epoxy-635/Acetone solution	1.03	$1.9 \times 10^{-2}$	U.S. Composites Inc.

#### 4.2.3 Permeability Measurement Setup

The through-thickness permeability of buckypaper was tested by using a simple filter apparatus, as shown in Figure 35(a). The buckypaper was placed inside the filter apparatus, which was supported by a metallic porous plate, as shown in Figure 35(b). In order to prevent buckypaper breakage under an applied high pressure during infiltration, a 100  $\mu\text{m}$  thick cellulose nitrate filter paper, produced by Sartorius Stedim Biotech GmbH with a pore size of 0.45  $\mu\text{m}$ , was placed beneath the buckypaper. A 50  $\mu\text{m}$  thick polyester mesh spacer filter paper produced by Sterlitech Corporation was placed under the cellulose nitrate filter to improve the effluent flow. The permeabilities of these filter papers were above  $2 \times 10^{-15} \text{ m}^2$ , much larger than those of buckypaper, so their effect on the test results would be negligible. The buckypaper specimens were cut into round 9 cm diameter discs and sealed with a rubber ring into the filter apparatus to eliminate any edge effect. Compressed air at a constant pressure forced the working fluid from a reservoir container to penetrate buckypaper in the through-thickness direction. The diameter of the effective cross section for liquid infiltration was 7.5 cm. Liquid penetration time was recorded to estimate the unsaturated permeability by recording when the first droplet of effluent filtrate was observed in the outlet. The observed liquid volume vs. time was measured after the buckypaper was fully wetted to determine its saturated permeability.

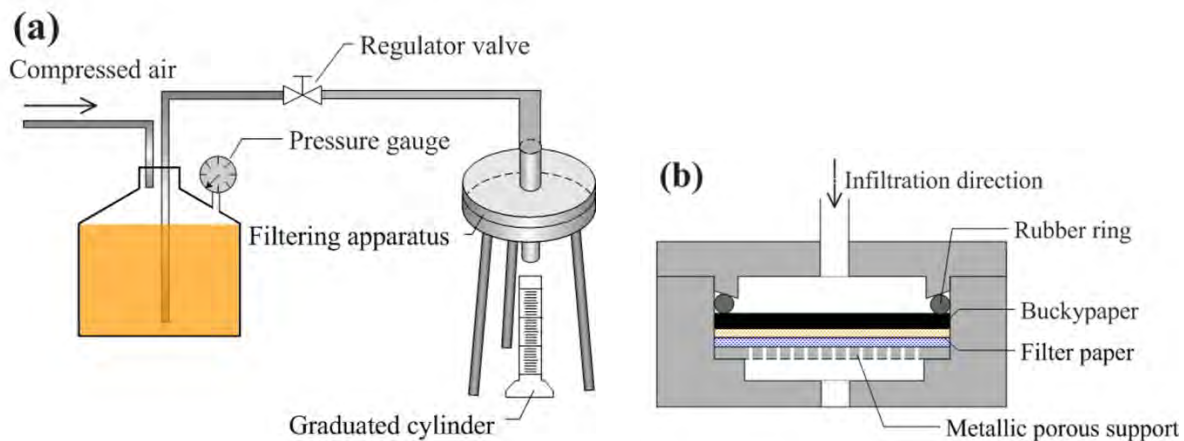


Figure 35. Through-thickness permeability test schematic: (a) measurement apparatus and (b) filtration assembly

#### 4.2.4 Pore characteristics measurement by gas adsorption

Pore size, volume and surface area of the buckypaper were characterized using the physical gas adsorption technique. The tests were using N<sub>2</sub> gas and a Micromeritics Tristar 3000 Pore Size and Surface Area Analyzer. All samples were degassed for 10 hours at 200 °C under a vacuum, which was followed by 2 hours at 200 °C under N<sub>2</sub> flow prior to measurement to clean the surface. The Brunauer, Emmett and Teller (BET) and Barrett, Joyner and Halenda (BJH) models were used to obtain the surface area and pore size characteristics, respectively. The data obtained from the N<sub>2</sub> sorption models were useful for observing trends among the samples in a qualitative or semi-quantitative manner. The porosity values of the samples were estimated from pore volume and bulk density, as shown in Table 7. However, due to the complexity of gas absorption in nanostructured carbons and the numerous assumptions involved in each model, caution was taken in attempting to determine the quantitative comparisons with other materials or values obtained from other characterization methods.

Table 7. Pore characteristic parameters of different buckypapers

	BET area (m <sup>2</sup> /g)	Pore width (nm)	Porosity (%)
MWCNT BP-1 (Pristine)	207.5	16.0	58.6
MWCNT BP-1 (Heat-treated)	229.3	17.3	66.5
MWCNT BP-2	184.0	15.1	44.7
MWCNT BP-3	161.5	15.4	71.8
SWCNT BP	415.4	6.9	67.9

### 4.3 Permeability Estimation Model

During the infiltration process, liquid penetrated the dry buckypaper. Rates for liquid infiltration into nanoscale pores were different based on the widths. This caused the complete saturation of buckypaper to be delayed. Unsaturated infiltration occurred at the beginning of the infiltration process.

#### 4.3.1 Unsaturated infiltration

Darcy's Law is widely used to describe infiltration behaviors of porous media by assuming a liquid as a Newtonian fluid,

$$\bar{v} = -\frac{\bar{K}}{\eta} \cdot \nabla P \quad (8)$$

where  $\bar{v}$  is the flow velocity of a working fluid infiltrating into porous medium,  $\bar{K}$  is the permeability,  $\eta$  is the liquid viscosity, and  $\nabla P$  is the pressure difference to drive the infiltration.

We attempted to see whether buckypaper with nanoscale pores followed Darcy's Law through permeability measurements and analysis.

Although Darcy's Law was developed for saturated flow in the microscale porous media, it has been widely used for unsaturated flow in the composite materials manufacturing field for resin infiltration into dry fiber preforms.<sup>118</sup> At the beginning of liquid penetration into a dry buckypaper, unsaturated flow will occur when the buckypaper is not completely filled with liquid. Darcy's Law in one-directional form<sup>119</sup> can be expressed as

$$\frac{dL}{dt} = \frac{K_{zu}}{\eta(1-V_f)} \frac{dP}{dL} \quad (9)$$

where L is the infiltration distance at time t, and  $K_{zu}$  is the unsaturated through-thickness permeability of buckypaper. During infiltration, a constant air pressure  $P_{air}$  was applied. By observing the existing of a threshold pressure ( $P_T$ ) for the liquid to penetrate buckypaper, this parameter,  $P_T$ , can be designed to describe the effect of the interaction between CNTs and the working liquid, and then equation (9) can be further integrated to produce

$$\frac{L^2}{t} = \frac{2K_{zu}}{\eta(1-V_f)} P_{air} + \frac{2K_{zu}P_T}{\eta(1-V_f)} \quad (10)$$

By plotting  $L^2/t$  against  $P_{air}$ , a straight line should fit the line with

$$Slope = a' = \frac{2K_{zu}}{\eta(1-V_f)} \quad (11)$$

And then unsaturated permeability,  $K_{zu}$ , can be estimated by the relation

$$K_{zu} = \frac{a'\eta(1-V_f)}{2} \quad (12)$$

### *Saturated infiltration analysis*

After the buckypaper was fully wetted or penetrated, Darcy's Law in saturated flow can be written as

$$Q = \frac{K_{zs}AP}{\eta L} \quad (13)$$

where Q is the flow rate, and A is the cross section of the buckypaper. Taking into account that

$$P = P_{air} + P_T \quad (14)$$

Equation 12 can be rewritten as

$$Q = \frac{K_{zs}A}{\eta L} P_{Air} + \frac{K_{zs}AP_T}{\eta L} \quad (15)$$

By plotting Q against P<sub>air</sub>, a straight line should fit the line with

$$Slope = a = \frac{K_{zs}A}{\eta L} \quad (16)$$

$$Incept = b = \frac{K_{zs}AP_T}{\eta L} \quad (17)$$

Then, the saturated permeability K<sub>zs</sub> and P<sub>T</sub> can be estimated respectively,

$$K_{zs} = \frac{a\eta L}{A} \quad (18)$$

$$P_T = \frac{b}{a} \quad (19)$$

#### **4.4 Permeability Results**

From the experimental results and model calculations, we found that liquid permeated into the buckypaper gradually faster until a constant flow rate was reached, which indicates unsaturated infiltration lasted for a period of time before saturation. Low viscosity and high pressure can effectively accelerate saturation. Therefore, we infiltrated the liquid under 400 kPa of pressure for about 5 minutes before we conducted saturation measurements to ensure the samples were fully wetted. Figure 36 shows the liquid volume vs. time plots for saturated infiltration under different applied air pressures. The good linear relationship indicated a constant flow rate, which can be calculated from the slope. The data revealed a relationship that would be expected from saturated permeation.

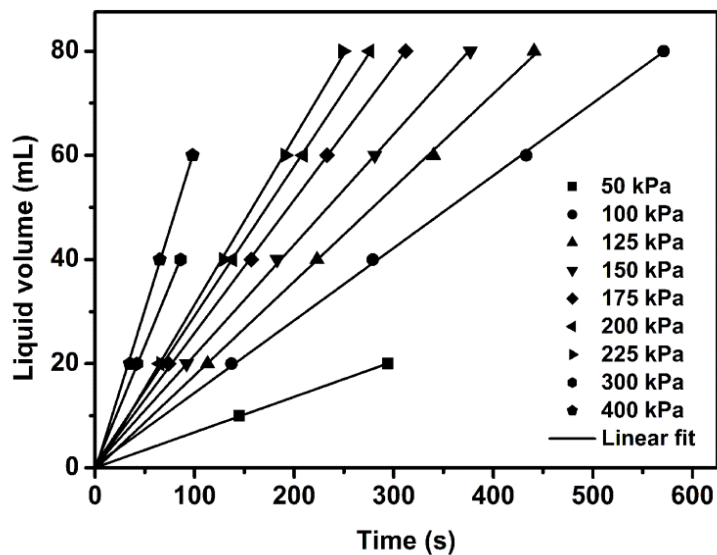


Figure 36. Plots of water infiltration volume vs. time under different air pressures of pristine MWCNT BP-1 sample

Assuming  $P_T=0$  Pa in the model to neglect the interaction effects, we can estimate saturated permeability based on each individual infiltration experiment under different applied pressures. The filled solid bar in Figure 37 shows the saturated permeability results. As an important material constant, permeability was only determined by the pore characteristics based on Darcy's Law. However, the resultant permeability noticeably increased with the increase of the test pressures, which conflicted with the observed linear relationships following Darcy's Law. The significant difference in pore sizes between the reinforcement fiber preform and buckypaper materials, as shown in Table 7, may be caused by more intensive interactions between CNTs and working liquids resulting from its nanoscale pores. In order to quantify such effects, a threshold pressure ( $P_T$ ) was defined as the interaction effect and introduced into Equation (15).

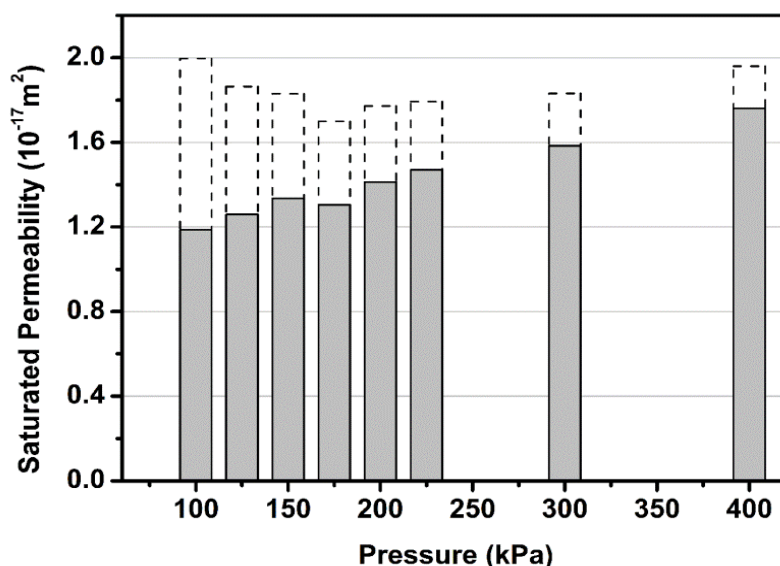


Figure 37. Saturated permeabilities of buckypaper from infiltration under different applied air pressures using Equation (15) by assuming  $PT=0$  (Solid bar) and with  $PT$  effect using the experimental threshold pressure value calculated from Equations (17-19) (Hollow bar)

Figure 38 presents the plots of flow rate vs. applied pressure for water permeation into pristine and heat treated MWCNT BP-1 samples. The plots of the data exhibited a good linear relationship. The threshold pressure was determined as  $-40.6$  kPa from the slope and intercept, according to Equation (19), indicating the pressure that must be exceeded for saturated infiltration. By substituting the experimental threshold pressure into Equation (15), we can correctly calculate the saturated permeability values for each individual infiltration experiment under different pressures as shown by the hollow dash bar in Figure 37. The measured permeability under different pressures remained relatively constant, which was predicted by Darcy's Law. We also believe that for a specific buckypaper and working liquid situation, the threshold pressure should be constant as determined by its nanoscale pore size and shape, and their interaction with working fluid. This also explains the inverse relationship between higher applied air pressure and decreased influence of the interaction component (Equation (15)) on permeability estimates. Only corrected permeability will be used in the following discussion.

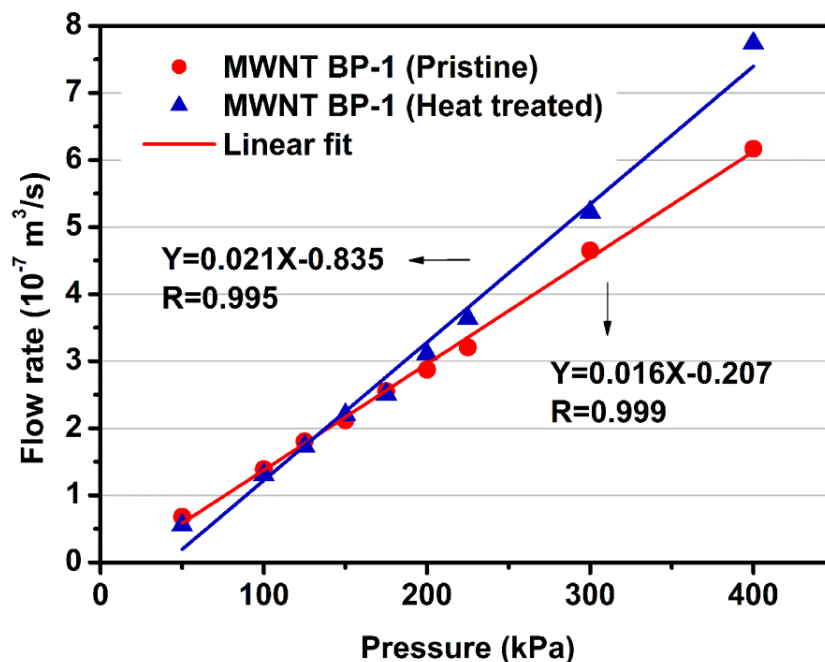


Figure 38. Variation of flow rate of water vs. applied pressure of pristine and heat treated MWCNT BP-1 samples

The unsaturated and saturated through-thickness permeabilities of buckypaper were 4-6 orders of magnitude lower than carbon fiber reinforcement with about 60% fiber volume fraction,<sup>120</sup> which is approximately  $1 \times 10^{-13} \text{ m}^2$ . This indicates that prolonging a low viscosity processing window would be necessary for resin infiltration into and expelling trapped air from the buckypaper during nanocomposite manufacture. The unsaturated permeability was lower than the saturated permeability for buckypaper, similar to what has been observed in carbon fabric preforms,<sup>121</sup> This phenomenon might be caused by the lubrication effect of adsorbed water on the CNT surface reducing fluid drag in saturated infiltration. Figure 38 shows that the resultant saturated permeabilities of the pristine buckypaper and heat treated buckypaper were  $1.44 \times 10^{-17} \text{ m}^2$  and  $1.87 \times 10^{-17} \text{ m}^2$ , respectively. Removal of surfactant enhanced both the saturated and unsaturated permeabilities by increasing the average pore diameter and overall pore volume.

To investigate the effects of buckypaper thickness on permeability, we carried out permeability tests by using MWCNT BP-1 manufactured with thicknesses of 40 and 80  $\mu\text{m}$ . Figure 39 shows the plots of water flow rate and applied pressure. Thickness affected the flow rate under identical pressure conditions due to changes in the flow path length. Buckypapers with higher thicknesses, and therefore, longer flow paths, exhibited lower flow rates during permeability testing. The permeability of the MWCNT BP-1 with 80  $\mu\text{m}$  thickness was measured as  $1.98 \times 10^{-17} \text{ m}^2$ , close to the results of  $1.87 \times 10^{-17} \text{ m}^2$  of 40  $\mu\text{m}$  thick buckypaper. This indicated that buckypaper permeability was not affected by its thickness. The variation in buckypaper preform thickness did not change nanoscale pore geometries inside the mat, which was different from reported gas permeability of foam film with nanoscale pores.<sup>122</sup>

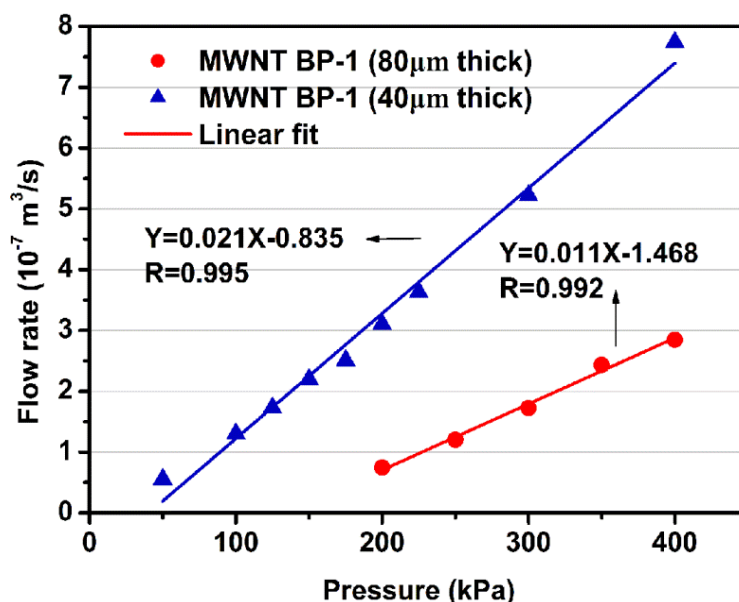


Figure 39. Variation of water flow rate vs. applied pressure for the MWCNT BP-1 samples with thicknesses of 40 and 80  $\mu\text{m}$

#### 4.5 Nanoscale Pore Characteristics-Permeability Relationships

In order to study the effects of pore characteristics on permeability, the infiltration behaviors of four different types of buckypapers were compared, which are shown in Figure 40. The flow rate of water permeation into buckypaper decreased in the order of MWCNT BP-3, MWCNT BP-1, MWCNT BP-2 and SWCNT BP under the same experimental conditions. Table 8 shows the resultant permeabilities of different buckypapers as calculated from Figure 40. The SWCNT BP buckypaper exhibited the lowest permeability of  $2.42 \times 10^{-19} \text{ m}^2$ , which was two orders of magnitude lower than the MWCNT buckypapers. Three MWCNT buckypapers displayed smaller differences in permeability. Among them, MWCNT BP-3 had the highest permeability of  $2.40 \times 10^{-17} \text{ m}^2$ , and MWCNT BP-2 provided lowest permeability of  $1.07 \times 10^{-17} \text{ m}^2$ .

The surface area, pore width and porosity of different buckypapers were characterized by a gas adsorption analysis.<sup>123</sup> Figure 41 shows the Barrett, Joyner and Halenda pore size distribution for different buckypapers. The SWCNT buckypaper presented a much narrower distribution of pore widths than the MWCNT samples. Table 7 lists the results of BET surface area, average pore width and porosity. The SWCNT BP exhibited the highest BET area of  $415.4 \text{ m}^2/\text{g}$  and the smallest pore width of 6.9 nm, which was the most likely reason for the inhibition of liquid infiltration and low permeability. The larger pore width of 15.4 nm, high porosity of 71.8% and low BET area of  $161.5 \text{ m}^2/\text{g}$  of MWCNT BP-3 contributed to its high permeability.

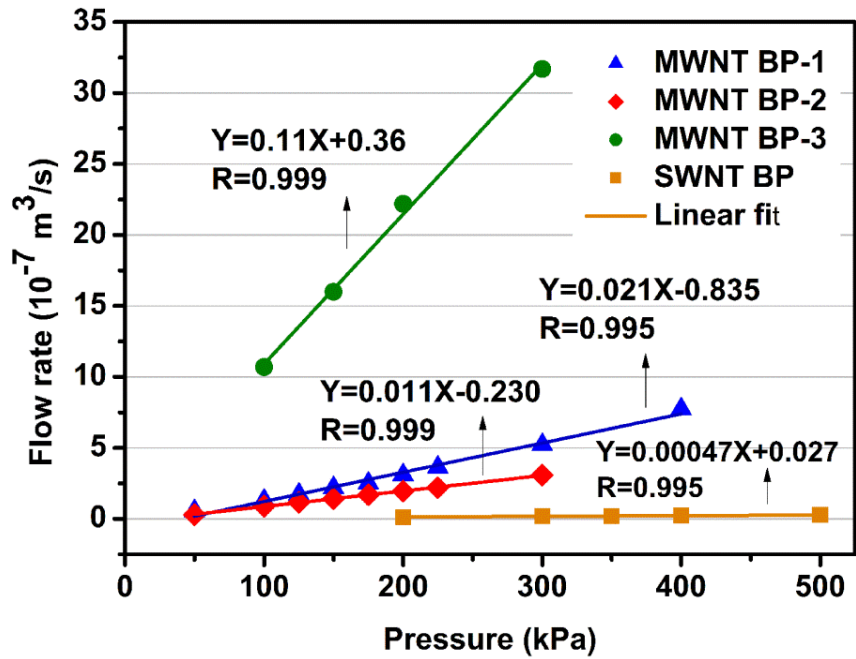


Figure 40. Plots of flow rate vs. pressure for four different buckypapers

Table 8. Permeabilities and threshold pressures tested by different liquids

	Water		Acetone		Epoxy-635/Acetone
	Permeability (m <sup>2</sup> ) / (C.V.)	Threshold pressure (kPa)	Permeability (m <sup>2</sup> ) / (C.V.)	Threshold pressure (kPa)	Permeability (m <sup>2</sup> ) / (C.V.)
MWNT BP-1	1.87×10 <sup>-17</sup> (5.3%)	-40.6	1.83×10 <sup>-17</sup> (9.5%)	-14.5	1.23×10 <sup>-17</sup> (0.7%)
MWNT BP-2	1.07×10 <sup>-17</sup> (2.2%)	-21.0	1.06×10 <sup>-17</sup> (10.2%)	-34.6	7.38×10 <sup>-18</sup> (2.1%)
MWNT BP-3	2.40×10 <sup>-17</sup> (2.4%)	3.41	2.60×10 <sup>-17</sup> (4.9%)	9.15	1.67×10 <sup>-17</sup> (3.7%)
SWNT BP	2.42×10 <sup>-19</sup> (3.3%)	56.8	4.39×10 <sup>-19</sup> (4.2%)	91.2	9.22×10 <sup>-20a</sup>

a Permeability at initial stage was tested under applied pressure of 500 kPa.

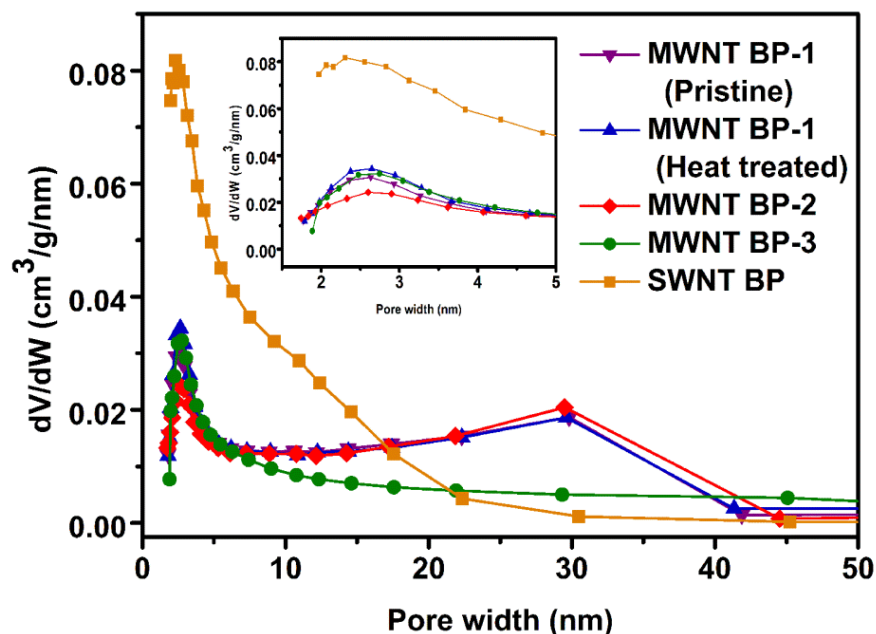


Figure 41. Barrett, Joyner and Halenda pore size distribution derived from the gas adsorption analysis

The classical microstructure-permeability relationship can be described by Kozeny-Carman equation<sup>124</sup>,

$$K = \frac{\varepsilon^3}{cS_v^2(1-\varepsilon)^2} \quad (20)$$

where  $K$  is permeability,  $\varepsilon$  is porosity,  $c$  is Kozeny constant, and  $S_v$  is specific surface area per unit volume, which was calculated by multiplying BET specific surface area by the buckypaper bulk density. The Kozeny constant is a factor affected by pore geometry and the tortuosity of flow path. This constant is typically assigned a value of 5 based on an assumption of a packed bed system of spherical particles.<sup>125,126</sup> However, many nanofiltration results have shown a large variation for this constant.<sup>127</sup> By applying the permeability, porosity and surface area parameters of the buckypaper samples into Equation (21), we can calculate Kozeny constants as 8.1, 2.8 and 7.0 for MWCNT BP-1, MWCNT BP-2 and MWCNT BP-3, respectively. These results were in the reported range of 2.2 to 9.0 for filamentous and pelleted mycelial cultures with the similar network structures by Oolman.<sup>128</sup> The SWCNT BP had a Kozeny constant of 91.4, most likely as a result of smaller pore diameter and high BET area. The Kozeny constant was influenced by the combination of the pore structural parameters, as shown in Figure 42. Larger porosity, larger surface area and smaller pore width appear to contribute to a larger Kozeny constant.

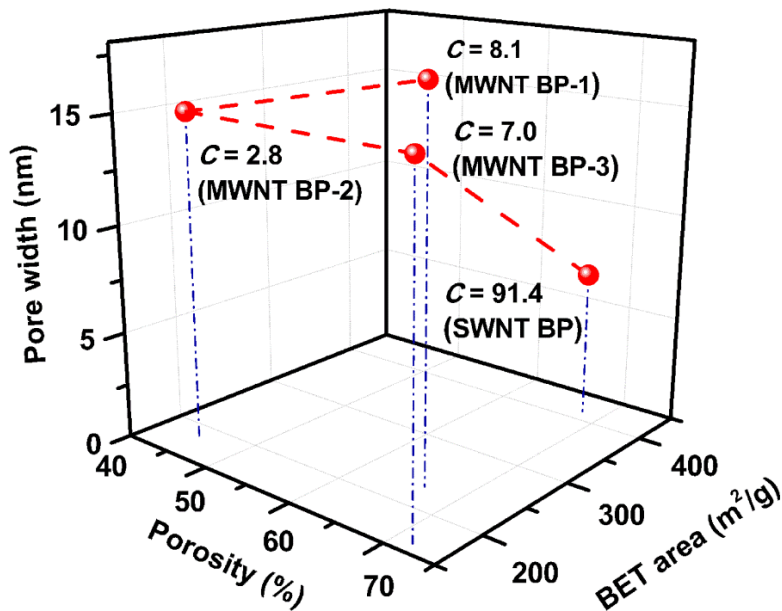


Figure 42. Pore structural parameters and Kozeny constants of different buckypapers

In summary, the effects of CNT geometry, heat treatment, porous structures and type of working fluid on permeability of different buckypaper materials were studied. We found that the infiltration behavior into the buckypaper was in agreement with Darcy's Law, except in the case of epoxy resin solution permeation into SWCNT buckypaper. Buckypaper permeabilities are in the order of magnitude of  $10^{-17}$ – $10^{-19}$  m<sup>2</sup>, which are 46 orders of magnitude lower than fiber reinforcements ( $10^{-13}$  m<sup>2</sup>) preform. This is most likely due to their nanoscale pore characteristics. The permeability of SWCNT buckypapers was two orders of magnitude lower than MWCNT buckypapers. Larger pore widths, larger porosity and smaller surface areas contributed to a larger permeability, which was consistent with the Kozeny-Carman model. The Kozeny constants of buckypaper were well correlated with tortuosity of flow path and pore characteristics. SWCNT buckypaper provided the largest Kozeny constant because of its long and narrow pore shape and high tortuosity. When using water and acetone as the working fluids, no visible difference resulted in the permeability. Epoxy solutions produced lower permeability due to the occurrence of pore blockage from molecular filtering. In addition, the threshold pressure of liquid infiltration for buckypaper materials can be either negative or positive depending on their pore characteristics. Those fundamental understanding of permeability properties of CNT networks with nanoscale porous structures is essential for developing nanocomposite manufacturing process which will be discussed in the following sections.

#### ***4.6 Manufacturing Challenges of CNT Buckypaper/CF Hybrid Composites***

We studied the use of CNT thin film or buckypaper, integrated into carbon fiber (CF) prepreg composites to create hybrid composite materials to achieve high CNT content while maintaining the outstanding mechanical properties of CF composites. The autoclave process of manufacturing hybrid composite laminates was investigated to gain an understanding of nano/micro dual-scale resin flow characteristics and impregnation mechanisms. Tensile properties and failure modes of the resultant composites were studied. The study found that resin bleeding along the through-thickness direction was inhibited due to extra-low permeability and high resin absorbing capacity of the buckypaper, which was the major contributing factor to void formation and resin starvation defects in resultant buckypaper/CF hybrid composites. Resin matrix-impregnated buckypaper layers were much thicker than dry pristine buckypaper due to high resin absorbency and swelling effects. The increase of buckypaper content reduced the global fiber concentration but increased the global resin concentration in the hybrid composites. Control and hybrid composites showed similar fiber volume fractions in the carbon fiber plies. The buckypaper/unidirectional (UD) carbon fiber hybrid composites with local fiber volume had comparable tensile moduli and strength as the control samples, but demonstrated significant improvements in failure strain. The dramatic improvements in both in-plane and through-thickness electrical conductivities demonstrate potential for both structural and multifunctional applications of the resultant hybrid composites.

#### ***4.7 Experimental***

##### ***4.7.1 Materials***

Nanocomp Technologies (NH, USA) supplied the CNT sheets, which were 1015 $\mu\text{m}$  thick, with an areal density of approximately 9.7g/m<sup>2</sup>. Cytec Engineered Materials (Woodland Park, USA) supplied the unidirectional IM7/CYCOM® 5250-4 prepreg, which had an areal density of 210 g/m<sup>2</sup> and a resin content of ~32 wt%. In addition, we also used IM7 GP-6k plain weave fabric in the study. The fabric prepreg was manufactured with a CYCOM 890 resin system, which is a low viscosity epoxy resin with a long shelf life. This fabric prepreg was made in-house by infusing CYCOM 890 resin into the fabrics. IM7 GP-6k plain weave fabric with an areal density of 190 g/m<sup>2</sup> was purchased from Textile Products, Inc. (Anahiem, USA). A single layer of carbon fabric was vacuum-bagged in a flat steel mold. The assembly was placed in an oven and CYCOM 890 resin was infused at 80 °C. After the fabric was completely impregnated, the prepreg was harvested and stored in a refrigerator for hybrid composite fabrication.

##### ***Fabrication of BP/CF interply hybrid composites***

Buckypaper's nanoscale porous structures and large surface area resulted in a very low permeability relative to unidirectional carbon fiber tapes and carbon fabrics as discussed in Sections 4.1-4.5. This phenomenon presents major challenges for making high quality composites using buckypaper or CNT materials. Two methods were used to prepare the BP/CF

interply hybrid composites to study the behavior of resin flow and impregnation within the buckypaper and carbon fiber layers. Table 9 shows the sample layup design. These two processes were denoted as “dry buckypaper lay-up process” and “buckypaper prepreg lay-up process,” respectively. Figure 33 shows the manufacturing process of the hybrid composite. Carbon fiber unidirectional prepreg or fabric prepreg were used in both methods to study their effects on the manufacturing processes.

In the dry buckypaper lay-up process, carbon fiber prepreg and dry buckypaper materials were laminated according to a designed stacking sequence on a steel mold. The overall lay-up sequence from the bottom-to-top on the mold-surface was in the following order: release film, interply hybrid structure made of alternating carbon fiber and buckypaper layers, peel ply, caul plate, breather and vacuum bagging film. The assembly was finally vacuum-bagged under a full vacuum to expel air. BP/CF hybrid composites were cured using an autoclave process following the CYCOM 5250-4 or CYCOM 890 curing schedules. A vacuum was applied to the final assembly for 1 hour before starting the curing and venting when the pressure reached 207 kPa. By heating and applying pressure to the assembly during the autoclave process, the resin in the carbon fiber prepreg was forced to flow into the adjacent dry buckypaper layer causing through-thickness impregnation. The curing schedule of CYCOM 5250-4 was modified to allow a longer period of time at 121 °C, which was used to keep the resin with a low viscosity for promoting resin flow from the carbon fiber prepreg into dry buckypaper. The composites using CYCOM 5250-4 resin was cured at 177 °C and 0.69 MPa for 6 hours, following by a post-cure process at 227 °C for 4 hours. The composites using CYCOM 890 resin was cured at 180 °C and 0.69 MPa for 3 hours.

For the buckypaper prepreg lay-up process, pre-impregnated buckypapers were prepared prior to composite manufacturing. Figure 33 shows in-house made large size BP/CYCOM 5250-4 prepreg. The lay-up sequence for the autoclave manufacturing process was identical to the dry buckypaper lay-up process for all hybrid composite fabrication. The resin matrix was partially cured during buckypaper prepreg preparation, so the low temperature stage was skipped during the curing. The final sample panel size was 200×250 mm<sup>2</sup>, as shown in Figure 33.

#### *4.7.3 Characterization*

Tensile property tests were conducted following the ASTM D 3039 standard using an MTS Landmark test system. A non-contact video extensometer monitored and recorded the specimen strain to calculate the tensile modulus. The specimens for BP/CF unidirectional and fabric hybrid samples were prepared in the dimensions of 15×250 mm<sup>2</sup> and 25×250 mm<sup>2</sup>, respectively. The control samples were the same sizes as their corresponding BP/CF hybrid counterparts. E-glass fiber reinforced epoxy tabs were used for the testing samples. The crosshead speed of the test machine was 1mm/min. The SEM samples were cut using a diamond blade. Specimen cross sections were produced by grinding with 1200 grit sandpaper and polished using 3 μm diamond suspension on a polishing machine. The sample surface was coated with a gold layer and

observed using a SEM machine (JEOL JSM-7401F USA, Inc.). Electrical conductivity was measured via a two-point method with the specimen dimension of  $5 \times 1 \text{ cm}^2$ . The two ends of the sample were polished and electrodes were connected using silver paste for better electrical contact conduction during the measurements.

Table 9. Structural parameters of BP/CF interply hybrid composite

	BP/UD-CF-1	BP/UD-CF-2	UD-CFRP Control	BP/PW-CF-1	PW-CFRP control	BP control
Lay-up	[BP/CF/BP/C F/BP/ $\overline{CF}$ ] <sub>s</sub>	[BP <sub>2</sub> /CF/BP <sub>2</sub> / CF/BP <sub>2</sub> / $\overline{CF}$ ] <sub>s</sub>	[0] <sub>6</sub>	[BP/CF/BP/CF/B P/CF/ $\overline{BP}$ ] <sub>s</sub>	[CF] <sub>6</sub>	[BP] <sub>6</sub>
Thickness (mm)	0.80	1.02	0.81	1.23	1.07	0.11
Density (g/cm <sup>3</sup> )	1.56	1.52	1.57	1.56	1.58	1.42
Global fiber content (wt%)	56.29	45.46	66.46	69.40	77.75	---
Global CNT content (wt%)	4.95	7.99	0	3.02	0	40.98
Global matrix content (wt%)	38.76	46.55	33.54	27.58	22.25	59.02
Local fiber volume fraction in CF ply (v%)	61.46	54.25	58.51	59.96	59.86	---
Local CNT volume fraction in BP ply (v%)	26.57	28.60	---	30.14	---	35.70
Process	BP prepreg lay-up process	BP prepreg lay-up process	---	Dry BP lay-up process	---	---
Type of CF prepreg	UD IM7/5250-4	UD IM7/5250- 4	UD IM7 /5250-4	PW IM7/Cycom 890	PW IM7/Cycom 890	---

## ***4.8 New Resin Flow Behavior and Manufacturing Challenges in Autoclave Process for BP/CF Hybrid Composites***

### *4.8.1 Extra-low permeability of CNT buckypaper eliminated through-thickness resin flow*

During conventional fiber laminated composite autoclave processing, the predominant resin flow occurred along the through-thickness direction within the fiber-reinforced laminates.<sup>129</sup> This resin flow is governed by resin rheology, the through-thickness permeability and process pressure of the reinforcement networks following Darcy's Law. In the case of the buckypaper and carbon fiber interply hybrid composites, resin flow occurred in both nanoscale and microscale pores during the autoclave process. The carbon fiber network primarily has a microscale pore structure, and the buckypaper layers predominately have a nanoscale pore structure, leading to large differences in permeability. The through-thickness permeability of buckypaper has been measured to be on the order of  $10^{-19}$  to  $10^{-17}$  m<sup>2</sup> (see *Sections 4.2-4.7*).<sup>107</sup> This is about four to six orders of magnitude lower than conventional carbon fiber reinforcements with about 60% fiber volume fraction, which is approximately  $10^{-13}$  m<sup>2</sup>. Despite the low permeability, the buckypaper absorbed and retained a large amount of resin during the autoclave curing process. This is likely caused by a strong capillary pressure for resin imbibitions due to an average nanoscale pore width of 11.66 nm in the buckypaper layer, based on BET test.<sup>107,124</sup> According to the Young-Laplace equation,<sup>130</sup> the capillary pressure is in inverse proportional relationship to the effective mean pore diameter. The diameter of IM7 fiber was 5.2 μm. The effective mean pore diameter of carbon fiber perform was calculated as approximately 3.5 μm at fiber volume fraction of 60%, which was much higher than the nanoscale radius of the CNT network.<sup>131</sup> This nanoscale pore size of the CNT sheet was most likely the cause of extremely high capillary pressure. CNTs were randomly oriented in the sheet, which resulted in small contact areas between the individual CNTs or their bundles and small van der Waals interactions at those junctions. The low viscosity resin at the evaluated processing temperature could possibly infiltrate between these CNT contact areas leading to swelling of the CNT layer, and further reducing the CNT/CNT contact area<sup>132</sup>.

The buckypaper imbibition behavior and swelling effects were illustrated by the dramatic increase in thickness during resin impregnation of the buckypaper layers under different processing conditions. Figure 43 shows the suggested resin flow mechanism in the dry buckypaper lay-up process. With increasing temperature, the resin viscosity decreased and allowed the resin to infiltrate into the buckypaper under the combined effects of capillary forces and applied pressures. Figure 43b shows this phenomenon. At this stage, through-thickness resin infiltration from carbon fiber prepregs to dry buckypapers became the main form of resin flow. Simultaneously, the carbon fiber plies were gradually compacted as the resin flowed into the buckypaper. Due to buckypaper's extremely low permeability, it was more difficult for resin to flow through the buckypaper than the carbon fiber layer. From the SEM observations of the testing samples, the thicknesses ratio of carbon fiber layer to buckypaper layer was approximately 5:1, and thus the calculated saturated flow rate through carbon fiber layer was

almost 2000 times faster than that through buckypaper layer, according to a simple estimation of one-direction flow from Darcy's Law. Resin bleeding along the through-thickness direction of laminates was largely inhibited by buckypaper layers, as shown in Figure 44. After the buckypaper was fully impregnated, the resin must bleed out at the laminate edges, as shown in Figure 43(c), and the carbon fiber layer could be further compacted due to the resin edge bleeding. The buckypaper selected for our research had a specific surface area of approximately  $179.2 \text{ m}^2/\text{g}$ , which was orders of magnitude higher than IM7 carbon fiber with a specific surface area of approximately  $1.4 \text{ m}^2/\text{g}$ . The high specific surface area of buckypaper easily led to entrapment of the absorbed resin. In the case of using buckypaper prepreg in the hybrid composite, the predominant resin flow behavior was in-plane bleeding within the carbon fiber layers, as displayed in Figure 43(c), due to the extra-low permeability of the buckypaper layer inhibiting the through-thickness flow.

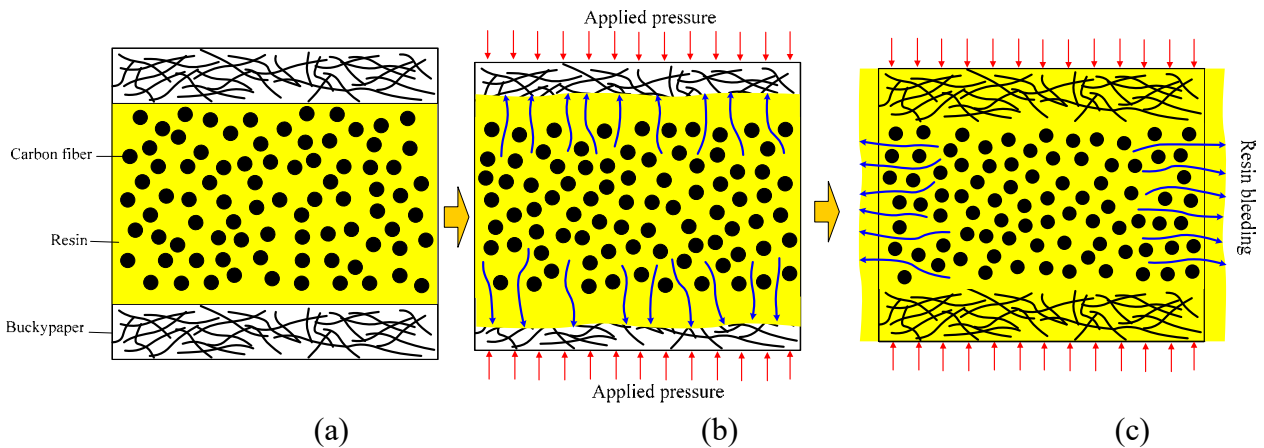


Figure 43. Resin flow model in autoclave processing for BP/CF interply hybrid composite fabrication: (a) initial hybrid structure layup, (b) resin flow along through-thickness direction into dry buckypaper, and (c) resin bleeding out from the sides of the carbon fiber prepreg layer after full impregnation of the buckypaper



Figure 44. Comparison of through-thickness resin flow during autoclave process of the buckypaper/CF hybrid laminate composites (the two without red color resin marks in the middle) and their control sample (CF prepreg laminates with uniform red resin marks in the middle)

#### *4.8.2 Resin starvation in carbon fiber layer and strong resin absorption of buckypaper layer*

Figure 45 shows the typical defects observed in the hybrid composites. These defects were found to closely correlate to the measured resin and buckypaper contents. We chose different types of buckypapers and lay-up designs to achieve 2040 wt% global resin contents and 320 wt% global CNT contents. The composite quality was evaluated by SEM analysis. Resin-starved regions and voids were found to be the most common defects in the BP/CF hybrid composite. The resin-starvation defects were directly related to the high resin absorbency of the buckypaper layers, especially for the dry buckypaper-based hybrid laminates. From the resultant cross-sectional morphology, shown in Figure 45d, when global resin content was lower than 30 wt%, resin-starvation defects tended to appear within the carbon fiber laminas. This type of defect is due to stronger capillary forces in the buckypaper layers compared to that of the carbon fiber networks – a result of the nanoscale capillary radius of buckypaper. The resin was absorbed into the buckypaper layer, leading to CF layer resin-starvation. When resin-starvation defects occurred, no resin bleeding was observed at the laminate edges during fabrication process.

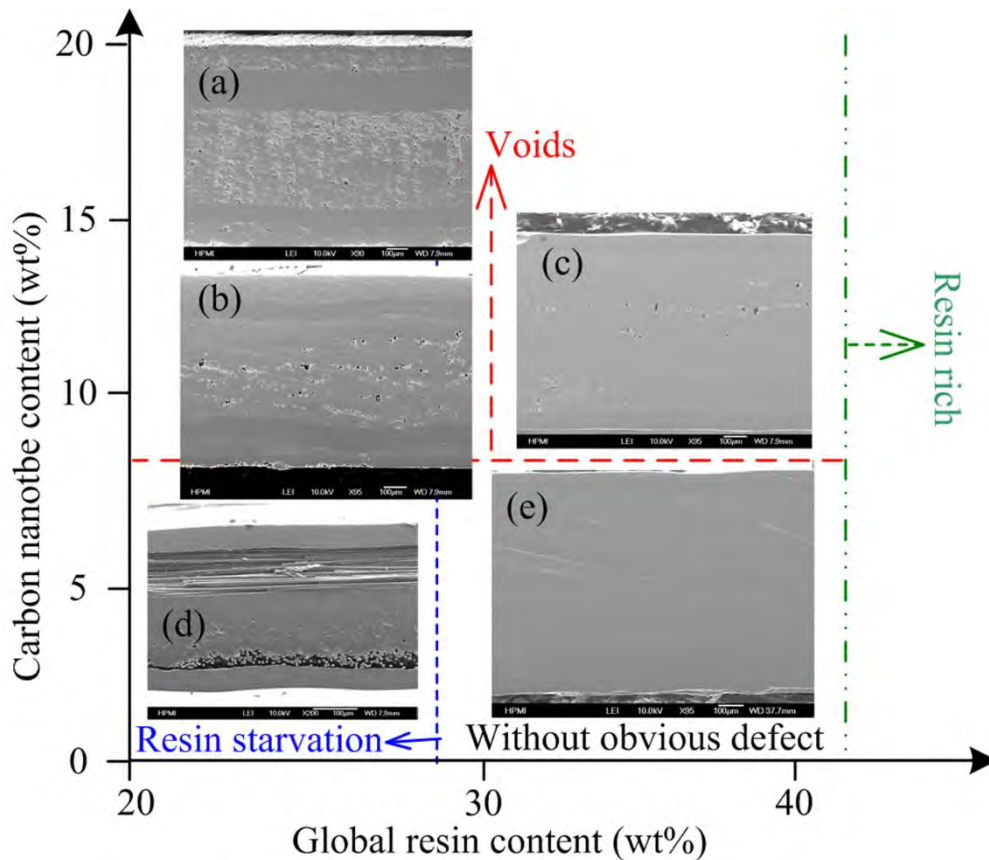


Figure 45. Effects of buckypaper layer and resin content of CF prepreg on typical defect formation in BP/CF hybrid composites

#### 4.8.3 Void formation in carbon fiber layers due to flow barrier effect of buckypaper layers

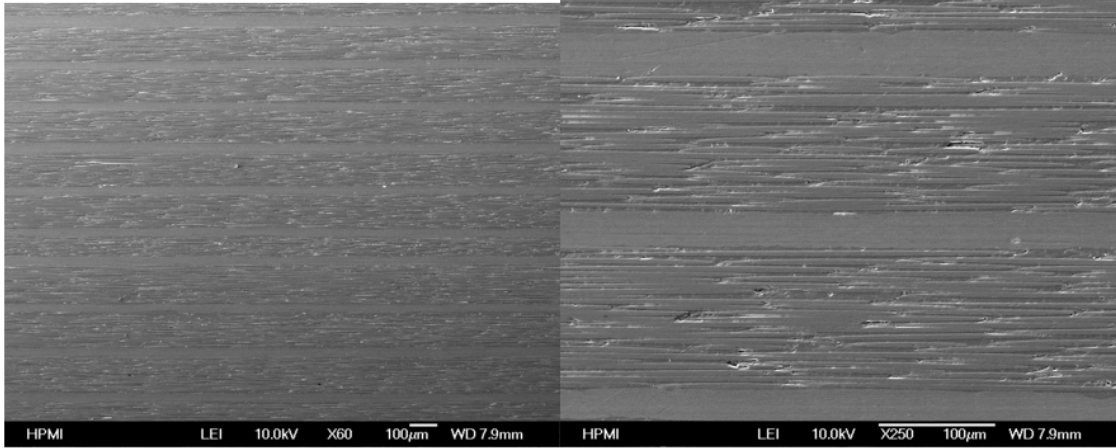
Defect formation was closely related to the resin impregnation mechanism during the autoclave process. As shown in Figures 43 and 44, the resin was absorbed by the buckypaper from the carbon fiber layers until the buckypaper was saturated. Void defects were formed due to the excessive resin bleeding out from carbon fiber layers. Meanwhile, under vacuum pressure during the autoclave process, the volatiles in the resin were likely to start boiling and push more resin bleeding away from the carbon fibers as a result of gas bubble formation and movement,<sup>145</sup> also resulting in creating voids. Adequate resin bleeding is critical for bubble transport out of the composite laminate to reduce voids content. Low buckypaper permeability and resin-starvation in the CF layers inhibited resin flow and the transport of bubbles out of the composite layup. The hybrid composite with a global resin content of 25 wt% and buckypaper content of approximately 20 wt% showed a porosity of 14.1 vol.% (Figure 45a). When CNT content exceeded 10 wt%, resin flow was significantly inhibited, and buckypaper acted as a barrier to the through-thickness flow due to its low permeability. In such cases, as shown in Figure 45(b), bubbles in carbon fiber layers were not able to be expelled, resulting in a high void content. In contrast to the CF layers, SEM examination indicated that the buckypaper laminas were usually fully impregnated without visible defects. With the decrease of buckypaper content to

approximately 10 wt%, the porosity decreased to 2.7 vol.% (Figure 45c). When global resin content further increased to 30 wt%, the porosity decreased to 1.0 vol.%, as shown in Figure 45(e). Under these conditions, visible resin bleeding at the sample edge was typically observed. For Table 9 the unidirectional hybrid composites for tensile tests were prepared by using buckypaper prepreg lay-up process, and the fabric hybrid composites were prepared by using dry buckypaper lay-up process. All these samples had porosity lower than 1.5%.

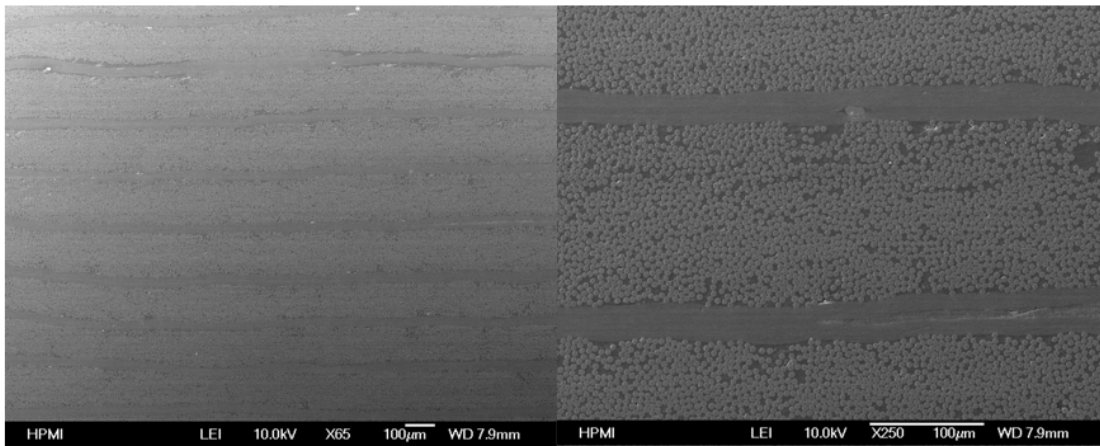
#### ***4.9 Aerospace-grade Quality of CNT BP/CF Hybrid Composites***

Figure 46 shows the typical cross-sectional morphology of buckypaper and unidirectional carbon fiber hybrid composite BP/UD-CF-1, longitudinally and transverse to the fiber axial direction. The hybrid composite had a global CNT content of 4.95 wt% and exhibited good overall quality. The interply hybrid structure was clearly observed in the hybrid composites. Both carbon fiber and buckypaper layers were fully impregnated with resin. The buckypaper layers were laminated between adjacent carbon fiber layers without observable resin rich areas.

Figure 47 also displays a high quality BP/CF fabric-1 hybrid composite. A wave structure of the buckypaper could be seen as it conformed to the surface texture of the adjacent carbon fabric woven structure. An interesting phenomenon was found that the impregnated buckypaper layer showed an average thickness of  $25 \pm 2 \mu\text{m}$ , which was double the  $1015 \mu\text{m}$  thickness of the dry pristine buckypaper. For both unidirectional and fabric layups, the measured thicknesses of the cured buckypaper layers within the hybrid structures were very consistent. This suggests that the buckypaper swelled during resin impregnation, as previously discussed, acting like a carbon nanotube sponge<sup>132,133</sup> to absorb and hold the resin molecules. This is most likely due to the nanoscale porous structure and large surface area of the carbon nanotube network.



(a)



(b)

Figure 46. Cross-section morphologies of BP/UD-CF-1 interply hybrid composites using prepreg buckypaper in (a) fiber axial and (b) transverse directions

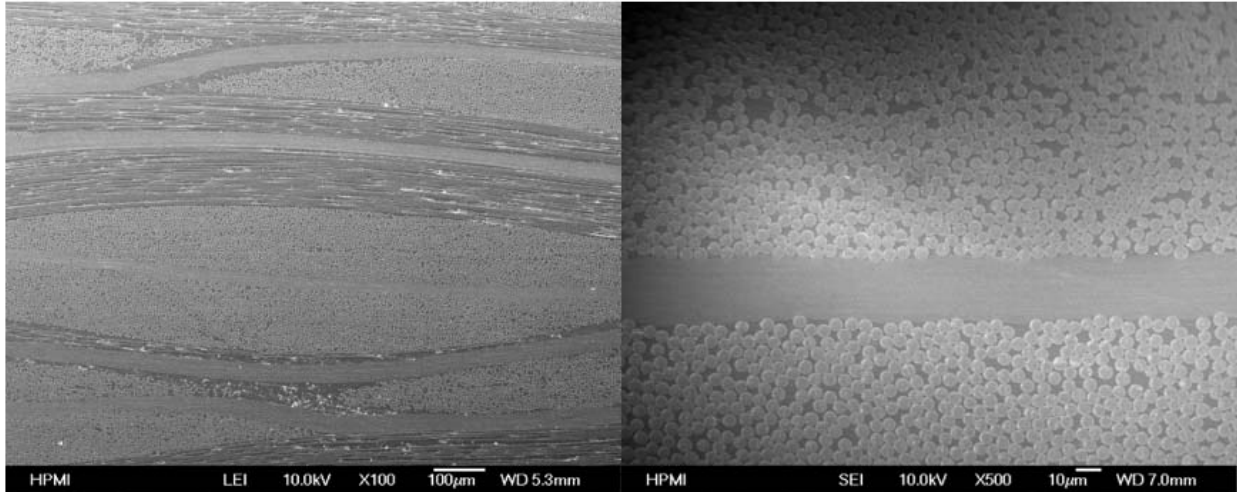
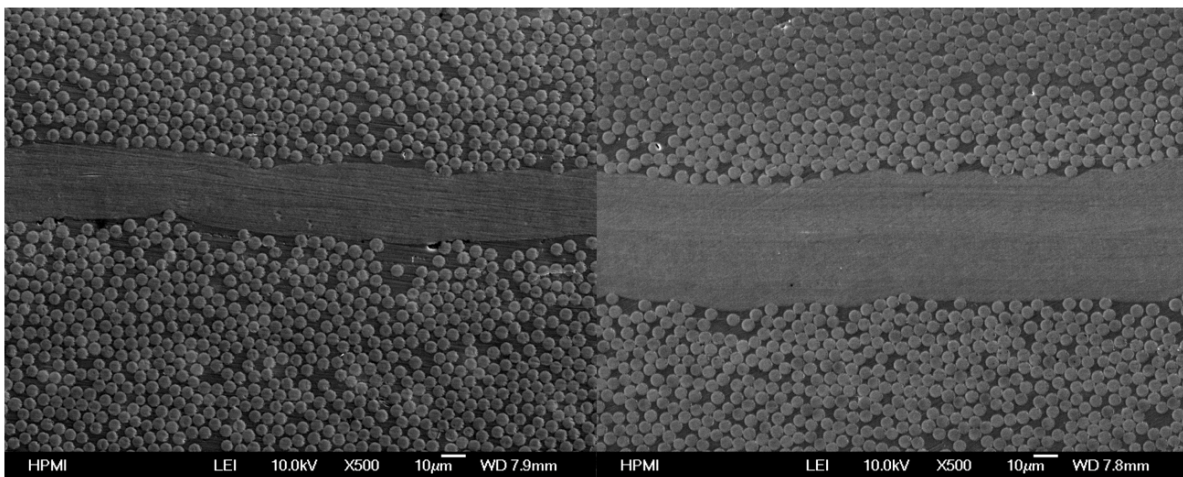


Figure 47. Cross-section morphologies of BP/CF fabric-1 interply hybrid composite using dry buckypaper

Figure 48 compares the cross-section morphologies of the hybrid composites BP/UD-CF-1 with 4.95 wt% and BP/UD-CF-2 with 7.99 wt% global CNT content. The stacking sequences of BP/UD-CF-1 and BP/UD-CF-2 were [BP/CF/BP/CF/BP/CF/BP/CF/BP/CF/BP] and [BP2/CF/BP2/CF/BP2/CF/BP2/CF/BP2/CF/BP2], respectively. The BP/UD-CF-2 sample exhibited a buckypaper thickness of  $50 \pm 3 \mu\text{m}$ , which was approximately twice the thickness of the single-layer buckypaper in the BP/UD-CF-1 sample, showing consistent resin absorbency and swelling properties of the buckypaper.



(a)

(b)

Figure 48. Cross-section morphology of hybrid composites: (a) BP/UD-CF-1 with a global CNT content of 4.95 wt% and (b) BP/UD-CF-2 with a global CNT content of 7.99 wt %.

The hybrid composite possessed a higher global matrix content than the control samples for both unidirectional and fabric reinforced composites cases. For instance, BP/UD-CF-1 hybrid

composite had a global resin content of 38.76 wt%, which was greater than the 33.54 wt% of the control sample. This difference was due to the high absorbency and swelling of buckypaper material, which allowed the hybrid structure to retain more resin than the control samples reinforced by carbon fiber alone. The low permeability of buckypaper layers also largely reduced the resin bleeding during the process, leading to high resin content in the hybrid composites. With the doubling of buckypaper layers in BP/UD-CF-2, we increased CNT content and also increased the resin content in the final hybrid composite. The global resin content of the BP/UD-CF-2 sample rose to 46.55 wt%. Both control and hybrid composites showed similar fiber volume fractions in the carbon fiber plies, which were approximately 60 vol.%. The local CNT volume fractions in buckypaper plies were decided by its resin absorbent capacity, which were about 30 vol.% for the experimental buckypaper.

#### ***4.10 Tensile Properties and Failure Modes of CNT BP/CF Hybrid Composites***

Figure 49 shows the typical stress-strain curves of the BP/UD-CF hybrid composites, the BP/CF fabric hybrid composites and the corresponding CF control and buckypaper composites. Buckypaper composites were reinforced by buckypaper alone as an additional control sample. For the buckypaper control sample, the buckypaper was first dipped into BMI5250-4/acetone solution, and then acetone was vaporized in a vacuum oven at 80 °C. The buckypaper composite was cured following the same schedule as buckypaper prepreg lay-up process. The control unidirectional samples showed a linear elastic behavior until the stress reached their maximum or peak load. Before reaching the peak load, an audible cracking sound was heard due to the crack growth. Once the peak load was reached, the sample failed via brittle fractures. Buckypaper composites solely reinforced by randomly oriented buckypaper with a CNT volume fraction of 35.7 vol.% exhibited a different stress-strain profile, as shown in Figure 49. As the strain increased, the stress-strain curve deviated from the linear proportionality, and the material reacted plastically. This is likely caused by CNT re-orientation under tensile loading and slippage at the CNT and resin interface.<sup>7</sup> The random buckypaper composite showed lower mechanical properties due to the lack of alignment and their weak interface strength with the resin matrix. After hybridizing buckypaper with unidirectional carbon fiber, the resultant composites exhibited a typical hybrid effect to have the properties between the buckypaper composite and CF control sample. Table 10 shows the tensile strength and modulus. BP/UD-CF-1 sample with a global CNT content of 4.95 wt% had excellent tensile strength and modulus of 2519±101 MPa and 149±18 GPa, respectively, which were very close to the control samples with 2626±187 MPa and 159±24 GPa values. The random CNT buckypaper composite sample had tensile strength and modulus of 331±25 MPa and 18±2 GPa. Godara also reported a much larger decrease in tensile behavior of CNT/UD laminates in the fiber direction. The reported UD-laminate was prepared by using epoxy resin mixed with a global CNT content of 0.5 wt%, and a decrease of tensile strength of up to 20% was observed. The strength decrease was explained by the stiffening effect of CNTs on matrix.<sup>134</sup> Different from the UD-laminate with homogeneously

dispersed CNTs, the fracture of interply hybrid composite initiated from the interface between CF and buckypaper plies.

The CF fabric control composite had a tensile strength and modulus of  $960\pm 27$  MPa and  $78\pm 4$  GPa, respectively. Its hybrid sample stress-strain curve shifted slightly toward the larger strain at the tensile stress around 700 MPa, as shown in Figure 49. This was likely due to initiation of delamination between carbon fabric and buckypaper layers. This hybrid composite showed strength and modulus of  $929\pm 31$  MPa and  $71\pm 5$  GPa, which was also close to the corresponding control sample. Figure 50 shows the failure modes of the BP/CF fabric hybrid composite and corresponding control samples. The failure of the hybrid composite (Figure 50a) showed cross-sectional expansion, which was accompanied by a cracking sound, likely related to delamination between buckypaper and carbon fiber layers. In contrast, the thickness of the fabric control sample (Figure 50b) did not show any visible change prior to fracture, and a typical localized lateral brittle fracture of the specimen was observed.

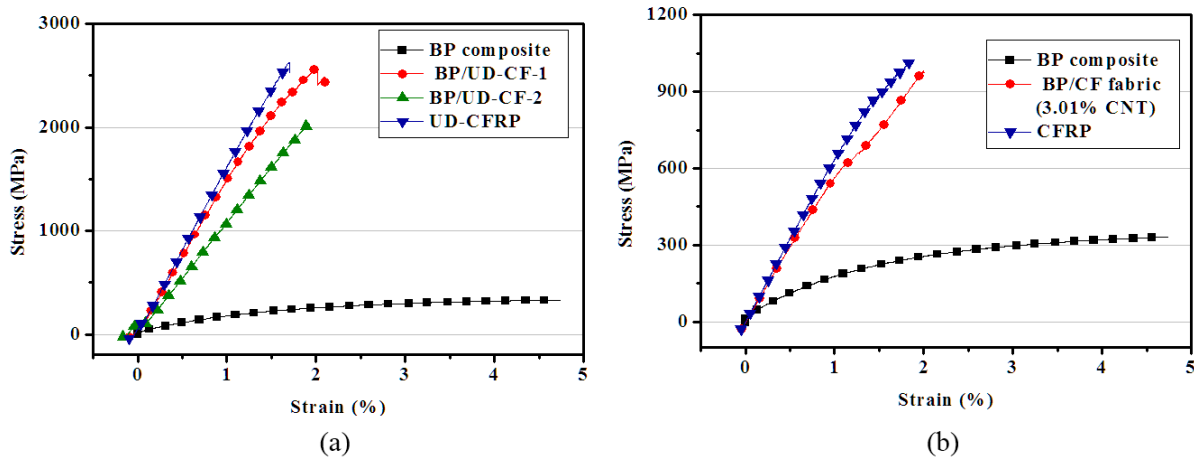


Figure 49. Typical tensile stress-strain curves of (a) BP/UD-CF and (b) BP/CF fabric, as well as buckypaper and carbon fiber control samples

Table 10. Tensile performances of BP/CF hybrid composites and corresponding control samples

Sample	Global CNT content (wt%)	Tensile strength (MPa)	Tensile modulus (GPa)
BP/UD-CF-1	4.95	$2519\pm 101$	$149\pm 18$
BP/UD-CF-2	7.99	$1966\pm 94$	$109\pm 9$
UD-CFRP (Control)	0	$2626\pm 187$	$159\pm 24$
BP/PW-CF-1	3.02	$929\pm 31$	$71\pm 5$
PW-CFRP (Control)	0	$960\pm 27$	$78\pm 4$
BP composite (Control)	40.98	$331\pm 25$	$18\pm 2$

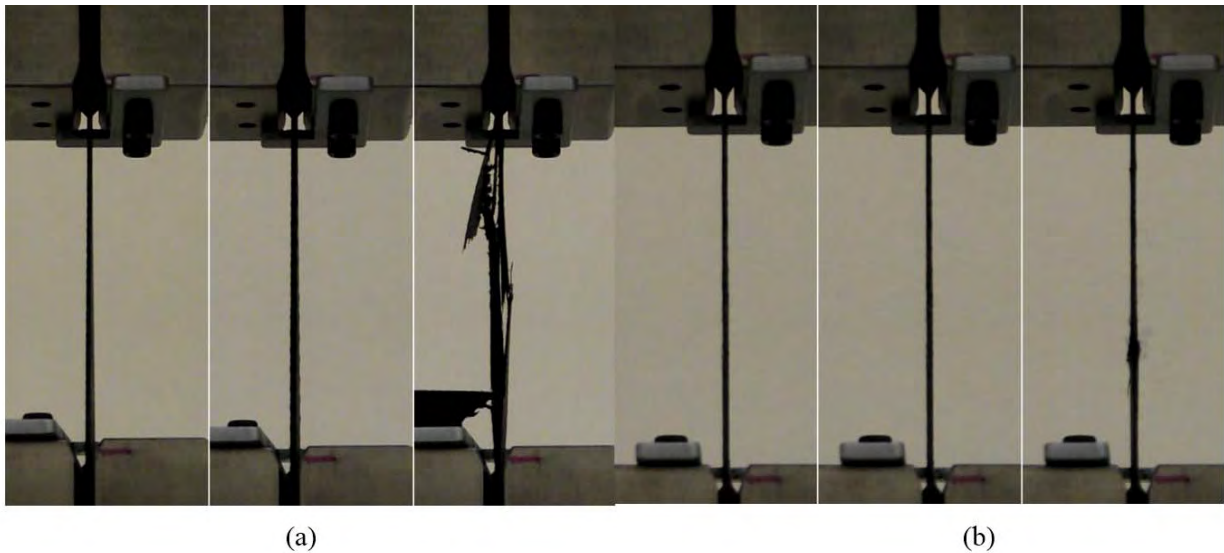


Figure 50. Comparison of failure process and modes: (a) BP/CF fabric hybrid composite and (b) CF fabric control sample

Figure 51 displays the failure modes of the unidirectional and fabric reinforced composites control samples. Figure 51(c) depicts the explosive failure mode of the unidirectional control sample, as described by tensile test failure code XGM, according to ASTM D3039. In contrast, delamination was the predominant failure mode for BP/UD-CF hybrid composites with fragmentation of the specimens, as shown in Figure 51(a) and (b), which were consistent with the failure code DGM. The sizes of the broken pieces were larger with the increasing CNT content, indicating an easier crack propagation for the high CNT content specimens. For the BP/CF fabric composites, the laminates delaminated and fractured in multiple locations, as shown in Figure 51(d). A DGM failure mode was observed. The CF fabric control composite samples failed as a LGM mode. The failure modes of hybrid composites suggest that improvement of interfacial bonding of BP materials is essential in future studies.

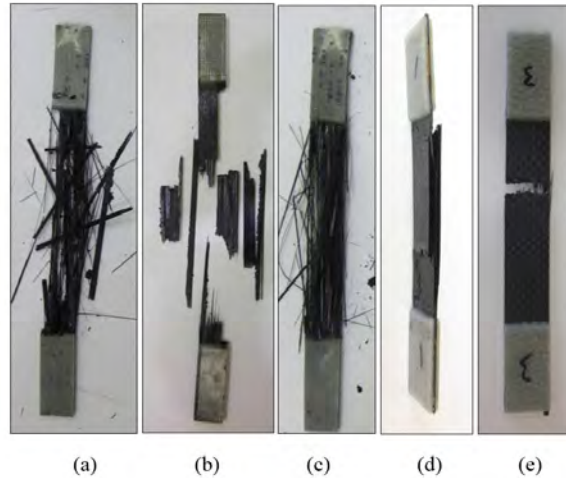


Figure 51. Typical specimen failure modes of (a) BP/UD-CF-1 with a global CNT content of 4.95 wt%, (b) BP/UD-CF-2 with a global CNT content of 7.99 wt%, (c) UD-CFRP control, (d) BP/CF fabric-1 with a global CNT content of 3.01 wt%, and (e) CF fabric control

The tensile modulus of hybrid composites was estimated by using a rule of mixtures.

$$E_{Hybrid} = E_{CF}V_{CF} + E_{BP}V_{BP} \quad (21)$$

where  $E_{CF}$  and  $E_{BP}$  are the moduli of the carbon fiber and buckypaper layers in composites, respectively.  $V_{CF}$  and  $V_{BP}$  are the volume fractions of carbon fiber and buckypaper layers. For the BP/UD-CF-1 sample, the thicknesses of the carbon fiber and buckypaper layers were measured by examining SEM images as  $126 \pm 6 \mu\text{m}$  and  $25 \pm 2 \mu\text{m}$ , respectively. The ratio of  $V_{CF}$  and  $V_{BP}$  was approximately 5:1. By substituting the moduli of the buckypaper and carbon fiber control samples, the predicted hybrid composite modulus was calculated as 135.5 GPa, based on Eq. (22), which was in the 10% variation range of experimental results of  $149 \pm 18 \text{GPa}$ .

To further improve interfacial bonding property of CNT/BMI in the hybrid composites, we further functionalized CNT buckypapers to make F-BP/UD-CF-1 samples. Figure 52 shows the tensile results indicating that with functionalization,<sup>17</sup> we can further improve the mechanical properties of the hybrid samples. The functionalized hybrids show not only the comparable tensile properties compared to the control of CF and corresponding hybrid laminates, but also early 100% increase of failure strain.

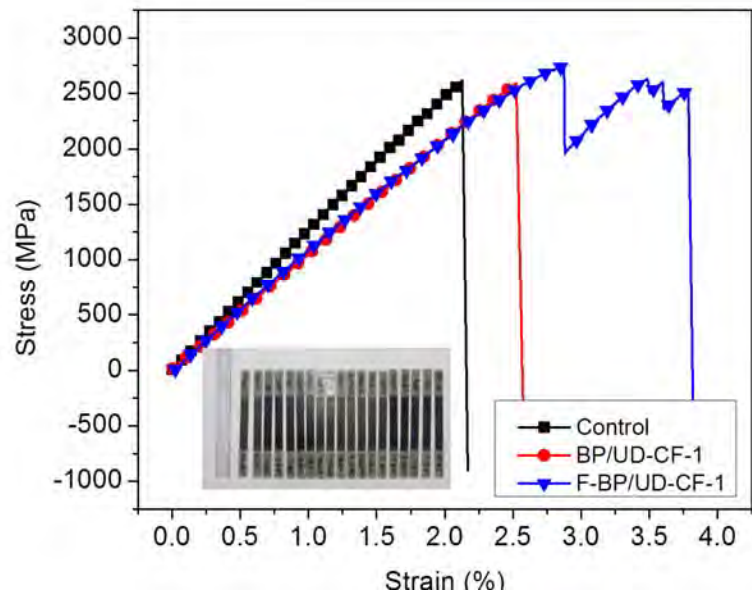


Figure 52. Substantial increase of functionalized buckypaper/CF hybrid composites

Figure 53 shows that the functionalized CNT layers acted as effective toughening media to arrest microcracks in the hybrid composites to improve the failure strain.

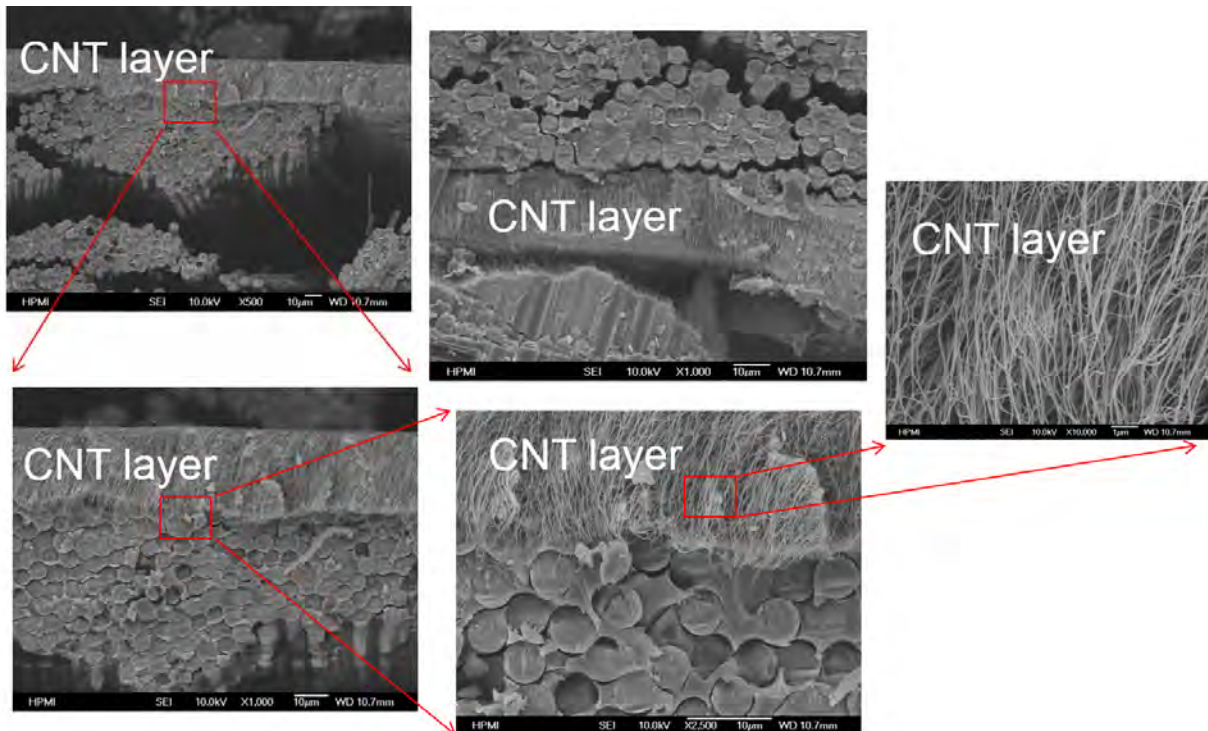


Figure 53. Functionalized CNT buckypaper layers as effective toughening media to arrest microcracks in the hybrid composites

#### 4.11 High Electrical Conductivity of CNT BP/CF Hybrid Composites

Table 11 shows the electrical conductivities of BP/CF hybrid and control composite samples. The in-plane electrical conductivity in UD-CF axial direction of control sample was 93.5 S/cm. After applying 4.95 wt% CNTs, the electrical conductivity of BP/UD-CF-1 increased to 258.4 S/cm. BP/UD-CF-2 showed an electrical conductivity of 306.8 S/cm with a higher global CNT content of 7.99 wt%. The enhancement of electrical conductivity resulted from the superior electrical conductivity of neat buckypaper, which was measured as approximately 855 S/cm. Fiber transverse direction and out-of-plane electrical conductivities of the hybrid composites showed even better improvements, which benefitted from both high electrical conductivity of buckypaper and its bridging effect to the adjacent carbon fibers. The BP/CF fabric composite showed the same tendency as unidirectional composites. In general, the electrical property improvements in BP/UD-CF hybrid composites were much better than that of CF fabric case. That can be explained by their microstructure differences. For the UD-CF cases, the buckypaper layers effectively eliminated resin rich layers in the hybrids compared to the control samples. However, for CF fabric samples, the bridging effects of the buckypaper layer were not so significant since the carbon fabrics had much better contacts compared to the UD fiber case.

Table 11. Electrical conductivities of BP/CF hybrid and control composite samples

Sample	In-plane electrical conductivity (S/cm)		Out-of-plane electrical conductivity (S/cm)
	Axial direction	Transverse direction	
UD-CFRP (control)	93.5	0.13	0.04
BP/UD-CF-1	258.4	45.7	0.18
BP/UD-CF-2	306.8	54.6	0.21
CF fabric (control)	61.4	51.7	0.23
BP/CF fabric-1	94.3	71.9	0.29

### 5. Multiscale Model and Simulation of Buckypaper and Nanocomposites

Integrated computational and experimental engineering (ICEE) is a powerful tool for developing new materials, especially for nanomaterials with high raw material costs. The development of high-performance carbon nanotube (CNT) supramolecular structures and CNT/carbon fiber (CF) composites uses ICEE to guide property prediction of the final product. This new material by nature has a multiscale structure with CNTs at nanoscale, CFs at microscale and composites at macroscale. It is difficult, if not impossible, to build a unified model for property prediction from information lying at all scales. The Georgia Institute of Technology (GT) team designed a

hierarchical modeling strategy for this new material development, as shown in Figure 54. The main components include MD simulation, coarse-grained MD modeling, finite element analysis (FEA), statistical surrogate modeling, and Bayesian based or latent variable based model calibration and adjustment. The result is a hybrid physics-statistics model that predicts mechanical properties of the supramolecular CNT/CF composites. Here we reported the major progress in coarse-grained MD modeling and finite element analysis (FEA) of CNT network and alignment properties.

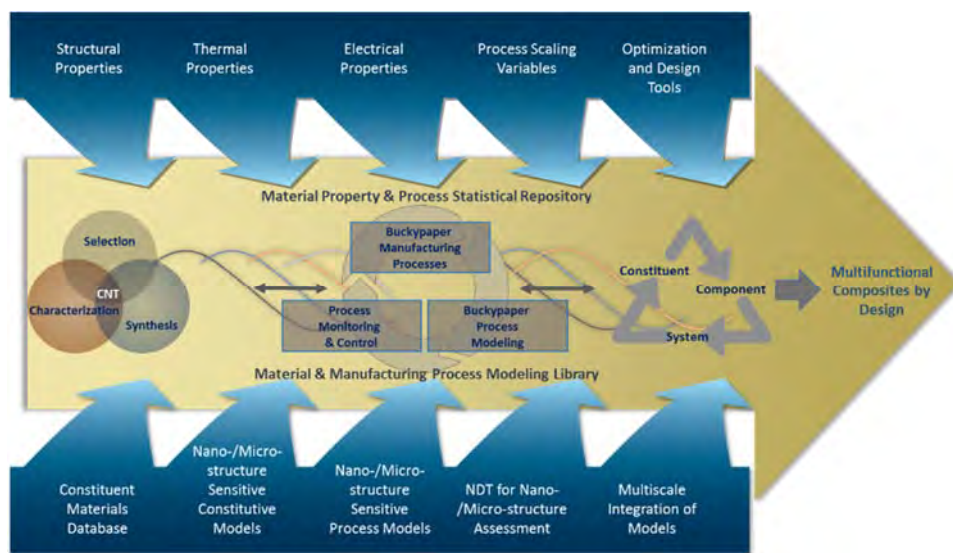


Figure 54. Integrated Computational and Experimental Engineering (ICEE) for multifunctional nanocomposite development

### 5.1 Coarse-grained MD Model of CNT Network Structures in Buckypaper

Our research team studied coarse-grained MD model and simulation of CNT network structures of buckypaper materials. The buckypapers consist of packed CNT bundles entangled with one another, held together, and arranged as a planer film through van der Waals forces.<sup>135</sup> They usually form a highly porous network structure with a random arrangement of CNTs cross-linked by weak intertube interactions.<sup>136</sup> As a result, a significant change in the topology/microstructure of a CNT network could result when the buckypapers are loaded mechanically, such as reorienting, bending, building or buckling the CNTs,<sup>132,136–138</sup> which would be expected to modulate the macroscopic properties. An in-depth understanding of the relations between the microstructures and mechanical properties of CNTs is needed before the potential of CNT buckypaper can be realized for engineering applications. MD simulations, more specifically large scale coarse-grained molecular dynamics (CGMD) simulations technique, were used to model and investigate the mechanical properties of CNT buckypaper.

The longer CNTs in buckypaper requires the representative volume element (RVE) for computational simulation to be mesoscopic. The resulting huge number of atoms and the large range of van der Waals (vdW) interactions between CNTs make a full atomistic simulation

impossible. Furthermore, the complexity of the CNT network in the buckypaper makes continuum modeling difficult.<sup>139</sup> Therefore, the CGMD simulations technique was adopted since it is based on the bead-spring model for CNTs.<sup>139–141</sup> The discrete bead interaction through bond and bond angle springs provide a description equivalent to a continuum mechanics model with specific tension stiffness and bending rigidity.

For our CGMD simulations, we modeled the cylindrical atomic structure of CNT into a multi-bead chain model, as shown in Figure 55. To do this, a full atomistic CNT was discretized into multiple beads with a concentrated mass and mutually connected through springs. This simplification greatly reduced the total number of degrees of freedom for modeled buckypaper and allowed us to take into account long-range vdW interactions between CNTs. The total energy of the multi-bead chain system is given by:<sup>142</sup>

$$E_{\text{system}} = E_T + E_B + E_{\text{pairs}} \quad (22)$$

Where  $E_T = k_T(b-b_0)^2/2$  is the energy stored in the chemical bonds due to axial stretching, where  $k_T = YA/b_0$  is the spring constant relating to the tension stiffness,  $Y$  is the Young's modulus of the carbon nanotube,  $A$  is the cross section area and  $b$  is the distance between two bonding beads with  $b_0=1$  nm as its equilibrium distance.  $E_B = k_B(\theta-\theta_0)^2/2$  is the bending of adjacent bead triplets, where  $k_B = 2YI/b_0$  is the angular spring constant relating to the bending stiffness  $D=YI$ ;  $\theta$  is the bending angle within the triplet;  $\theta_0$  is the equilibrium angle; and  $I$  is the bending moment of inertia.  $E_{\text{pairs}} = 4\varepsilon[(\sigma/r)^{12} - (\sigma/r)^6]$  is the energy due to weak van der Waals interactions between all pairs of non-bonded beads, separated by a distance  $r$ .  $\varepsilon$  and  $\sigma$  represent the energy depth and equilibrium distance at vdW equilibrium, respectively. The six parameters,  $k_T$ ,  $k_B$ ,  $b_0$ ,  $\theta_0$ ,  $\varepsilon$  and  $\sigma$  that define the multi-bead chain model can be obtained from a series of full atomistic simulations of CNTs via equilibrium conditions ( $b_0$ ,  $\theta_0$  and  $\sigma$ ) and energy conservation conditions ( $k_T$ ,  $k_B$  and  $\varepsilon$ ), i.e., tension, bending and adhesion tests of CNTs, respectively, following a “fine-trains-coarse” approach.<sup>141,143</sup>

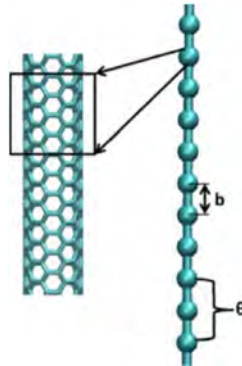


Figure 55. The bead-spring model for CNT<sup>140</sup>

The model parameters derived in<sup>141</sup> for (5,5) SWCNT was based on the full atomistic calculation of CNTs are used in our simulation, as listed in Table 12.

Table 12. Parameters of the mesoscopic bead-spring model of (5, 5) SWCNT<sup>142</sup>

Parameters	Units	(5, 5) SWCNT
$k_{bond}$	Kcal mol <sup>-1</sup> Å <sup>-2</sup>	1000
$r_0$	Å	100
$k_{bend}$	Kcal mol <sup>-1</sup> rad <sup>-2</sup>	180
$\theta_0$	Degree	14300
$\epsilon$	Kcal mol <sup>-1</sup>	15.10
$\sigma$	Å	9.35

Figure 56a illustrates the structure of our coarse-grained model CNT buckypaper. Self-avoid random walk was used to generate the initial configuration of RVE of the CNT network in buckypaper. Then the RVE was relaxed using a combined molecular dynamics/Monte Carlo method, bond swap algorithm (BSA), to reach the minimum energy state under room temperature and atmosphere, which were the initial conditions for MD simulations of stress-strain tests. To make the initial configuration generated by random walk as close to the relaxed state as possible, the walk path of each CNT was constructed as follows:

- Choose a random starting point within the RVE. The dimensions of the RVE are user specified. In this study, the dimensions used are: 200 (L) × 200 (W) × 20 (H) nm<sup>3</sup>.
- Use spherical coordinates to define the walking direction (1,  $\theta$ ,  $\varphi$ ).
- Choose a random walking direction to move to the second point: theta ( $\theta$ ) is defined to obey normal distribution on the range  $[0, \pi]$ ,  $\theta = \pi/2 + ((\pi/4)/1.6) * \text{randn}$  &  $0 \leq \theta \leq \pi$ , with the mean to be  $\pi/2$  and the probability falling in  $[\pi/4, 3\pi/4]$  to be 90%, in order to make sure the CNT is more aligned in x-y plane; the moving direction in x-y plane is defined by  $\varphi$ , a random variable uniformly defined in  $[0, 2\pi]$ .
- From 3rd points onward, the movement in the z-direction is similar as that defined in step c) with  $\theta$ ; the moving direction in x-y plane is defined such that it will not deviate too much from the previous walk path (because the equilibrium angle between bead-bead bonds is 180°), which is achieved by  $\varphi = \text{dir}\varphi + ((\pi/6)/1.6) * \text{randn}$ : the mean is the  $\varphi$  of previous path, probability of deviating  $\pm 60^\circ$  is 90%.
- Re-choose the path if the point-to-move-to has already been occupied by existing points or exceeds the RVE range.

The process was repeated until the desired number of CNTs was achieved. The RVE of buckypaper was set to be 200×200×20 nm<sup>3</sup> and contained 80 (5, 5) SWCNT at a length of 500

nm. Figure 56 shows representative RVEs of CNT buckypaper composites that were generated following the steps above.

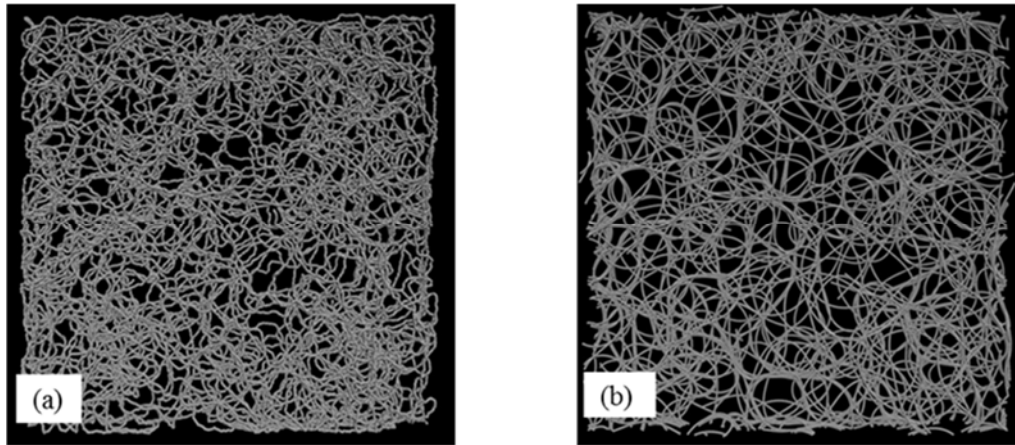


Figure 55. CNT configurations in buckypaper (a) before energy minimization (b) after 64-picoseconds relaxation

However, the initial configuration generated in this way was far from being in a state of equilibrium and the initial relaxation for a minimum energy state took a long time. A three-hour calculation on a four-core computer, which was equivalent to 64-picoseconds in real time, showed no sign of equilibrium, although the total potential energy of the whole system decreased to about 92,500 Kcal/mole (Figure 56b) from the initial value with an order of 1,018 Kcal/mole (Figure 56a). The right image gave a better representation of buckypaper with a smoother orientation of CNTs. The established model can be used for further analysis of structure-property relationships of CNT networks.

### ***5.2 FEA for Modeling CNT Network Structure Change and Alignment Properties***

As most inputs for the FEA model are directly measured from SEM images of buckypaper, the first task is to enhance the image analysis for a more accurate nanostructure characterization. The properties of the CNT sheet are determined by its nanostructure characteristics, such as lengths, diameters, orientations of CNTs, and how they interconnect with each other. However, direct measurement from SEM images of CNT sheet is difficult<sup>144,145</sup> due to its multilayer nature (Figure 57). In order to extract accurate characteristics of CNTs, the SEM images need to be processed and analyzed using image enhancement tools.

The GT team has developed an algorithm to handle this particular problem. The algorithm captures the boundaries of CNTs in the image. Then it removes the noise from the lower layer and repairs the nanotubes on the top layer. The resulting image shows greater contraction between top layer nanotubes and lower layer noises, as shown in Figure 58.

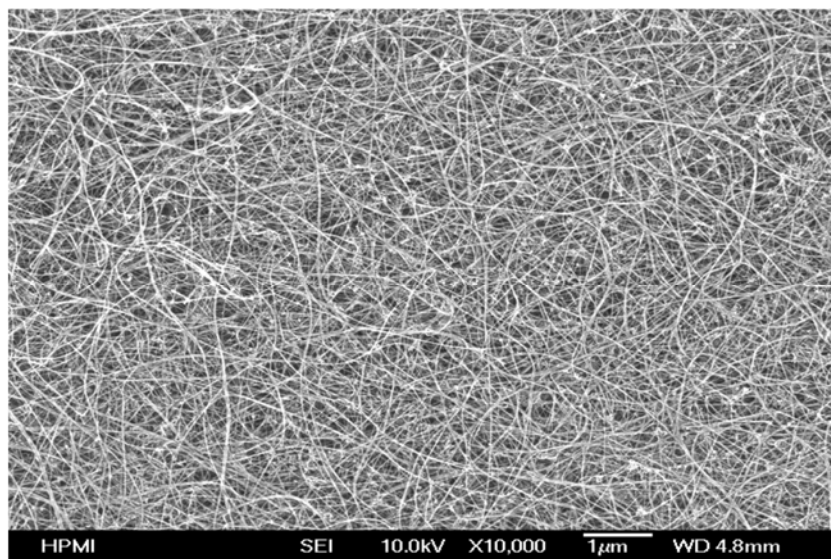


Figure 57. Typical SEM image of CNT sheet

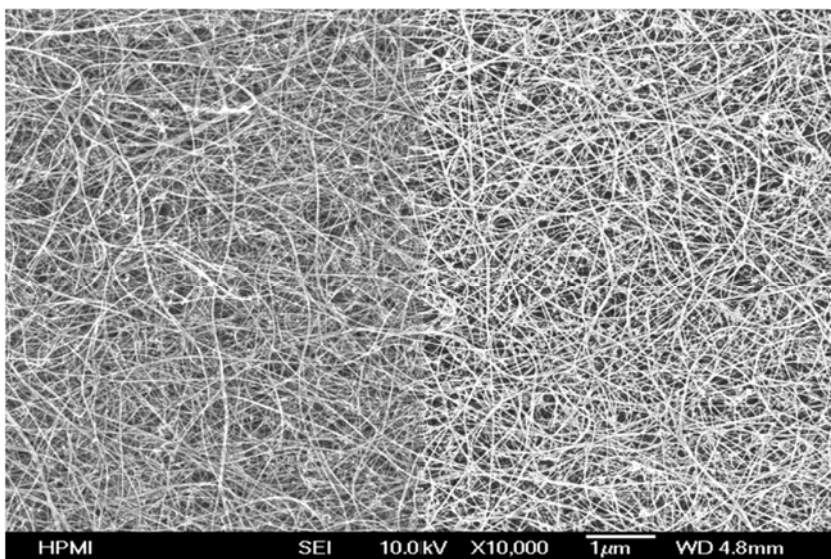


Figure 58. A comparison between original image (left) and processed image. A comparison between original image (left) and processed image (right). The brightness and sharpness of top layer CNTs are enhanced, providing a more distinguishable input for the analysis software

SIMAGIS, an advanced image analysis software, was used to extract the nanostructure information from the SEM images. We compared the analysis results from both the original image and the processed image to the manual measurement of 100 CNTs in each SEM image, which is shown in Figure 59. Similarly, the length distribution and orientation distribution were also measured from the SEM images. An example of such characterizations of a random buckypaper is shown in Figure 60.

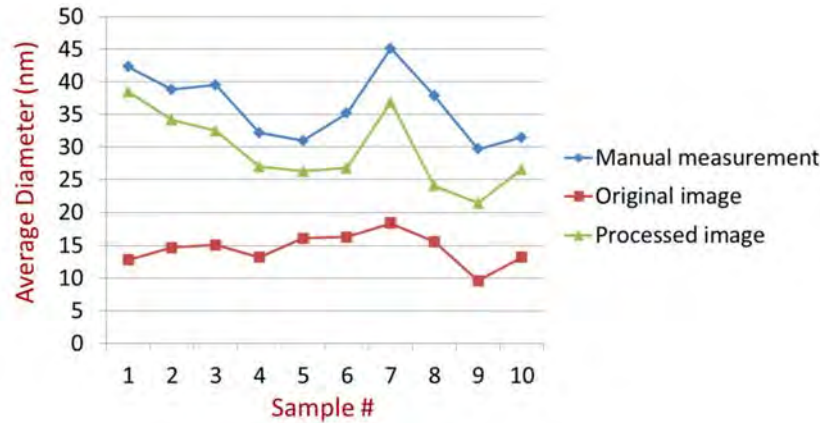


Figure 59. The comparison of diameter measurement results. The results from the processed image not only reduced the discrepancy between manual measurement and software analysis, but also better captured the trend

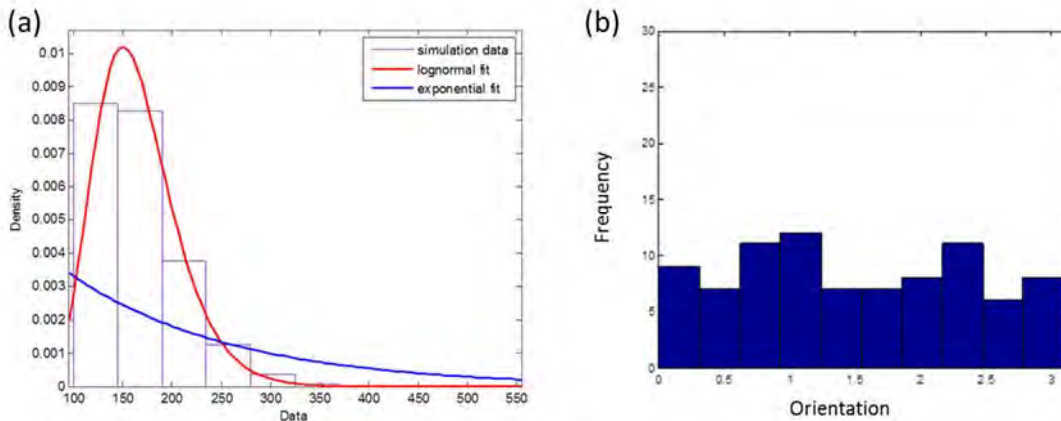


Figure 60. (a) Length measurements and (b) orientation measurements of a random buckypaper

The effective load transferring at the nanotube interconnections in a CNT sheet is the critical mechanism underlying its mechanical properties,<sup>112</sup> In order to provide a strong interaction between the nanotubes, the joints were treated by methods, such as e-beam sintering. Assuming all joints are fixed after the CNTs achieve a supramolecular structure, the mechanical properties of the CNT sheet can be predicted based on its nanostructure. A finite element-based mechanical model for CNT sheets has been developed for this purpose.

The network of CNT in the sheet was viewed as a truss structure.<sup>146</sup> The GT team developed a random network generator, which simulates the CNT network in the sheet confined in a 1  $\mu\text{m}$  by 1  $\mu\text{m}$  control cell. The lengths and distributions of each element were generated from distributions characterized by previous measurement methods from SEM images of CNT sheets. The joints were identified by finding the intersections of elements, as shown in Figure 61. This imaging analysis-based approach is valuable for exploring structure-property relationships of CNT networks.

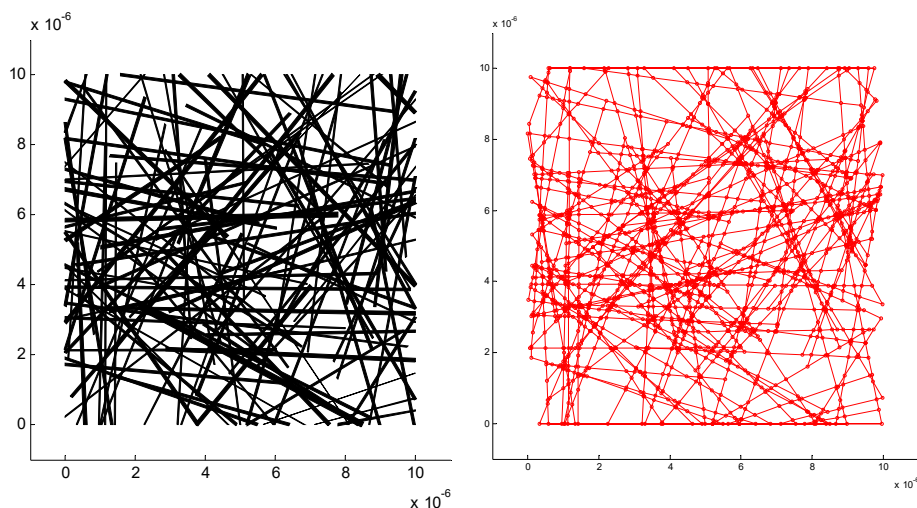


Figure 61. The randomly generated CNT network (left) and the corresponding truss structure (right)

## Conclusions

In this project, we explored two novel low-density material systems to potentially realize the ultimate intrinsic properties of CNTs for scale-up applications: continuous highly aligned CNT tapes or sheets and CNT sheet/carbon fiber hybrid composites (CNT/CF) with aerospace-grade quality and carbon fiber concentration.

We studied different approaches for engineering CNT networks in CNT thin films or buckypaper to achieve high degree of alignment and graphitic crystal packing. With the selection of extra-large aspect ratio ( $>100,000$ ) and small diameter (58 nanometers) double-walled CNT and use of load transfer media in CNT networks, we developed unique mechanical stretching process to realize high degree of alignment and graphitic crystal assembling CNTs to reduce packing defects in macroscopic assemblages of CNTs. We found that the ductility of the network largely relies on the high aspect ratio of millimeter long nanotubes, high waviness and locking points from residual catalyst nanoparticles and use of load transfer media. The original random network has low density, strength and modulus. The effect of uniaxial strain on the CNT network was the nanostructure evolution through multiple deformation modes found by using SEM, Raman and in-situ X-ray analysis. The deformation modes exposed the CNT network strain hardening parameter  $n$  value as high as 0.65, which was much higher than annealed low-carbon steel and typical polymers. The alignment treatment also enhanced the mechanical properties with strength coefficient  $K$  values for the CNT network and show high values up to roughly 450 MPa in the range of annealed magnesium alloys.

The aligned CNT fraction in the resultant materials can be as high as 0.93, close to that of carbon fiber materials. We discovered that the unique geometrically constrained self-assembly and graphitic crystal packing of flattened and aligned CNT can lead to intimately surface contact of CNTs to substantially improve load transfer and mechanical properties. The failure modes and

mechanisms at different scales were studied by SEM and TEM analysis. The microstructure analysis by SEM showed evidence of failure due to nanotube bundle telescoping, interlayer separation, and bundle pullout and folding, resulting from relatively weak CNT/CNT and CNT/resin interactions. The CNTs in bundles were collapsed and preferred to form surface-to-surface stacking and shoulder-to-shoulder assemblies. MD simulations of 8 nm diameter nanotubes predicted a density of 0.665 and 1.820 g/cm<sup>3</sup> for round and flattened nanotubes respectively. Comparing predicted densities to the measured densities indicates that the samples are highly dense, with a very low void volume fraction and a large percentage of flattened CNTs. This novel geometrically constrained self-assembly and packing of flattened and aligned CNTs has the potential to realize microstructures with the long-range order, low defect density, and ordered crystalline CNT packing that are thought to be essential for fully translating CNT mechanical properties into composite materials.

We also revealed that extremely low permeability ( $\times 10^{-17\sim 19}$  m<sup>2</sup>) of CNT thin film or buckypaper materials could largely eliminate through-thickness flow of resin matrix during composite autoclave fabrication process. Modification of processing parameters and consideration of strong capillary resin absorption of CNT networks during CNT buckypaper/CF prepreg materials for hybrid composites are needed to fabricate aerospace-grade hybrid composites with 5–8 wt.% CNT and 50–60 vol.% carbon fiber concentrations. The composites with CNT/CF alternative interply hybridization demonstrated promising mechanical/electrical multifunctional features. The strong CNT layers also acted as effective microcrack arresting layers to potentially improve damage tolerance properties. The project results provide a new fundamental understanding for scale-up for CNT applications in lightweight and multifunctional composites and structures. The multiscale model and simulation of CNT and buckypaper-based materials were also explored. The new fundamental understanding of highly aligned and graphitic crystal pack of flattened CNTs and toughening effect of interply CNT layers in buckypaper/CF hybrid composites are valuable for developing future low density and multifunctional composite systems.

## **Acknowledgement**

This project was supported by AFOSR. The sponsorship and oversight of this program by Dr. Joycelyn Harrison from AFOSR is greatly appreciated. Cytec Engineered Materials is also thanked for their funding and partnership. We would like to thank Boeing, Nanocomp Technologies support and The TEM facility at FSU, which is funded and supported by the Florida State University Research Foundation, and the National High Magnetic Field Laboratory, which was supported in part by the National Science Foundation Cooperative Agreement DMR-1157490, the State of Florida, and Florida State University.

We also would like to thank the participation and contributions from Dr. Chuck Zhang from (Georgia Tech), Dr. JinGyn Park and Dr. Ayoun Hao, and Mr. Frank Allen from FSU. We would like to thank to all students and postdocs participated and supported the project.

## REFERENCES

- (1) Yu, M.-F.; Lourie, O.; Dyer, M. J.; Moloni, K.; Kelly, T. F.; Ruoff, R. S. Strength and Breaking Mechanism of Multiwalled Carbon Nanotubes Under Tensile Load. *Science* **2000**, *287* (5453), 637–640.
- (2) Schultz, J. M. *Polymer Materials Science*; Prentice hall, 1974.
- (3) Bower, C.; Zhu, W.; Jin, S.; Zhou, O. Plasma-Induced Alignment of Carbon Nanotubes. *Appl. Phys. Lett.* **2000**, *77* (6), 830–832.
- (4) Zhang, M.; Atkinson, K. R.; Baughman, R. H. Multifunctional Carbon Nanotube Yarns by Downsizing an Ancient Technology. *Science* **2004**, *306* (5700), 1358–1361.
- (5) Feng, W.; Bai, X. D.; Lian, Y. Q.; Liang, J.; Wang, X. G.; Yoshino, K. Well-Aligned Polyaniline/carbon-Nanotube Composite Films Grown by in-Situ Aniline Polymerization. *Carbon* **2003**, *41* (8), 1551–1557.
- (6) Wang, D.; Song, P.; Liu, C.; Wu, W.; Fan, S. Highly Oriented Carbon Nanotube Papers Made of Aligned Carbon Nanotubes. *Nanotechnology* **2008**, *19* (7), 075609.
- (7) Cheng, Q.; Bao, J.; Park, J.; Liang, Z.; Zhang, C.; Wang, B. High Mechanical Performance Composite Conductor: Multi-Walled Carbon Nanotube Sheet/Bismaleimide Nanocomposites. *Adv. Funct. Mater.* **2009**, *19* (20), 3219–3225.
- (8) Ruan, S. L.; Gao, P.; Yang, X. G.; Yu, T. X. Toughening High Performance Ultrahigh Molecular Weight Polyethylene Using Multiwalled Carbon Nanotubes. *Polymer* **2003**, *44* (19), 5643–5654.
- (9) Koziol, K.; Vilatela, J.; Moisala, A.; Motta, M.; Cunniff, P.; Sennett, M.; Windle, A. High-Performance Carbon Nanotube Fiber. *Science* **2007**, *318* (5858), 1892–1895.
- (10) Berber, S.; Kwon, Y.-K.; Tománek, D. Unusually High Thermal Conductivity of Carbon Nanotubes. *Phys. Rev. Lett.* **2000**, *84* (20), 4613–4616.
- (11) Xie, X.-L.; Mai, Y.-W.; Zhou, X.-P. Dispersion and Alignment of Carbon Nanotubes in Polymer Matrix: A Review. *Mater. Sci. Eng. R Rep.* **2005**, *49* (4), 89–112.
- (12) Thostenson, E. T.; Li, C.; Chou, T.-W. Nanocomposites in Context. *Compos. Sci. Technol.* **2005**, *65* (3–4), 491–516.
- (13) Chou, T.-W.; Gao, L.; Thostenson, E. T.; Zhang, Z.; Byun, J.-H. An Assessment of the Science and Technology of Carbon Nanotube-Based Fibers and Composites. *Compos. Sci. Technol.* **2010**, *70* (1), 1–19.
- (14) Iakoubovskii, K. Techniques of Aligning Carbon Nanotubes. *Open Phys.* **2009**, *7* (4), 645–653.
- (15) Park, J. G.; Smithyman, J.; Lin, C.-Y.; Cooke, A.; Kismarhardja, A. W.; Li, S.; Liang, R.; Brooks, J. S.; Zhang, C.; Wang, B. Effects of Surfactants and Alignment on the Physical Properties of Single-Walled Carbon Nanotube Buckypaper. *J. Appl. Phys.* **2009**, *106* (10), 104310.
- (16) Bao, J. W.; Cheng, Q. F.; Wang, X. P.; Liang, Z. Y.; Wang, B.; Zhang, C.; Kramer, L.; Funchess, P.; Dorrough, D. Mechanical Properties of Functionalized Nanotube Buckypaper Composites. In *17th International Conference on Composite Materials*; 2009.
- (17) Cheng, Q.; Wang, B.; Zhang, C.; Liang, Z. Functionalized Carbon-Nanotube Sheet/Bismaleimide Nanocomposites: Mechanical and Electrical Performance Beyond Carbon-Fiber Composites. *Small* **2010**, *6* (6), 763–767.

- (18) Li, S.; Park, J. G.; Liang, Z.; Siegrist, T.; Liu, T.; Zhang, M.; Cheng, Q.; Wang, B.; Zhang, C. In Situ Characterization of Structural Changes and the Fraction of Aligned Carbon Nanotube Networks Produced by Stretching. *Carbon* **2012**, *50* (10), 3859–3867.
- (19) Zhang, Y.; Iijima, S. Elastic Response of Carbon Nanotube Bundles to Visible Light. *Phys. Rev. Lett.* **1999**, *82* (17), 3472–3475.
- (20) Huang, Z. P.; Xu, J. W.; Ren, Z. F.; Wang, J. H.; Siegal, M. P.; Provencio, P. N. Growth of Highly Oriented Carbon Nanotubes by Plasma-Enhanced Hot Filament Chemical Vapor Deposition. *Appl. Phys. Lett.* **1998**, *73* (26), 3845–3847.
- (21) Ren, Z. F.; Huang, Z. P.; Xu, J. W.; Wang, J. H.; Bush, P.; Siegal, M. P.; Provencio, P. N. Synthesis of Large Arrays of Well-Aligned Carbon Nanotubes on Glass. *Science* **1998**, *282* (5391), 1105–1107.
- (22) Ren, Z. F.; Huang, Z. P.; Wang, D. Z.; Wen, J. G.; Xu, J. W.; Wang, J. H.; Calvet, L. E.; Chen, J.; Klemic, J. F.; Reed, M. A. Growth of a Single Freestanding Multiwall Carbon Nanotube on Each Nanonickel Dot. *Appl. Phys. Lett.* **1999**, *75* (8), 1086–1088.
- (23) Bower, C.; Zhou, O.; Zhu, W.; Werder, D. J.; Jin, S. Nucleation and Growth of Carbon Nanotubes by Microwave Plasma Chemical Vapor Deposition. *Appl. Phys. Lett.* **2000**, *77* (17), 2767–2769.
- (24) Okai, M.; Muneyoshi, T.; Yaguchi, T.; Sasaki, S. Structure of Carbon Nanotubes Grown by Microwave-Plasma-Enhanced Chemical Vapor Deposition. *Appl. Phys. Lett.* **2000**, *77* (21), 3468–3470.
- (25) Aliev, A. E.; Guthy, C.; Zhang, M.; Fang, S.; Zakhidov, A. A.; Fischer, J. E.; Baughman, R. H. Thermal Transport in MWCNT Sheets and Yarns. *Carbon* **2007**, *45* (15), 2880–2888.
- (26) Yamaguchi, M.; Pan, L.; Akita, S.; Nakayama, Y. Effect of Residual Acetylene Gas on Growth of Vertically Aligned Carbon Nanotubes. *Jpn. J. Appl. Phys.* **2008**, *47* (4), 1937–1940.
- (27) Zheng, L.; Sun, G.; Zhan, Z. Tuning Array Morphology for High-Strength Carbon-Nanotube Fibers. *Small* **2010**, *6* (1), 132–137.
- (28) Zhang, L.; Zhang, G.; Liu, C.; Fan, S. High-Density Carbon Nanotube Buckypapers with Superior Transport and Mechanical Properties. *Nano Lett.* **2012**, *12* (9), 4848–4852.
- (29) Li, Y.-L.; Kinloch, I. A.; Windle, A. H. Direct Spinning of Carbon Nanotube Fibers from Chemical Vapor Deposition Synthesis. *Science* **2004**, *304* (5668), 276–278.
- (30) Li, Q. W.; Zhang, X. F.; DePaula, R. F.; Zheng, L. X.; Zhao, Y. H.; Stan, L.; Holesinger, T. G.; Arendt, P. N.; Peterson, D. E.; Zhu, Y. T. Sustained Growth of Ultralong Carbon Nanotube Arrays for Fiber Spinning. *Adv. Mater.-DEERFIELD BEACH THEN Weinh.* **2006**, *18* (23), 3160.
- (31) Zhang, Y.; Zou, G.; Doorn, S. K.; Htoon, H.; Stan, L.; Hawley, M. E.; Sheehan, C. J.; Zhu, Y.; Jia, Q. Tailoring the Morphology of Carbon Nanotube Arrays: From Spinnable Forests to Undulating Foams. *ACS Nano* **2009**, *3* (8), 2157–2162.
- (32) Haggenueller, R.; Gommans, H. H.; Rinzler, A. G.; Fischer, J. E.; Winey, K. I. Aligned Single-Wall Carbon Nanotubes in Composites by Melt Processing Methods. *Chem. Phys. Lett.* **2000**, *330* (3–4), 219–225.
- (33) Bhattacharyya, A. R.; Sreekumar, T. V.; Liu, T.; Kumar, S.; Ericson, L. M.; Hauge, R. H.; Smalley, R. E. Crystallization and Orientation Studies in Polypropylene/single Wall Carbon Nanotube Composite. *Polymer* **2003**, *44* (8), 2373–2377.

- (34) Hone, J.; Llaguno, M. C.; Nemes, N. M.; Johnson, A. T.; Fischer, J. E.; Walters, D. A.; Casavant, M. J.; Schmidt, J.; Smalley, R. E. Electrical and Thermal Transport Properties of Magnetically Aligned Single Wall Carbon Nanotube Films. *Appl. Phys. Lett.* **2000**, *77* (5), 666–668.
- (35) Smith, B. W.; Benes, Z.; Luzzi, D. E.; Fischer, J. E.; Walters, D. A.; Casavant, M. J.; Schmidt, J.; Smalley, R. E. Structural Anisotropy of Magnetically Aligned Single Wall Carbon Nanotube Films. *Appl. Phys. Lett.* **2000**, *77* (5), 663–665.
- (36) Chen, X. Q.; Saito, T.; Yamada, H.; Matsushige, K. Aligning Single-Wall Carbon Nanotubes with an Alternating-Current Electric Field. *Appl. Phys. Lett.* **2001**, *78* (23), 3714–3716.
- (37) Walters, D. A.; Casavant, M. J.; Qin, X. C.; Hu, C. B.; Boul, P. J.; Ericson, L. M.; Haroz, E. H.; Connell, M. J. O.; Smith, K.; Colbert, D. T.; Smalley, R. E. In-Plane-Aligned Membranes of Carbon Nanotubes. **2001**, *338* (April), 14–20.
- (38) Casavant, M. J.; Walters, D. A.; Schmidt, J. J.; Smalley, R. E. Neat Macroscopic Membranes of Aligned Carbon Nanotubes. *J. Appl. Phys.* **2003**, *93* (4), 2153–2156.
- (39) Fischer, J. E.; Zhou, W.; Vavro, J.; Llaguno, M. C.; Guthy, C.; Haggemueller, R.; Casavant, M. J.; Walters, D. E.; Smalley, R. E. Magnetically Aligned Single Wall Carbon Nanotube Films: Preferred Orientation and Anisotropic Transport Properties. *J. Appl. Phys.* **2003**, *93* (4), 2157–2163.
- (40) Kamat, P. V.; Thomas, K. G.; Barazzouk, S.; Girishkumar, G.; Vinodgopal, K.; Meisel, D. Self-Assembled Linear Bundles of Single Wall Carbon Nanotubes and Their Alignment and Deposition as a Film in a Dc Field. *J. Am. Chem. Soc.* **2004**, *126* (34), 10757–10762.
- (41) Bradford, P. D.; Wang, X.; Zhao, H.; Maria, J.-P.; Jia, Q.; Zhu, Y. T. A Novel Approach to Fabricate High Volume Fraction Nanocomposites with Long Aligned Carbon Nanotubes. *Compos. Sci. Technol.* **2010**, *70* (13), 1980–1985.
- (42) Jin, L.; Bower, C.; Zhou, O. Alignment of Carbon Nanotubes in a Polymer Matrix by Mechanical Stretching. *Appl. Phys. Lett.* **1998**, *73* (9), 1197–1199.
- (43) Miaudet, P.; Badaire, S.; Maugey, M.; Derré, A.; Pichot, V.; Launois, P.; Poulin, P.; Zakri, C. Hot-Drawing of Single and Multiwall Carbon Nanotube Fibers for High Toughness and Alignment. *Nano Lett.* **2005**, *5* (11), 2212–2215.
- (44) Wang, X.; Bradford, P. D.; Liu, W.; Zhao, H.; Inoue, Y.; Maria, J.-P.; Li, Q.; Yuan, F.-G.; Zhu, Y. Mechanical and Electrical Property Improvement in CNT/Nylon Composites through Drawing and Stretching. *Compos. Sci. Technol.* **2011**, *71* (14), 1677–1683.
- (45) Wang, X.; Yong, Z. Z.; Li, Q. W.; Bradford, P. D.; Liu, W.; Tucker, D. S.; Cai, W.; Wang, H.; Yuan, F. G.; Zhu, Y. T. Ultrastrong, Stiff and Multifunctional Carbon Nanotube Composites. *Mater. Res. Lett.* **2013**, *1* (1), 19–25.
- (46) Liu, K.; Sun, Y.; Zhou, R.; Zhu, H.; Wang, J.; Liu, L.; Fan, S.; Jiang, K. Carbon Nanotube Yarns with High Tensile Strength Made by a Twisting and Shrinking Method. *Nanotechnology* **2010**, *21* (4), 045708.
- (47) Behabtu, N.; Young, C. C.; Tsentlovich, D. E.; Kleinerman, O.; Wang, X.; Ma, A. W. K.; Bengio, E. A.; Waarbeek, R. F. ter; Jong, J. J. de; Hoogerwerf, R. E.; Fairchild, S. B.; Ferguson, J. B.; Maruyama, B.; Kono, J.; Talmon, Y.; Cohen, Y.; Otto, M. J.; Pasquali, M. Strong, Light, Multifunctional Fibers of Carbon Nanotubes with Ultrahigh Conductivity. *Science* **2013**, *339* (6116), 182–186.

- (48) Badaire, S.; Pichot, V.; Zakri, C.; Poulin, P.; Launois, P.; Vavro, J.; Guthy, C.; Chen, M.; Fischer, J. E. Correlation of Properties with Preferred Orientation in Coagulated and Stretch-Aligned Single-Wall Carbon Nanotubes. *J. Appl. Phys.* **2004**, *96* (12), 7509–7513.
- (49) Kim, Y.; Minami, N.; Kazaoui, S. Highly Polarized Absorption and Photoluminescence of Stretch-Aligned Single-Wall Carbon Nanotubes Dispersed in Gelatin Films. *Appl. Phys. Lett.* **2005**, *86* (7), 073103.
- (50) Downes, R.; Wang, S.; Haldane, D.; Moench, A.; Liang, R. Strain-Induced Alignment Mechanisms of Carbon Nanotube Networks. *Adv. Eng. Mater.* **2014**, *17* (3), 349–358.
- (51) Callister, W. D.; Rethwisch, D. G.; others. *Materials Science and Engineering: An Introduction*; Wiley New York, 2007; Vol. 7.
- (52) Rubinstein, M.; Colby, R. H. *Polymer Physics*; OUP Oxford, 2003.
- (53) Xiao, H.-M.; Zhang, W.-D.; Lv, C.; Fu, S.-Y.; Wan, M.-X.; Mai, Y.-W. Large Enhancement in Conductivity of Polyaniline Films by Cold Stretching. *Macromol. Chem. Phys.* **2010**, *211* (10), 1109–1116.
- (54) Askeland, D. R.; Phulé, P. P. *The Science and Engineering of Materials*. **2003**.
- (55) Yu, Z.; Brus, L. Rayleigh and Raman Scattering from Individual Carbon Nanotube Bundles. *J. Phys. Chem. B* **2001**, *105* (6), 1123–1134.
- (56) Liu, T.; Kumar, S. Quantitative Characterization of SWNT Orientation by Polarized Raman Spectroscopy. *Chem. Phys. Lett.* **2003**, *378* (3-4), 257–262.
- (57) Lu, W.; Chou, T.-W. Analysis of the Entanglements in Carbon Nanotube Fibers Using a Self-Folded Nanotube Model. *J. Mech. Phys. Solids* **2011**, *59* (3), 511–524.
- (58) Cheng, Q.; Liang, R.; Wang, B.; Zhang, C. Composite Materials and Method for Making High-Performance Carbon Nanotube Reinforced Polymer Composites. US8916651 B2, December 23, 2014.
- (59) Futaba, D. N.; Hata, K.; Yamada, T.; Hiraoka, T.; Hayamizu, Y.; Kakudate, Y.; Tanaike, O.; Hatori, H.; Yumura, M.; Iijima, S. Shape-Engineerable and Highly Densely Packed Single-Walled Carbon Nanotubes and Their Application as Super-Capacitor Electrodes. *Nat. Mater.* **2006**, *5* (12), 987–994.
- (60) Hermans, P. H. *Contribution to the Physics of Cellulose Fibres: A Study in Sorption, Density, Refractive Power and Orientation*; Elsevier Publishing Company, 1946.
- (61) Hermans, J. J.; Hermans, P. H.; Vermaas, D.; Weidinger, A. Quantitative Evaluation of Orientation in Cellulose Fibres from the X-Ray Fibre Diagram. *Recl. Trav. Chim. Pays-Bas* **1946**, *65* (6), 427–447.
- (62) Gommans, H. H.; Alldredge, J. W.; Tashiro, H.; Park, J.; Magnuson, J.; Rinzler, A. G. Fibers of Aligned Single-Walled Carbon Nanotubes: Polarized Raman Spectroscopy. *J. Appl. Phys.* **2000**, *88* (5), 2509–2514.
- (63) Montgomery, H. C. Method for Measuring Electrical Resistivity of Anisotropic Materials. *J. Appl. Phys.* **1971**, *42* (7), 2971–2975.
- (64) Debye, P.; Bueche, A. M. Scattering by an Inhomogeneous Solid. *J. Appl. Phys.* **1949**, *20* (6), 518–525.
- (65) Debye, P.; Jr, H. R. A.; Brumberger, H. Scattering by an Inhomogeneous Solid. II. The Correlation Function and Its Application. *J. Appl. Phys.* **1957**, *28* (6), 679–683.
- (66) Jiang, K.; Li, Q.; Fan, S. Nanotechnology: Spinning Continuous Carbon Nanotube Yarns. *Nature* **2002**, *419* (6909), 801–801.

- (67) Downes, R. D.; Hao, A.; Park, J. G.; Su, Y.-F.; Liang, R.; Jensen, B. D.; Siochi, E. J.; Wise, K. E. Geometrically Constrained Self-Assembly and Crystal Packing of Flattened and Aligned Carbon Nanotubes. *Carbon* **2015**, *93*, 953–966.
- (68) Trayner, S.; Hao, A.; Downes, R.; Park, J. G.; Su, Y.-F.; Liang, R. High-Resolution TEM Analysis of Flatten Carbon Nanotube Packing in Nanocomposites. *Synth. Met.* **2015**, *204*, 103–109.
- (69) Kaw, A. K. *Mechanics of Composite Materials*; CRC Press, 1997.
- (70) Zhang, Y.; Zheng, L.; Sun, G.; Zhan, Z.; Liao, K. Failure Mechanisms of Carbon Nanotube Fibers under Different Strain Rates. *Carbon* **2012**, *50* (8), 2887–2893.
- (71) Roesler, J.; Harders, H.; Baeker, M. *Mechanical Behaviour of Engineering Materials - Metals, Ceramics, Polymers, and Composites*; Springer, 2007.
- (72) Wang, S.; Young, C.; Downes, R.; Hao, A.; Haldane, D.; Liang, R. Microstructure and Mechanical Property Characterizations of Buckypaper and Carbon Fiber Hybrid Composites; SAMPE TECH 2014. Seattle, WA, 2014.
- (73) Wang, S.; Downes, R.; Young, C.; Haldane, D.; Hao, A.; Liang, R.; Wang, B.; Zhang, C.; Maskell, R. Carbon Fiber/Carbon Nanotube Buckypaper Interply Hybrid Composites: Manufacturing Process and Tensile Properties. *Adv. Eng. Mater.* **2015**, n/a – n/a.
- (74) Wong, M.; Paramsothy, M.; Xu, X. J.; Ren, Y.; Li, S.; Liao, K. Physical Interactions at Carbon Nanotube-Polymer Interface. *Polymer* **2003**, *44* (25), 7757–7764.
- (75) Wardle, B. L.; Saito, D. S.; Garcia, E. J.; Hart, A. J.; de Villoria, R. G.; Verploegen, E. A. Fabrication and Characterization of Ultrahigh-Volume-Fraction Aligned Carbon Nanotube-Polymer Composites. *Adv Mater* **2008**, *20* (14), 2707–2714.
- (76) Motta, M.; Moisala, A.; Kinloch, I. A.; Windle, A. H. High Performance Fibres from “Dog Bone” Carbon Nanotubes. *Adv. Mater.* **2007**, *19* (21), 3721–3726.
- (77) Elliott, J. A.; Sandler, J. K. W.; Windle, A. H.; Young, R. J.; Shaffer, M. S. P. Collapse of Single-Wall Carbon Nanotubes Is Diameter Dependent. *Phys. Rev. Lett.* **2004**, *92* (9), 095501.
- (78) Zhong, X.-H.; Li, Y.-L.; Liu, Y.-K.; Qiao, X.-H.; Feng, Y.; Liang, J.; Jin, J.; Zhu, L.; Hou, F.; Li, J.-Y. Continuous Multilayered Carbon Nanotube Yarns. *Adv. Mater.* **2010**, *22* (6), 692–696.
- (79) Zhang, C.; Chen, L.; Chen, S. Adhesion between Two Radially Collapsed Single-Walled Carbon Nanotubes. *Acta Mech.* **2013**, *224* (11), 2759–2770.
- (80) Cheng, Q.; Li, M.; Jiang, L.; Tang, Z. Bioinspired Layered Composites Based on Flattened Double-Walled Carbon Nanotubes. *Adv. Mater.* **2012**, *24* (14), 1838–1843.
- (81) Plimpton, S. Fast Parallel Algorithms for Short-Range Molecular Dynamics. *J. Comput. Phys.* **1995**, *117* (1), 1–19.
- (82) Stukowski, A. Visualization and Analysis of Atomistic Simulation Data with OVITO—the Open Visualization Tool. *Model. Simul. Mater. Sci. Eng.* **2010**, *18* (1), 015012.
- (83) Pascal, T. A.; Karasawa, N.; Iii, W. A. G. Quantum Mechanics Based Force Field for Carbon (QMFF-Cx) Validated to Reproduce the Mechanical and Thermodynamics Properties of Graphite. *J. Chem. Phys.* **2010**, *133* (13), 134114.
- (84) Tang, J.; Qin, L.-C.; Sasaki, T.; Yudasaka, M.; Matsushita, A.; Iijima, S. Compressibility and Polygonization of Single-Walled Carbon Nanotubes under Hydrostatic Pressure. *Phys. Rev. Lett.* **2000**, *85* (9), 1887–1889.
- (85) López, M. J.; Rubio, A.; Alonso, J. A.; Qin, L.-C.; Iijima, S. Novel Polygonized Single-Wall Carbon Nanotube Bundles. *Phys. Rev. Lett.* **2001**, *86* (14), 3056–3059.

- (86) Xiao, J.; Liu, B.; Huang, Y.; Zuo, J.; Hwang, K.-C.; Yu, M.-F. Collapse and Stability of Single- and Multi-Wall Carbon Nanotubes. *Nanotechnology* **2007**, *18* (39), 395703.
- (87) Chopra, N. G.; Benedict, L. X.; Crespi, V. H.; Cohen, M. L.; Louie, S. G.; Zettl, A. Fully Collapsed Carbon Nanotubes. *Nature* **1995**, *377* (6545), 135–138.
- (88) Lourie, O.; Cox, D. M.; Wagner, H. D. Buckling and Collapse of Embedded Carbon Nanotubes. *Phys. Rev. Lett.* **1998**, *81* (8), 1638–1641.
- (89) Pantano, A.; M. Parks, D.; Boyce, M. C. Mechanics of Deformation of Single- and Multi-Wall Carbon Nanotubes. *J. Mech. Phys. Solids* **2004**, *52* (4), 789–821.
- (90) Zhang, X.; Li, Q. Enhancement of Friction between Carbon Nanotubes: An Efficient Strategy to Strengthen Fibers. *ACS Nano* **2010**, *4* (1), 312–316.
- (91) Zhao, R.; Luo, C. Torsion-Induced Mechanical Couplings of Single-Walled Carbon Nanotubes. *Appl. Phys. Lett.* **2011**, *99* (23), 231904.
- (92) Ni, B.; Sinnott, S. B. Chemical Functionalization of Carbon Nanotubes through Energetic Radical Collisions. *Phys. Rev. B* **2000**, *61* (24), R16343–R16346.
- (93) Jang, I.; Sinnott, S. B.; Danailov, D.; Keblinski, P. Molecular Dynamics Simulation Study of Carbon Nanotube Welding under Electron Beam Irradiation. *Nano Lett.* **2004**, *4* (1), 109–114.
- (94) Banhart, F. Irradiation Effects in Carbon Nanostructures. *Rep. Prog. Phys.* **1999**, *62* (8), 1181–1221.
- (95) Krasheninnikov, A. V.; Nordlund, K.; Sirviö, M.; Salonen, E.; Keinonen, J. Formation of Ion-Irradiation-Induced Atomic-Scale Defects on Walls of Carbon Nanotubes. *Phys. Rev. B* **2001**, *63* (24), 245405.
- (96) Krasheninnikov, A. V.; Nordlund, K.; Keinonen, J. Production of Defects in Supported Carbon Nanotubes under Ion Irradiation. *Phys. Rev. B* **2002**, *65* (16), 165423.
- (97) Krasheninnikov, A. V.; Nordlund, K.; Keinonen, J.; Banhart, F. Ion-Irradiation-Induced Welding of Carbon Nanotubes. *Phys. Rev. B* **2002**, *66* (24), 245403.
- (98) Krasheninnikov, A. V.; Banhart, F. Engineering of Nanostructured Carbon Materials with Electron or Ion Beams. *Nat. Mater.* **2007**, *6* (10), 723–733.
- (99) Krasheninnikov, A. V.; Nordlund, K. Ion and Electron Irradiation-Induced Effects in Nanostructured Materials. *J. Appl. Phys.* **2010**, *107* (7), 071301.
- (100) Skákalová, V.; Kaiser, A. B.; Osváth, Z.; Vértesy, G.; Biró, L. P.; Roth, S. Ion Irradiation Effects on Conduction in Single-Wall Carbon Nanotube Networks. *Appl. Phys. A* **2008**, *90* (4), 597–602.
- (101) Cress, C. D.; Schauerman, C. M.; Landi, B. J.; Messenger, S. R.; Raffaele, R. P.; Walters, R. J. Radiation Effects in Single-Walled Carbon Nanotube Papers. *J. Appl. Phys.* **2010**, *107* (1), 014316.
- (102) Zhang, M.; Fang, S.; Zakhidov, A. A.; Lee, S. B.; Aliev, A. E.; Williams, C. D.; Atkinson, K. R.; Baughman, R. H. Strong, Transparent, Multifunctional, Carbon Nanotube Sheets. *Science* **2005**, *309* (5738), 1215–1219.
- (103) Wang, S.; Liang, Z.; Wang, B.; Zhang, C. High-Strength and Multifunctional Macroscopic Fabric of Single-Walled Carbon Nanotubes. *Adv. Mater.* **2007**, *19* (9), 1257–1261.
- (104) Terrones, M.; Terrones, H.; Banhart, F.; Charlier, J.-C.; Ajayan, P. M. Coalescence of Single-Walled Carbon Nanotubes. *Science* **2000**, *288* (5469), 1226–1229.
- (105) Suenaga, K.; Colliex, C.; Iijima, S. In Situ Electron Energy-Loss Spectroscopy on Carbon Nanotubes during Deformation. *Appl. Phys. Lett.* **2001**, *78* (1), 70–72.

- (106) Wang, S.; Downes, R.; Young, C.; Haldane, D.; Liang, R.; Wang, B.; Zhang, C.; Maskell, R. Carbon Fiber/Carbon Nanotube Buckypaper Interply Hybrid Composites: Manufacturing Process and Tensile Properties. *Compos. Part Appl. Sci. Manuf.* Under review.
- (107) Wang, S.; Haldane, D.; Liang, R.; Smithyman, J.; Zhang, C.; Wang, B. Nanoscale Infiltration Behaviour and through-Thickness Permeability of Carbon Nanotube Buckypapers. *Nanotechnology* **2013**, *24* (1), 015704.
- (108) Thostenson, E. T.; Chou, T.-W. Aligned Multi-Walled Carbon Nanotube-Reinforced Composites: Processing and Mechanical Characterization. *J. Phys. Appl. Phys.* **2002**, *35* (16), L77–L80.
- (109) Thostenson, E. T.; Ren, Z.; Chou, T.-W. Advances in the Science and Technology of Carbon Nanotubes and Their Composites: A Review. *Compos. Sci. Technol.* **2001**, *61* (13), 1899–1912.
- (110) Baur, J.; Silverman, E. Challenges and Opportunities in Multifunctional Nanocomposite Structures for Aerospace Applications. *MRS Bull.* **2007**, *32* (04), 328–334.
- (111) Wardle, B. L.; Saito, D. S.; García, E. J.; Hart, A. J.; de Villoria, R. G.; Verploegen, E. A. Fabrication and Characterization of Ultrahigh-Volume-Fraction Aligned Carbon Nanotube–Polymer Composites. *Adv. Mater.* **2008**, *20* (14), 2707–2714.
- (112) Coleman, J. N.; Khan, U.; Blau, W. J.; Gun'ko, Y. K. Small but Strong: A Review of the Mechanical Properties of Carbon Nanotube–polymer Composites. *Carbon* **2006**, *44* (9), 1624–1652.
- (113) Vlasveld, D. P. N.; Bersee, H. E. N.; Picken, S. J. Nanocomposite Matrix for Increased Fibre Composite Strength. *Polymer* **2005**, *46* (23), 10269–10278.
- (114) Zhao, Z.-G.; Ci, L.-J.; Cheng, H.-M.; Bai, J.-B. The Growth of Multi-Walled Carbon Nanotubes with Different Morphologies on Carbon Fibers. *Carbon* **2005**, *43* (3), 663–665.
- (115) Wang, Z.; Liang, Z.; Wang, B.; Zhang, C.; Kramer, L. Processing and Property Investigation of Single-Walled Carbon Nanotube (SWNT) Buckypaper/epoxy Resin Matrix Nanocomposites. *Compos. Part Appl. Sci. Manuf.* **2004**, *35* (10), 1225–1232.
- (116) Cheng, Q. F.; Wang, J. P.; Wen, J. J.; Liu, C. H.; Jiang, K. L.; Li, Q. Q.; Fan, S. S. Carbon Nanotube/epoxy Composites Fabricated by Resin Transfer Molding. *Carbon* **2010**, *48* (1), 260–266.
- (117) Li, S.; Park, J. G.; Liang, R.; Zhang, C.; Wang, B. Effects of Solvent Immersion and Evaporation on the Electrical Conductance of Pre-Stressed Carbon Nanotube Buckypapers. *Nanotechnology* **2011**, *22* (36), 365706.
- (118) Chen, I.-W. P.; Liang, Z.; Wang, B.; Zhang, C. Charge-Induced Asymmetrical Displacement of an Aligned Carbon Nanotube Buckypaper Actuator. *Carbon* **2010**, *48* (4), 1064–1069.
- (119) Verrey, J.; Michaud, V.; Månson, J.-A. E. Dynamic Capillary Effects in Liquid Composite Moulding with Non-Crimp Fabrics. *Compos. Part Appl. Sci. Manuf.* **2006**, *37* (1), 92–102.
- (120) Amico, S. C.; Lekakou, C. Axial Impregnation of a Fiber Bundle. Part 1: Capillary Experiments. *Polym. Compos.* **2002**, *23* (2), 249–263.
- (121) Antonucci, V.; Giordano, M.; Nicolais, L.; Calabrò, A.; Cusano, A.; Cutolo, A.; Inserra, S. Resin Flow Monitoring in Resin Film Infusion Process. *J. Mater. Process. Technol.* **2003**, *143–144*, 687–692.
- (122) Kuentzer, N.; Simacek, P.; Advani, S. G.; Walsh, S. Permeability Characterization of Dual Scale Fibrous Porous Media. *Compos. Part Appl. Sci. Manuf.* **2006**, *37* (11), 2057–2068.

- (123) Muruganathan, R.; Müller, H.-J.; Möhwald, H.; Krastev, R. Effect of Headgroup Size on Permeability of Newton Black Films. *Langmuir* **2005**, *21* (26), 12222–12228.
- (124) Smithyman, J.; Moench, A.; Liang, R.; Zheng, J. P.; Wang, B.; Zhang, C. Binder-Free Composite Electrodes Using Carbon Nanotube Networks as a Host Matrix for Activated Carbon Microparticles. *Appl. Phys. A* **2012**, *107* (3), 723–731.
- (125) Xu, P.; Yu, B. Developing a New Form of Permeability and Kozeny–Carman Constant for Homogeneous Porous Media by Means of Fractal Geometry. *Adv. Water Resour.* **2008**, *31* (1), 74–81.
- (126) Heijs, A. W. J.; Lowe, C. P. Numerical Evaluation of the Permeability and the Kozeny Constant for Two Types of Porous Media. *Phys. Rev. E* **1995**, *51* (5), 4346–4352.
- (127) Åström, B. T.; Pipes, R. B.; Advani, S. G. On Flow through Aligned Fiber Beds and Its Application to Composites Processing. *J. Compos. Mater.* **1992**, *26* (9), 1351–1373.
- (128) Foley, G. A Review of Factors Affecting Filter Cake Properties in Dead-End Microfiltration of Microbial Suspensions. *J. Membr. Sci.* **2006**, *274* (1–2), 38–46.
- (129) Li, M.; Gu, Y.; Zhang, Z.; Sun, Z. A Simple Method for the Measurement of Compaction and Corresponding Transverse Permeability of Composite Prepregs. *Polym. Compos.* **2007**, *28* (1), 61–70.
- (130) Amico, S. C.; Lekakou, C. Axial Impregnation of a Fiber Bundle. Part 2: Theoretical Analysis. *Polym. Compos.* **2002**, *23* (2), 264–273.
- (131) Li, M.; Wang, S.; Gu, Y.; Zhang, Z.; Li, Y.; Potter, K. Dynamic Capillary Impact on Longitudinal Micro-Flow in Vacuum Assisted Impregnation and the Unsaturated Permeability of Inner Fiber Tows. *Compos. Sci. Technol.* **2010**, *70* (11), 1628–1636.
- (132) Gui, X.; Wei, J.; Wang, K.; Cao, A.; Zhu, H.; Jia, Y.; Shu, Q.; Wu, D. Carbon Nanotube Sponges. *Adv. Mater.* **2010**, *22* (5), 617–621.
- (133) Li, H.; Gui, X.; Zhang, L.; Wang, S.; Ji, C.; Wei, J.; Wang, K.; Zhu, H.; Wu, D.; Cao, A. Carbon Nanotube Sponge Filters for Trapping Nanoparticles and Dye Molecules from Water. *Chem. Commun.* **2010**, *46* (42), 7966.
- (134) Godara, A.; Mezzo, L.; Luizi, F.; Warriar, A.; Lomov, S. V.; Van Vuure, A. W.; Gorbatiikh, L.; Moldenaers, P.; Verpoest, I. Influence of Carbon Nanotube Reinforcement on the Processing and the Mechanical Behaviour of Carbon Fiber/epoxy Composites. *Carbon* **2009**, *47* (12), 2914–2923.
- (135) Kharisov, B. I.; Kharissova, O. V.; Dias, H. V. R. *Nanomaterials for Environmental Protection*; John Wiley & Sons, 2014.
- (136) Xie, B.; Liu, Y.; Ding, Y.; Zheng, Q.; Xu, Z. Mechanics of Carbon Nanotube Networks: Microstructural Evolution and Optimal Design. *Soft Matter* **2011**, *7* (21), 10039.
- (137) Xu, M.; Futaba, D. N.; Yamada, T.; Yumura, M.; Hata, K. Carbon Nanotubes with Temperature-Invariant Viscoelasticity from  $-196^{\circ}$  to  $1000^{\circ}\text{C}$ . *Science* **2010**, *330* (6009), 1364–1368.
- (138) Wang, C.; Xie, B.; Liu, Y.; Xu, Z. Mechanotunable Microstructures of Carbon Nanotube Networks. *ACS Macro Lett.* **2012**, *1* (10), 1176–1179.
- (139) Li, Y.; Kröger, M. A Theoretical Evaluation of the Effects of Carbon Nanotube Entanglement and Bundling on the Structural and Mechanical Properties of Buckypaper. *Carbon* **2012**, *50* (5), 1793–1806.
- (140) Li, Y.; Kröger, M. Viscoelasticity of Carbon Nanotube Buckypaper: Zipping–unzipping Mechanism and Entanglement Effects. *Soft Matter* **2012**, *8* (30), 7822.

- (141) Buehler, M. J. Mesoscale Modeling of Mechanics of Carbon Nanotubes: Self-Assembly, Self-Folding, and Fracture. *J. Mater. Res.* **2006**, *21* (11), 2855–2869.
- (142) Cranford, S. W.; Buehler, M. J. *In Silico* Assembly and Nanomechanical Characterization of Carbon Nanotube Buckypaper. *Nanotechnology* **2010**, *21* (26), 265706.
- (143) Zhigilei, L. V.; Wei, C.; Srivastava, D. Mesoscopic Model for Dynamic Simulations of Carbon Nanotubes. *Phys. Rev. B* **2005**, *71* (16), 165417.
- (144) Smajda, R.; Kukovecz, Á.; Kónya, Z.; Kiricsi, I. Structure and Gas Permeability of Multi-Wall Carbon Nanotube Buckypapers. *Carbon* **2007**, *45* (6), 1176–1184.
- (145) Whitby, R. L. D.; Fukuda, T.; Maekawa, T.; James, S. L.; Mikhailovsky, S. V. Geometric Control and Tuneable Pore Size Distribution of Buckypaper and Buckydiscs. *Carbon* **2008**, *46* (6), 949–956.
- (146) Scarpa, F.; Adhikari, S.; Wang, C. Y. Mechanical Properties of Non-Reconstructed Defective Single-Wall Carbon Nanotubes. *J. Phys. Appl. Phys.* **2009**, *42* (14), 142002.

1.

**1. Report Type**

Final Report

**Primary Contact E-mail**

Contact email if there is a problem with the report.

zliang@fsu.edu

**Primary Contact Phone Number**

Contact phone number if there is a problem with the report

850-645-8998

**Organization / Institution name**

Florida State University

**Grant/Contract Title**

The full title of the funded effort.

Macroscopic Crosslinked Neat Carbon Nanotube Materials and CNT/Carbon Fiber Hybrid Composites: Supermolecular Structure and New Failure Mode Study

**Grant/Contract Number**

AFOSR assigned control number. It must begin with "FA9550" or "F49620" or "FA2386".

FA9550-11-1-0131

**Principal Investigator Name**

The full name of the principal investigator on the grant or contract.

Richard Liang

**Program Manager**

The AFOSR Program Manager currently assigned to the award

Joycelyn Harrison

**Reporting Period Start Date**

07/01/2011

**Reporting Period End Date**

06/30/2015

**Abstract**

Two novel low-density material systems were explored to attempt to realize the ultimate intrinsic properties of CNTs for scale-up applications: 1) continuous highly aligned CNT tapes or sheets and 2) CNT sheet/carbon fiber hybrid composites (CNT/CF) with aerospace-grade quality and carbon fiber concentration. Different approaches for engineering CNT networks in CNT thin films to achieve a high degree of alignment and graphitic crystal packing were studied. We discovered that the unique geometrically constrained self-assembly and graphitic crystal packing of flattened and aligned CNTs can lead to close surface contact between CNTs to substantially improve the load transfer and mechanical properties. We also revealed that extremely low permeability ( $\times 10^{-17} \sim -19$  m<sup>2</sup>) of CNT thin film or buckypaper materials could largely eliminate through-thickness flow of resin matrix during composite autoclave fabrication process. Modifications in the processing parameters and consideration of strong capillary resin absorption of CNT networks during CNT buckypaper/CF prepreg materials for hybrid composites are needed to fabricate aerospace-grade hybrid composites with 5–8 wt.% CNT and 50–60 vol.% carbon fiber concentrations. The composites with CNT/CF alternative interply hybridization demonstrated promising mechanical/electrical multifunctional feature. Strong CNT layers acted as effective microcrack arresting layers to potentially improve damage tolerance properties.

**Distribution Statement**

This is block 12 on the SF298 form.

Distribution A - Approved for Public Release

**Explanation for Distribution Statement**

If this is not approved for public release, please provide a short explanation. E.g., contains proprietary information.

**SF298 Form**

Please attach your SF298 form. A blank SF298 can be found [here](#). Please do not password protect or secure the PDF. The maximum file size for an SF298 is 50MB.

[SF 298 for FA9550-11-1-0131.pdf](#)

**Upload the Report Document. File must be a PDF. Please do not password protect or secure the PDF . The maximum file size for the Report Document is 50MB.**

[Aligned CNT Composites FSU-GT report final report 092815.pdf](#)

**Upload a Report Document, if any. The maximum file size for the Report Document is 50MB.**

**Archival Publications (published) during reporting period:**

**Changes in research objectives (if any):**

**Change in AFOSR Program Manager, if any:**

**Extensions granted or milestones slipped, if any:**

**AFOSR LRIR Number**

**LRIR Title**

**Reporting Period**

**Laboratory Task Manager**

**Program Officer**

**Research Objectives**

**Technical Summary**

**Funding Summary by Cost Category (by FY, \$K)**

	Starting FY	FY+1	FY+2
Salary			
Equipment/Facilities			
Supplies			
Total			

**Report Document**

**Report Document - Text Analysis**

**Report Document - Text Analysis**

**Appendix Documents**

**2. Thank You**

**E-mail user**

Sep 28, 2015 15:26:54 Success: Email Sent to: zliang@fsu.edu